8-2018

Effect of Chemistry on Electrodynamics in the Martian Dynamo Region

Morgan M. Matheny

EFFECT OF CHEMISTRY ON ELECTRODYNAMICS IN THE MARTIAN DYNAMO REGION

BY
MORGAN M. MATHENY

A Thesis
Submitted to the Department of Physical Sciences
and the Committee on Graduate Studies
In partial fulfillment of the requirements
for the degree of
Master in Science in Engineering Physics

08/2018
Embry-Riddle Aeronautical University
Daytona Beach, Florida

EFFECT OF CHEMISTRY ON ELECTRODYNAMICS IN THE MARTIAN DYNAMO REGION

by

Morgan M. Matheny

This thesis was prepared under the direction of the candidate's Thesis Committee Chair, Dr. H. Katariina Nykyri, Professor, Daytona Beach Campus, and Thesis Committee Members Dr. Xuanye Ma, Assistant Research Professor, Daytona Beach Campus, and Dr. Jérémy A. Riousset, Assistant Professor, Florida Institute of Technology, and has been approved by the Thesis Committee. It was submitted to the Department of Physical Sciences in partial fulfillment of the requirements of the degree of

Master of Science in Engineering Physics

THESIS COMMITTEE:

Dr. H. Katariina Nykyri,
Committee Chair

Xuanye Ma.

Dr. Xuanye Ma,
Committee Member

Dr. Jérémy A. Riousset,
Committee Member

Dr. Matthew Zettergren,
Graduate Program Chair,
Engineering Physics

Dr. Terry Oswalt,
Department Chair,
Physical Sciences

Dr. Karen Gaines,
Dean, College of Arts and Sciences

Lon D. Moeller,
Senior V.P. for Academic Affairs and Provost

Abstract

Electromagnetic interactions between Mars remnant crustal magnetic fields and solar and planetary ions lead to time and space variations of the ionosphere. In this work, we continue the investigations started by *Riousset et al.* [2013] and address the effect of chemistry on ion populations in the dynamo region, where ion dynamics are driven by collisions while electrons are still mostly magnetized. We adopt a mesoscale model to simulate dynamics of electrons and ions in the upper atmosphere (100–400 km). Our approach focuses on numerical studies using the Martian Multifluid Magnetohydrodynamic (MF-MHD) Model (M^4). The dynamo is a region which varies in time and space due to the lack of a global planetary intrinsic magnetic field, the location of the remnant crustal fields, and the planetary rotation responsible for day/night transition and subsequent trans-terminator particle transfer. The time scales of atmospheric collisions, gyromotions, and chemical processes are discussed in detail to support the selection of relevant reactions for mesoscale studies of the dynamo regions. Several schemes are available in the referenced literature [e.g., *Najib et al.*, 2011; *Brain et al.*, 2015; *Dong et al.*, 2018], and the chemistry model developed as part of this work is based on *Najib et al.* [2011]. The improved model more accurately reflects changes in the population of planetary ions, which can alter the dynamo current, thereby also causing perturbations of the magnetic field. The MAVEN mission has shown the importance of ion escape in the Martian atmospheric loss, and previous modeling studies [e.g., *Riousset et al.*, 2014] have shown that electrodynamics in the dynamo region may impact upward transport of ions from this region, supporting the need for further studies. This work shows that the inclusion of chemistry results in substantial changes of ion distributions. Furthermore, differences in the symmetry, strength and

altitude range of the dynamo current are observed, likely stemming from the absence of a peak electron density region because of an unbalanced production/destruction of CO_2^+.

Acknowledgments

First and foremost, I would like to express my neverending gratitude to my science advisor Dr. Jérémy A. Riousset, who introduced me to the field of magnetohydrodynamics. Without his guidance, advice, and confidence during the last two years, the research presented in this work would not have been possible. I would also like to thank Dr. H. Katariina Nykyri and Dr. Xuanye Ma for their invaluable feedback and support as members of my thesis committee. I am also indebted to the AGU community for the many helpful discussions and lectures during the 2017 AGU Fall Meeting.

Finally, I would like to thank my family with a special thought for my parents Tina and Sam, my grandmother Mary, and my fiancé Iris, for the endless encouragements and support that they have given to me.

Morgan Matheny
Daytona Beach, FL
June 28, 2018

This research was supported by the Florida Space Grant Consortium under the Masters Fellowship Grant (NNX15009) to Embry-Riddle Aeronautical University.

Dedication

to my loving mother and father,

Tina Robinson and Sam Matheny

without whom I would not be the man I am today.

Contents

List of Tables

List of Figures

Chapter 1

Introduction

Mars is a major priority for current and future solar system exploration missions [MEPAG, 2015]. There is a desire to understand how the red planet lost its atmosphere to the solar wind during the earlier phases of the solar system and whether or not it once supported bacterial life. Recent observations [e.g., *Withers*, 2009] have shown that Mars represents a delicately coupled system where even minor changes can cause significant physical effects on even the most distant components. The dayside ionosphere is a prime example of this balance, where conditions depend on solar activity, remanent magnetism, collisions between magnetized and non-magnetized particles, and ion neutral chemistry.

1.1 Mars Magnetic Field

One of the most important discoveries of Mars Global Surveyor (MGS) was a distinct lack of global magnetic field on Mars [e.g., *Acuña*, 1999]. However, the planet is not entirely devoid of magnetism. The MGS mission revealed that similar to the Moon, Mars is dominated by a remanent field of lithospheric origins. This phenomena is also present on Earth, but is largely overshadowed by the larger global field (see Figure 1.2). *Connerney et al.* [1999] demonstrated that the strength of these crustal fields on Mars is not negligible. The remanent Martian magnetization exceeds terrestrial crust magnitudes tenfold (see Figure 1.2).

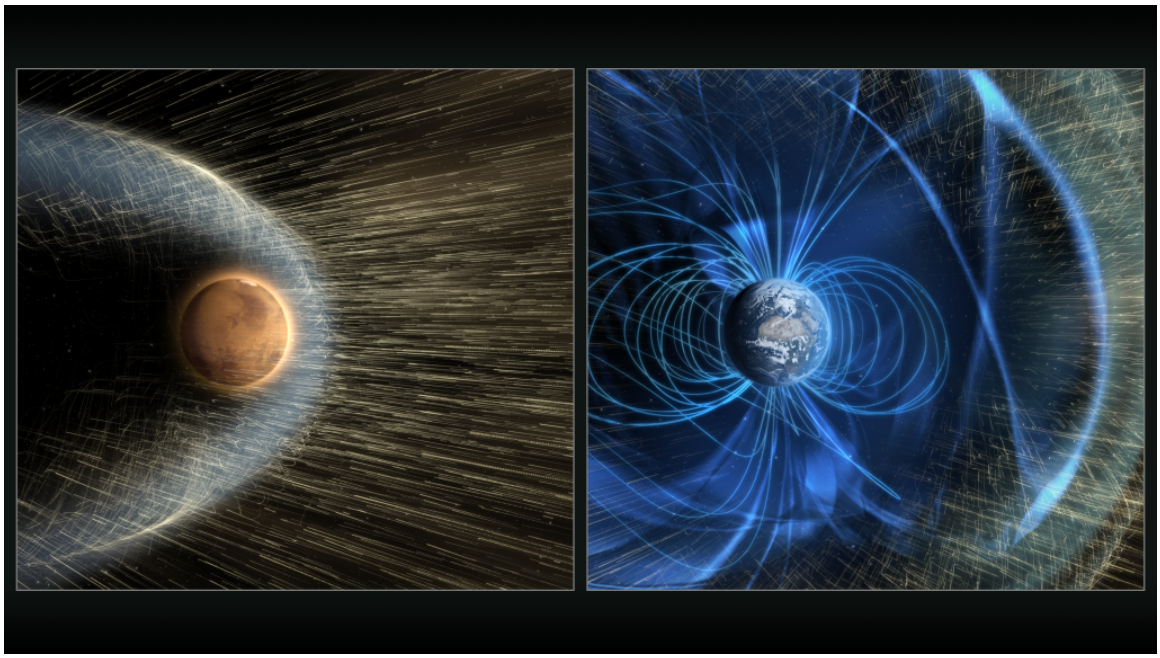

Figure 1.1: Artist depiction of the magnetic field of Mars (seen on left) compared to the magnetic field of Earth (seen on right) and their respective interactions with the solar wind [e.g., *Green*, 2017].

The field strength varies on scales of 50–100 km with strong day/night asymmetries. *Shinagawa* [2000] demonstrated that a multitude of small scale magnetic structures of crustal origin exists within the ionosphere of Mars in various regions. This leads to an environment where the remanent field is sufficient to drive magnetic processes in the ionosphere. In particular, *Fillingim et al.* [2010] show regions of enhanced ionization existing near local magnetic cusps. *Withers and Mendillo* [2005] hypothesize that anomalous results in some MGS electron profiles are linked to the geometry of the local magnetic field. Strong and weak fields exist in close proximity, leading to the formation of magnetic cusps and loops. *Mitchell et al.* [2001] showed that magnetic field strength varies by up to two orders of magnitude, sometimes reaching values of 200 nT at an altitude of 400 km. This magnetic field structure has a significant influence on the electrodynamics in the Martian ionosphere. *Halekas et al.* [2008] found electrons accelerating downwards near radial fields at cusps, as seen by MGS. *Bertaux et al.* [2005] observed an aurora in the martian atmosphere using

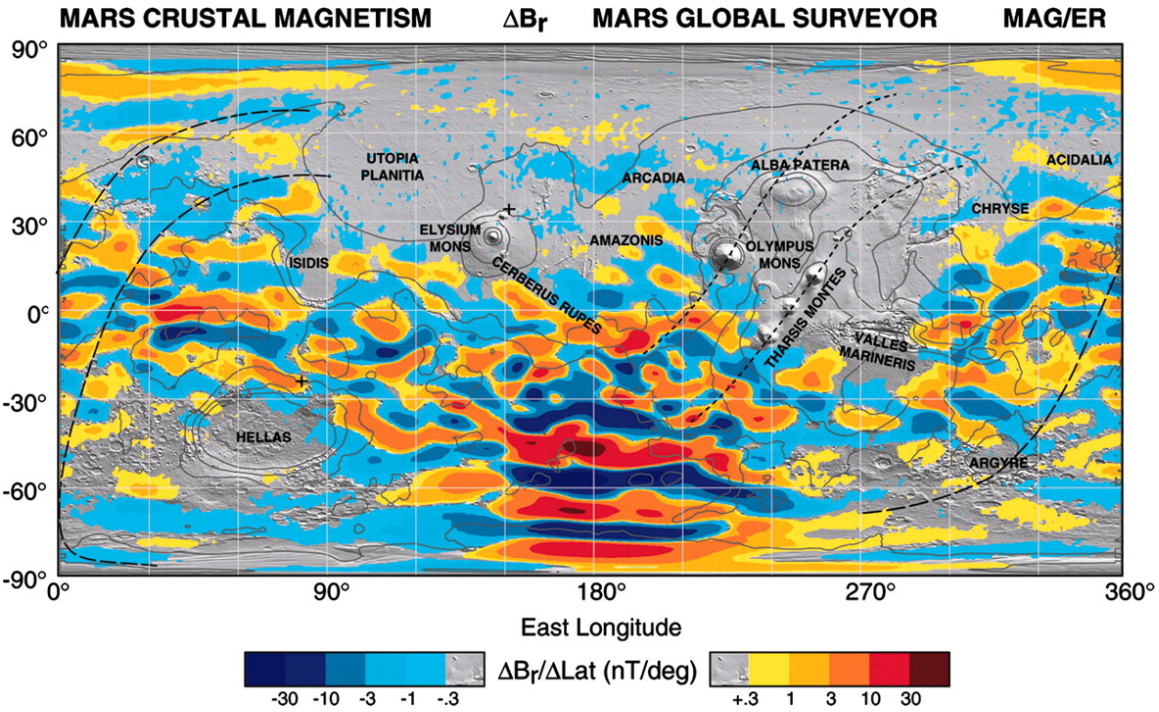

Figure 1.2: MGS observations of Martian radial magnetic field at 400 km altitude [*Connerney et al.*, 1999]. Red-green colored regions represent intense field strength in the upward direction, while dark blue regions represent intense field strength in the downward direction.

the ultraviolet spectrometer SPICAM on board Mars Express, and conclude that the aurora are a highly concentrated and localized emission controlled by magnetic field anomalies in the martian crust. The spectra of these electrons are similar in shape to observations done at the Earth's auroral zones. In such an environment one would expect an increase in ionization, therefore leading to an enhancement in ionospheric density.

Previous reviews of the Martian ionosphere relied mostly on upper atmospheric mass spectrometer measurements from the Viking 1 and Viking 2 landers [e.g., *Lewis et al.*, 1999]. *Zhang et al.* [1990] showed that Mars has much more variation between day and nightside as compared to a planet with a well defined magnetic field, and that Martian dust storms can "lift" the ionosphere by 20–30 km. According to *Barth et al.*

[1992], atomic oxygen escape is caused by a non-thermal process, namely the dissociative recombination of O_2^+. *Trotignon et al.* [2000] concluded that the transfer of momentum of the solar wind to the upper part of the ionosphere plays a considerable role in the loss of the atmosphere of Mars.

These missions predated Mars Express (MEX), which provided substantial datasets from the Mars Radio Science Experiment (MaRS) and the Sub-Surface Sounding Radar Altimeter (MARSIS). *Kopf et al.* [2008] observed transient ion layers in the martian ionosphere (see Figure 1.1). These layers may be related to the "dynamo current," a phenomena that *Riousset et al.* [2013] and others sought to understand and one that this work seeks to build upon. Mars Express datasets along with the electron density profiles provided by the Mars Global Surveyor (MGS) radio occultation experiment [*Hinson et al.*, 1999; *Withers*, 2009] allowed new studies of the different processes causing variability of the ionosphere.

Fillingim et al. [2010] examined the electrodynamics of the dynamo region of the ionosphere, an environment where electrons are guided by gyromotions around magnetic field lines while ion motions are driven by collisions. They estimated this region to lie approximately between 110 and 160 km altitude, and showed that non-uniform density profiles and the presence of neutral winds can lead to formation of electric current. *Fox* [2004] further established that ion-neutral collisions may be a driving factor in the lower ionosphere of Mars between 100 and 200 km. *Withers* [2008] predicted that currents of on the order of 10^{-8} A/m^2 are likely to form within the dynamo region in the presence of 50 nT background fields. In a subsequent study *Fillingim et al.* [2012] demonstrated that magnetic perturbations resulting from the conduction currents could be detected by the Mars Atmosphere and Volatile EvolutioN (MAVEN) mission, which inserted into its orbit on September 22, 2014.

MAVEN is the first spacecraft devoted to studying the Mars upper atmosphere and ionosphere, its interactions with the Sun and solar wind, and the subsequent escape of atmospheric gases to space [e.g., *Jakosky et al.*, 2015]. The study by *Bougher et al.* [2014] revealed that the early findings of the MAVEN *deep dip* campaign confirmed that ionospheric structure is closely tied not only to the crustal fields, but also to ion neutral chemical processes and the solar wind. *Romanelli et al.* [2018] showed that the

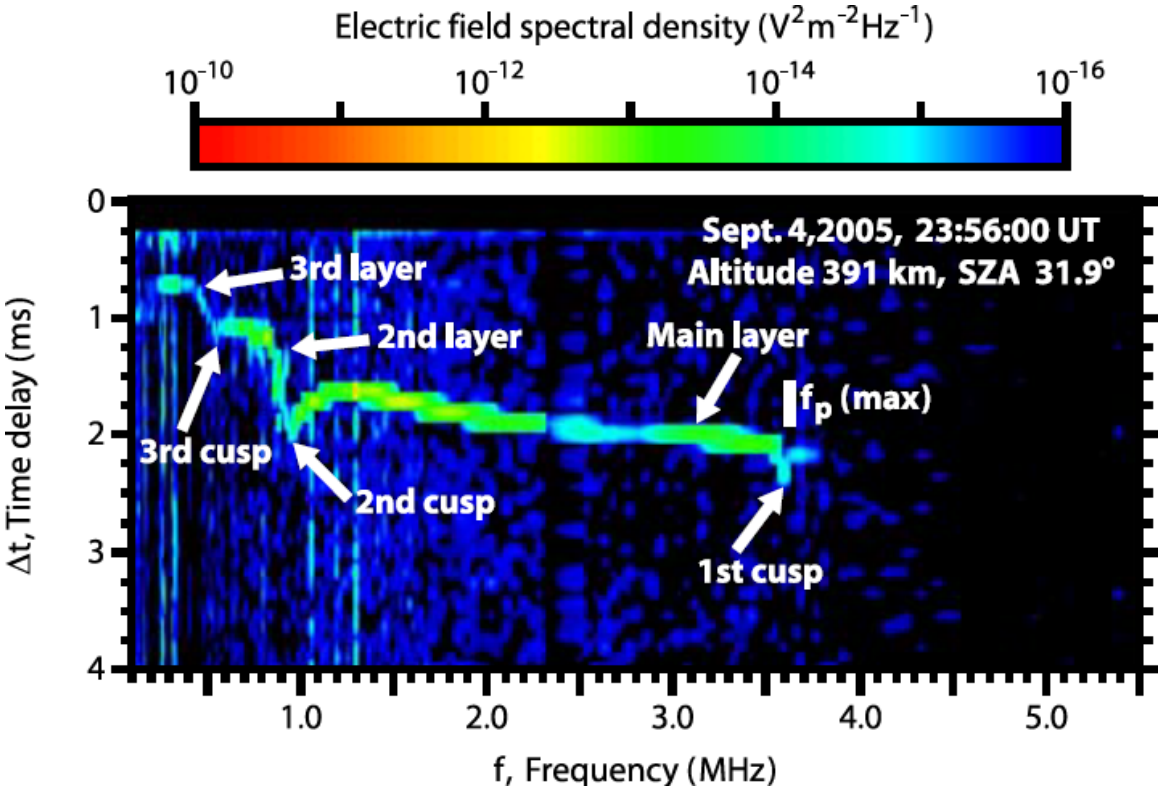

Figure 1.3: Characteristic signatures of transient ion layers on the dayside, 180–220 km altitude, timescale of tens of seconds to several minutes [Kopf et al., 2008].

interaction of the solar wind with the crustal magnetic fields constantly modify the intrinsic field properties, leading to a highly dynamic magnetic field topology. *Brain et al.* [2015] used MAVEN data to map outgoing and incoming planetary ion fluxes, and show that there exists net escape of planetary ions on the nightside. Interestingly, they show that planetary ions travel toward the planet in the southern hemisphere on the dayside. Numerical modeling by *Dong et al.* [2018] accurately reproduce these loss estimates. In addition, they conclude that the photochemical loss of atomic hot oxygen dominates over the total ion loss at the current epoch while the atmospheric ion loss is likely much more important at ancient times.

The dynamo is a region where electrons are magnetized and ions are not. We refer to a magnetized particle as an electron or as a singly ionized species of oxygen molecule O_2^+, oxygen atom CO_2^+, or carbon dioxide O^+ with a gyropath that is not

notably disturbed by collisions with other charged or neutral species. The upper and lower ranges of this region on Mars are usually between 100 and 400 km depending on the values of the local magnetic field and the electron, ion, and neutral densities. The altitude ranges can be estimated by comparing the gyrofrequencies of O_2^+ (the dominant ion) and electrons to their respective collision frequencies with CO_2 (the most abundant neutral).

The gyrofrequency Ω_α for a singly charged species α is given by its standard definition: $\Omega_\alpha = \frac{eB}{m_\alpha}$, where e and m_α are the elementary charge and the mass of the particle α, respectively. On the other hand, the electron-CO_2 and O_2^+-CO_2 collision frequencies ν depend on altitude and are given as a function of the temperatures of electrons, ions, and neutrals. Specifically, electrons are expected to be mostly demagnetized below the altitude defined by $\Omega_e = \nu_{e-CO_2}$, and magnetized above. Similarly, O_2^+ ions are expected to be magnetized above the altitude where their cyclotron frequency $\Omega_{O_2^+}$ is equal to their collision frequency with CO_2 and demagnetized below. Together, these two altitudes form the *a priori* upper and lower boundaries of the dynamo region as summarized in Table 1.1.

$z \geq 200$ km	$\nu_{O_2^+-CO_2} \ll \Omega_{CO_2}$ $\nu_{e-CO_2} \ll \Omega_e$	Magnetized ions. Magnetized electrons.	No dynamo current
125 km$\leq z \leq$200 km	$\nu_{O_2^+-CO_2} \geq \Omega_{CO_2}$ $\nu_{e-CO_2} \ll \Omega_e$	Demagnetized ions. Magnetized electrons.	Dynamo current
$z \leq 125$ km	$\nu_{O_2^+-CO_2} \geq \Omega_{CO_2}$ $\nu_{e-CO_2} \geq \Omega_e$	Demagnetized ions. Demagnetized electrons.	No differential current.

Table 1.1: Driving factors of charged particle dynamics in the Martian ionosphere.

The work in this paper revolves around the role of electrodynamics in the dynamo region and how they influence ion escape. *Riousset et al.* [2013] introduce the Martian Multifluid Magnetohydrodynamic Model (M^4), using uniform magnetic field geometries to validate the model and to demonstrate the formation of the dynamo currents between altitudes of 100 and 200 km. In addition, they show that the currents depend on the strength of the crustal fields as well as the neutral wind speeds. Uniform fields are an obvious over simplification of the crustal fields, which in reality are much more complex. *Langlais et al.* [2004] demonstrated that the crustal field

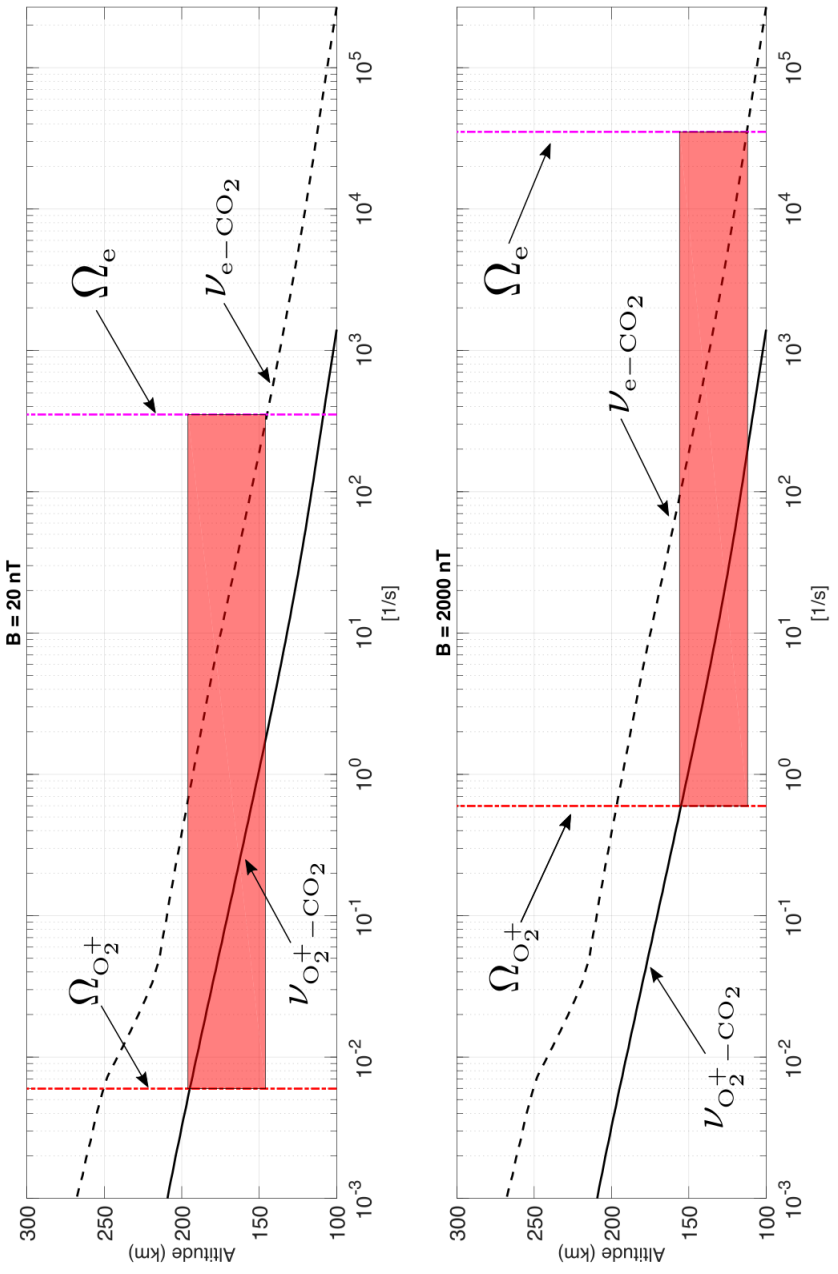

Figure 1.4: Estimated altitudes of the dynamo region for uniform, upward magnetic fields of magnitude 20 nT and 2000 nT. The upper boundary is estimated by comparing the gyrofrequency of the most abundant ion ($\Omega_{O_2^+}$) to the collision frequency of O_2^+ with CO_2, the most abundant neutral (denoted by $\nu_{O_2^+-CO_2}$). The lower boundary is estimated by comparing the gyrofrequency of electrons (Ω_e) to the collision frequency of electrons with CO_2 (denoted by ν_{e-CO_2}). Estimated dynamo region highlighted in red.

can be effectively modeled by buried dipoles below the surface, adequately reproducing the observations of MGS at 400 km altitudes. The model in this thesis uses a similar strategy of buried dipoles on a regional scale (first implemented by *Riousset et al.* [2014]) to investigate the dynamics of the dynamo region, and to conclude that strongly magnetized regions are likely to shield the local atmosphere and alter the motions of charged particles from the lower to the upper atmosphere.

The composition of the upper atmosphere and ionosphere of Mars is highly variable on the day and night side and an understanding of the role of chemistry in this region is needed to determine ion, electron, and neutral distributions. The study of volatile escape processes is the subject of active investigation as to how Mars lost most of its atmosphere throughout its history. The hybrid photochemical model of *Bößwetter et al.* [2010] analyzes ion loss rates of Mars many billions of years ago when solar activity was substantially higher and found that the level of ionization was sufficient to lead to substantial loss of atmosphere. *Krasnopolsky* [2002] perform investigations of Martian chemistry using a one dimensional chemical model to provide dissociative reaction rates used in this work. Together with others, these works help form the basis of the chemistry scheme developed in this paper.

The model described in this work (M^4) differs from several other MHD and MF-MHD models used at Mars in that it simulates collisions between electrons, ions, and neutrals. This makes the use of an approximate conductivity/resistivity redundant. Collisional interactions are able to generate currents, electric fields, and magnetic perturbations in the dynamo region but are not included in many existing models such as *Haider et al.*'s [1992] photochemical model, *Bougher et al.*'s [2009] global circulation model, *Ledvina et al.*'s [2008] semikinetic hybrid models, and *Ma et al.*'s [2004] single fluid, multispecies MHD model. *Najib et al.* [2011] introduced a collisional multifluid MHD model accounting for collisions between ion-neutrals and ion-ions as well as chemistry on a planetary scale. This approximation dampens out the conditions for forming the dynamo region's upper boundary and may result in upper boundary altitudes beyond 250 km [e.g., *Riousset et al.*, 2014].

1.2 Organization of the thesis

Chapter 1 began our discussion by reviewing reviewing previous studies of the Martian magnetic field and atmosphere followed by efforts to model the complex dynamics of its ionosphere. Chapter 2 begins by introducing the M^4 model and profiles used to determine initial conditions. The chemistry scheme to be used is then shown, followed by numerical methods used to simulate the model. Chapter 3 is where the analytical solutions for the chemical model are formulated and then tested to validate the scheme. Chapter 4 discusses the findings of this work will be performed by examining how the new chemistry scheme compares to previous work.

1.3 Scientific contributions

This work makes several contributions to the fields of magnetohydrodynamic modeling and specifically to the modeling of the Martian atmosphere, which can be summarized as follows:

1. A chemistry scheme is formulated to be used in a collisional multifluid magnetohydrodynamic model applied to the Martian ionosphere.

2. That scheme is then implemented into the conservation of mass, momentum, and energy density equations as well as the generalized Ohm's law of the M^4 model.

3. The chemical source and loss terms are tested and validated by deriving analytical solutions to the conservation equations, and comparing those with numerical solutions of simulations.

4. The effects of chemistry on ion population densities and the atmospheric dynamo current strength and altitude range are analyzed and discussed.

This work has been disseminated in the form of a poster presentation at the American Geophysical Union 2017 meeting in New Orleans, LA.

Chapter 2

Model Formulation

The purpose of this chapter is to formulate the model used in this thesis. The first section describes the M^4 model. The second section describes the profile, boundary conditions, and numerical methods used by this model. The third section introduces and describes how the chemistry scheme is implemented into the model. Finally, a discussion summarizes the findings of this chapter.

2.1 Mars Multifluid Magnetohydrodynamic Model (M^4)

This section describes the formulation of the model used in this work through the development of conservation laws along with Maxwell's equations.

MF-MHD equations

This work is based on the existing M^4 model. It has already been developed and applied effectively to study the interactions between neutral winds, the local Martian ionosphere, and crustal fields [*Riousset et al.*, 2013; 2014]. Our plasma dynamics model employ the classic conservation laws derived from the collisional Boltzmann equation: matter (2.1), momentum (2.2), and pressure/energy density (2.3), and calculates them separately for each ion species. The subscript i denotes the ions, e

the electrons, and n the neutrals. The variable $\vec{u}$ is the ion/electron/neutral fluid velocity, p denotes the pressure, e the elementary charge, m the mass, and n the number density. The vectors $\vec{E}$ and $\vec{B}$ represent the electric and magnetic fields, respectively, and $\vec{J}$ stands for the current density. The fluid equations for the original M^4 model are given by [e.g., *Riousset et al.*, 2013]:

$$\frac{\partial n_i}{\partial t} = -\nabla_{\vec{r}} \cdot (n_i \vec{u}_i) \tag{2.1}$$

$$\frac{\partial \vec{u}_i}{\partial t} = -(\vec{u}_i \cdot \nabla_{\vec{r}})\vec{u}_i + \frac{e}{m_i}\left(\vec{E} + \vec{u}_i \times \vec{B}\right) - \frac{\nabla_{\vec{r}} p_i}{m_i n_i} - \frac{\vec{g}_{\mathrm{M}}}{\left(1 + \frac{z}{R_{\mathrm{M}}}\right)^2} + \sum_{\beta} \nu_{i,\beta}\left(\vec{u}_\beta - \vec{u}_i\right) \tag{2.2}$$

$$\frac{\partial p_i}{\partial t} = -\gamma_i \nabla_{\vec{r}} \cdot (p_i \vec{u}_i) + (\gamma_i - 1)\, \vec{u}_i \cdot \nabla_{\vec{r}} p_i \tag{2.3}$$

The variable z is the altitude in km, t is elapsed time, and $\nabla_{\vec{r}}$ is the spatial gradient, present in all conservation equations. The constant $\vec{g}_{\mathrm{M}}$ is the acceleration due to gravity on Mars, R_{M} is the radius of Mars (3389 km), and γ the specific heat ratio of neutrals and ions. Elastic collisions between neutrals, ions, and electrons are represented by collision rates, denoted by $\nu_{\alpha,\beta}$, and given in Table 2.1. The model does not yet account for inelastic conditions or heat exchange. The addition of chemistry is done as part of this work and is addressed specifically in Section 2.2. Electrons are treated as a fluid, their dynamics driven by the plasma approximation (2.4), the conduction current definition (2.5), and the adiabatic equation of state (2.6):

$$n_{\mathrm{e}} = \sum_i n_i \tag{2.4}$$

$$\vec{u}_{\mathrm{e}} = \sum_i \frac{q_i n_i}{q_{\mathrm{e}} n_{\mathrm{e}}} \vec{u}_i - \frac{\vec{J}}{q_{\mathrm{e}} n_{\mathrm{e}}} \tag{2.5}$$

$$\frac{\partial p_{\mathrm{e}}}{\partial t} = -\gamma_{\mathrm{e}} \nabla_{\vec{r}} \cdot (p_{\mathrm{e}} \vec{u}_{\mathrm{e}}) + (\gamma_{\mathrm{e}} - 1)\, \vec{u}_{\mathrm{e}} \cdot \nabla_{\vec{r}} p_{\mathrm{e}} \tag{2.6}$$

Table 2.1: Collision rates [*Schunk and Nagy*, 2000, pp. 96–99]. Rates denoted by ν, units in s^{-1}.

α	$\nu_{\alpha\to CO_2}$	$\nu_{\alpha\to O}$	$\nu_{\alpha\to O_2^+}$	$\nu_{\alpha\to CO_2^+}$	$\nu_{\alpha\to O^+}$	$\nu_{\alpha\to e}$
O_2^+	$5.63\times10^{-10}n_{CO_2}$	$2.31\times10^{-10}n_O$	$0.16\frac{n_{O_2^+}}{T_{O_2^+}^{3/2}}$	$0.17\frac{n_{O_2^+}}{T_{CO_2^+}^{3/2}}$	$0.13\frac{n_{O^+}}{T_{O^+}^{3/2}}$	-
CO_2^+	$\begin{cases}2.85\times10^{-11}n_{CO_2}T_r^{0.5}(1-0.083\log(T_r))^2\\ T_r>850\text{ K}\end{cases}$	$1.76\times10^{-10}n_O$	$0.12\frac{n_{O_2^+}}{T_{O_2^+}^{3/2}}$	$0.14\frac{n_{CO_2^+}}{T_{CO_2^+}^{3/2}}$	$0.10\frac{n_{O^+}}{T_{O^+}^{3/2}}$	-
O^+	$8.95\times10^{-10}n_{CO_2}$	$\begin{cases}3.67\times10^{-11}n_OT_r^{0.5}(1-0.064\log(T_r))^2\\ T_r>235\text{ K}\end{cases}$	$0.26\frac{n_{O_2^+}}{T_{O_2^+}^{3/2}}$	$0.27\frac{n_{CO_2^+}}{T_{CO_2^+}^{3/2}}$	$0.22\frac{n_{O^+}}{T_{O^+}^{3/2}}$	-
e	$3.68\times10^{-8}n_{CO_2}(1+4.1\times10^{-11}\lvert4500-T_e\rvert^{2.93})$	$8.9\times10^{-11}n_O(1+5.7\times10^{-4}T_e)T_e^{0.5}$	$54.5\frac{n_{O_2^+}}{T_{O_2^+}^{3/2}}$	$54.5\frac{n_{CO_2^+}}{T_{CO_2^+}^{3/2}}$	$54.5\frac{n_{O^+}}{T_{O^+}^{3/2}}$	$\frac{54.5}{\sqrt{2}}\frac{n_e}{T_e^{3/2}}$

$T_r=\frac{T_i+T_n}{2}$

Prior to this work, no chemistry scheme had been implemented into M^4. The plasma current is obtained from Ampère's law (2.7), where the displacement current is neglected by the Darwin approximation (i.e., the gyrofrequency remains consistently smaller than the plasma frequency). On the other hand, the electric and magnetic fields are obtained from the generalized Ohm's law (2.9) and Faraday's law (2.8). The electrodynamic description is then:

$$\vec{J} = \frac{\nabla_{\vec{r}} \times \vec{B}}{\mu_0} \tag{2.7}$$

$$\frac{\partial \vec{B}}{\partial t} = -\nabla_{\vec{r}} \times \vec{E} \tag{2.8}$$

$$\vec{E} = -\sum_i \frac{q_i n_i}{q_\mathrm{e} n_\mathrm{e}} \vec{u}_i \times \vec{B} + \frac{\vec{J} \times \vec{B}}{q_\mathrm{e} n_\mathrm{e}} - \frac{\nabla_{\vec{r}} p_\mathrm{e}}{q_\mathrm{e} n_\mathrm{e}} + \frac{m_\mathrm{e}}{q_\mathrm{e}} \sum_n \nu_{n-\mathrm{e}} \left(\vec{u}_n - \vec{u}_\mathrm{e}\right) + \frac{m_\mathrm{e}}{q_\mathrm{e}} \sum_i \nu_{i-\mathrm{e}} \left(\vec{u}_i - \vec{u}_\mathrm{e}\right) \tag{2.9}$$

The $\vec{J} \times \vec{B}$ and $\nu_{\mathrm{i}-\beta}$ terms in Equation (2.9) define M^4 as being a Hall, resistive, multifluid model. *Riousset et al.* [2013] assume that collisions are elastic and therefore only change the momentum of ions (2.2) and Ohm's law (2.9), and do not affect the conservation of energy (2.3), (2.6), or the continuity equation (2.1):

$$\frac{\partial \vec{u}_i}{\partial t} + \vec{u}_i \cdot \nabla_{\vec{r}} \vec{u}_i = \frac{q_i}{m_i}\left(\vec{E} + \vec{u}_i \times \vec{B}\right) - \frac{\nabla_{\vec{r}} p_i}{m_i n_i} + \frac{\vec{g}_M}{(1 + \frac{z}{R_\mathrm{M}})^2} - \sum_\beta \underbrace{\nu_{i,\beta}}_{\text{collision frequency}} \left(\vec{u}_i - \vec{u}_\beta\right)$$

The collision frequencies of momentum transfer $\nu_{\alpha,\beta}$ between ions, electrons and all other particles β that can collide with it are shown in Table 2.1. Next, we discuss how to solve this system of equations.

2.2 Initial profiles, boundary conditions, and numerical methods

In order to predict the evolution of a system, one needs to define the starting state of the system through initial conditions, or profiles. Furthermore, one must define a set of boundary conditions so that the system can be constrained. Equations (2.1)–(2.9) represent a system of partial differential equations, and cannot be solved analytically. Therefore, a numerical scheme is needed to predict its evolution. Numerical schemes for predicting the behavior of physical systems can become unstable and produce nonphysical behavior if the length of its time step is not constrained in accordance with the highest velocities in the system. All of these are discussed in this section.

2.2.1 Profiles

Neutral density profiles (Figure 2.1b) are provided by the Mars Climate Database [e.g., *Lewis et al.*, 1999]. In order to initialize the density profiles of the ion species (Figure 2.1a), the relative fraction of each ion is used at each altitude z given by the Viking I measurements [e.g., *Hanson et al.*, 1977]. Those profiles, as well as the electron number density profile from [*Lillis et al.*, 2009], are used to build the density profiles in panel (a) used by the model. Approximations of ion densities above 300 km are obtained by fitting [*Chapman*, 1931] functions to the data. Temperature profiles (Figure 2.1c) are built using input from *Lillis et al.* [2009]. The pressure for each species α (Figure 2.1d) is calculated as $p_\alpha = n_\alpha k_\mathrm{B} T_\alpha$, where k_B is the Boltzmann constant.

Model remnant fields are achieved by placing upward directed magnetic dipole(s) with a magnetic moment of $\mu = 10^{16}\,\mathrm{A}\cdot\mathrm{m}^2$ buried 20 km below the surface. This method is consistent with the work done by *Purucker et al.* [2000] and *Langlais et al.* [2004]. On Mars examples of isolated cusps can be seen at (15°N, 15°E) and (10°S, 110°E) and multiple cusps positioned closely together can produce an analog to Terra Sirenum magnetic topology, as evidenced by *Connerney et al.* [1999] and shown in Figure 1.2. Crustal magnetization is frequently organized in East-West trending linear

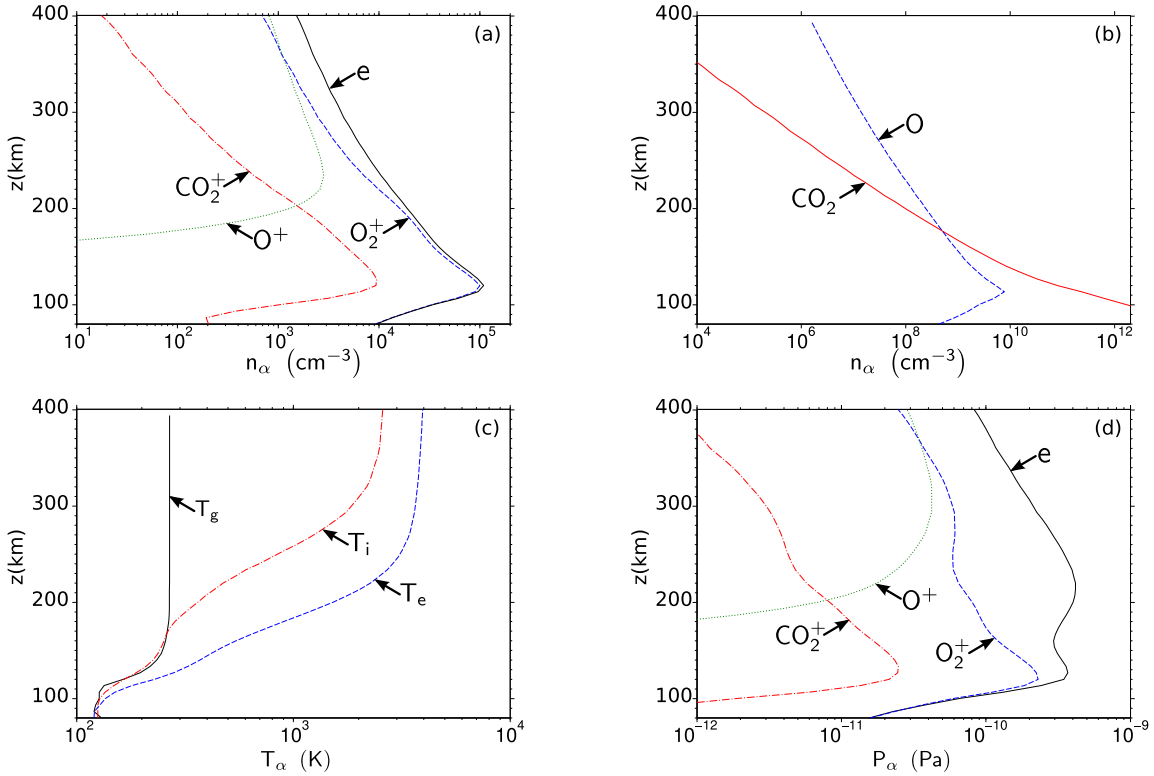

Figure 2.1: Initial profiles used for simulations of the current model [*Riousset et al.*, 2013]. Neutral density profiles in panel (b) are provided by the Mars Climate Database [e.g., *Lewis et al.*, 1999]. The relative fraction of each ion at each altitude z given by the Viking I measurements [e.g., *Hanson et al.*, 1977]. Those profiles, as well as the electron number density profile from [*Lillis et al.*, 2009], are used to build density profiles in panel (a). Approximations of ion densities above 300 km are obtained by fitting [*Chapman*, 1931] functions to the data. Temperature profiles in panel (c) are built using input from *Lillis et al.* [2009]. The pressure for each species α in panel (d) are calculated as $p_\alpha = n_\alpha k_B T_\alpha$.

features, the longest extending over 2000 kilometers.

Relatively simple boundary conditions can be used without significantly influencing processes in the region of interest. Therefore, simple Neumann (null flux) boundary conditions are used for all variables:

$$\frac{\partial f}{\partial n} = 0 \tag{2.10}$$

where f=$\vec{u}_i$, n_i, p_i, p_e, and $\vec{B}$, and $\hat{n}$ is the direction normal to the boundary. Specifically, the value of a variable in a boundary cell is carried from the nearest cell along the direction $-\hat{n}$, effectively leading to a null flux at the boundaries. The same boundary conditions are used for n_e, $\vec{u}_\mathrm{e}$, $\vec{E}$, and $\vec{J}$. This is consistent (even redundant) with Equations (2.5), (2.6), (2.7), and (2.9). However, the presence of the curl operator in (2.7) and (2.9) makes it impractical to explicitly calculate the boundary values of $\vec{J}$, $\vec{E}$, and subsequently $\vec{u}_\mathrm{e}$ from (2.7), (2.9), and (2.5). *Riousset et al.* [2013] establish that more complex boundary conditions lead to similar results when conclusions are drawn after about 5–10 s. Longer time spans than this may result in non-physical results from the reflection of Alfvèn waves off of the domain boundaries.

2.2.2 Discretization and time stepping (CFL conditions)

Equations (2.1)–(2.9) represent a system of partial differential equations, and cannot be solved analytically. Therefore, a numerical scheme is needed to predict its evolution. The convoluted magnetic field makes it necessary to employ a 3-D approach. The system of Equations (2.1)–(2.9) is discretized using a centered difference scheme [e.g., *Gilat*, 2013, Table 8.1]. An iterative fourth order, ten-stage Runge-Kutta method is used to solve the temporal dependence of the model. The time step is recalculated after each iteration to satisfy the Courant-Friedrich-Lewy (CFL) conditions [e.g., *Courant, Friedrichs, and Lewy*, 1967]. In order to avoid nonphysical effects of the magnetohydrodynamic flow, the CFL condition must be met for the hydrodynamical flow of ions and electrons. Each individual species is treated separately for the determination of a CFL criterion. The ion fluid velocity is used to find the critical time step for each ion:

$$\delta t^i_\mathrm{cr} = \min\left(\frac{\delta x}{\max(|u^i_x|)}, \frac{\delta x}{\max(|u^i_y|)}, \frac{\delta x}{\max(|u^i_z|)}\right) \tag{2.11}$$

A similar method is adopted to find the critical time step for electrons:

$$\delta t^\mathrm{e}_\mathrm{cr} = \min\left(\frac{\delta x}{\max(|u^e_x|)}, \frac{\delta x}{\max(|u^e_y|)}, \frac{\delta x}{\max(|u^e_z|)}\right) \tag{2.12}$$

we then compare the critical time step of ions and electrons take the minimum:

$$\delta \mathrm{t}_{\mathrm{CFL}} = \min\left(\delta \mathrm{t}^{\mathrm{i}}_{\mathrm{cr}}, \delta \mathrm{t}^{\mathrm{e}}_{\mathrm{cr}}\right) \tag{2.13}$$

then the time step is updated after each iteration:

$$\delta t = C \delta t_{\mathrm{CFL}} \tag{2.14}$$

C is a safety coefficient, chosen to be 0.1 for this study. Typically, $\delta t \lesssim 1$ ms throughout the simulation. Such a small time step requires many iterations, so the solver is parallelized using the MPI library with the help of the Portable, Extensible Toolkit for Scientific computation (PETSc) [*Balay et al.*, 2018]. Next, we formulate the contributions to the model as part of this thesis.

2.3 Chemistry module

Previous modeling efforts have incorporated chemistry, but often have focused on a planetary scale to observe broader effects of the solar wind interaction with Mars. The multifluid magnetohydrodynamic model of *Najib et al.* [2011] incorporates a chemistry scheme similar to the one in this work, but accounts only for ion-neutral and ion-ion collisions. *Ma et al.* [2004] uses chemistry in a multispecies MHD model, but assumes a single fluid and only accounts for ion-neutral collisions. These works account for effects on a planetary scale, dampening out conditions for the formation of the dynamo. It has been shown that accounting for chemistry can have noticeable affects on ion density distributions. It is worth examining the effects on the dynamo region using the updated version of M^4, as it could change the structure and altitude range of the dynamo region due to the abundance of O^+, O_2^+, CO_2^+, CO_2, and O_2.

2.3.1 Chemical reaction rates

Chemical reactions in an atmosphere can be represented using rates similar to collision frequencies of momentum transfer between neutrals (CO_2 and O), ions (O_2^+, CO_2^+,

and O^+), and electrons. For simplicity, we call these "chemical collision frequencies" or rates; consider an example of the rate of production and destruction of O_2^+:

$$\begin{aligned}\frac{dn_{O_2^+}}{dt} =& \underbrace{k_8 n_{CO_2^+}}_{\nu^S_{O\to O_2^+}} n_O + \underbrace{k_{10} n_{O^+}}_{\nu^S_{CO_2\to O_2^+}} n_{CO_2} - \underbrace{k_5 n_e}_{\nu^L_{O_2^+}} n_{O_2^+} \\ =& \nu^S_{O\to O_2^+} n_O + \nu^S_{CO_2\to O_2^+} n_{CO_2} - \nu^L_{O_2^+} n_{O_2^+},\end{aligned}$$

where k are reaction rates summarized in Table 2.2, 2.3, and 2.4. One can write the source term as a sum of the reactions where neutrals become ions:

$$\frac{dn_{O_2^+}}{dt} = \sum_n \nu^S_{n\to O_2^+} n_n - \nu^L_{O_2^+} n_{O_2^+}$$

More generally, we can write this equation for any species α:

$$\frac{dn_\alpha}{dt} = \sum_n \nu^S_{n\to\alpha} n_n - \nu^L_\alpha n_\alpha$$

This is in fact the continuity equation (2.1), but the method of calculating the source (ν^S) and loss (ν^L) rates is the same for all cases. The chemical collision frequencies are summarized in Tables 2.2, 2.3, and 2.4. Here we examined the rate of production of species, but the source rates $\nu^S_{n\to\alpha}$ and loss rates ν^L_α also contribute to the conservation of momentum and energy equations.

2.3.2 Modified equations

From the collision term in the generalized Boltzmann equation (details in Appendix A), the chemistry source and loss terms appear in all of the conservation equations (2.1), (2.2), (2.3), (2.6), as well as in the generalized Ohm's law (2.9). In the new set of equations (2.15)−(2.19), the green terms (ν^S) are sources, while the red terms (ν^L) are sinks:

$$\frac{\partial n_i}{\partial t} = -\nabla_{\vec{r}} \cdot (n_i \vec{u}_i) + \sum_n \nu^S_{n\to i} n_n - \nu^L_i n_i \tag{2.15}$$

$$\begin{aligned}\frac{\partial \vec{u}_i}{\partial t} =& -\vec{u}_i \cdot \nabla_{\vec{r}} \vec{u}_i + \frac{q_i}{m_i}\left(\vec{E} + \vec{u}_i \times \vec{B}\right) - \frac{\nabla_{\vec{r}} p_i}{m_i n_i} - \frac{\frac{g_{\mathrm{M}}}{a_0}\hat{z}}{\left(1 + \frac{z}{R_{\mathrm{M}}}\right)^2} \\ &+ \sum_n \nu^{\mathrm{S}}_{n\to i} \frac{n_n}{n_i}(\vec{u}_n - \vec{u}_i) + \sum_\beta \nu_{i,\beta}\left(\vec{u}_\beta - \vec{u}_i\right)\end{aligned} \tag{2.16}$$

$$\begin{aligned}\frac{\partial p_i}{\partial t} =& -\gamma_i \nabla_{\vec{r}} \cdot (p_i \vec{u}_i) + (\gamma_i - 1)\,\vec{u}_i \cdot \nabla_{\vec{r}} p_i + \sum_n \nu^{\mathrm{S}}_{n\to i} \frac{m_i}{m_n} \frac{\gamma_i - 1}{\gamma_n - 1} p_n \\ &- \nu^{\mathrm{L}}_i p_i + (\gamma_i - 1) \sum_n \nu^{\mathrm{S}}_{n\to i} m_i n_n \frac{(\vec{u}_n - \vec{u}_i)^2}{2}\end{aligned} \tag{2.17}$$

$$\begin{aligned}\frac{\partial p_{\mathrm{e}}}{\partial t} =& -\gamma_i \nabla_{\vec{r}} \cdot (p_{\mathrm{e}} \vec{u}_{\mathrm{e}}) + (\gamma_{\mathrm{e}} - 1)\,\vec{u}_{\mathrm{e}} \cdot \nabla_{\vec{r}} p_{\mathrm{e}} + \sum_n \nu^{\mathrm{S}}_{n\to \mathrm{e}} \frac{m_{\mathrm{e}}}{m_n} \frac{\gamma_{\mathrm{e}} - 1}{\gamma_n - 1} p_n \\ &- \nu^{\mathrm{L}}_{\mathrm{e}} p_{\mathrm{e}} + (\gamma_{\mathrm{e}} - 1) \sum_n \nu^{\mathrm{S}}_{n\to \mathrm{e}} m_{\mathrm{e}} n_n \frac{(\vec{u}_n - \vec{u}_{\mathrm{e}})^2}{2}\end{aligned} \tag{2.18}$$

$$\begin{aligned}\vec{E} =& -\sum_i \frac{q_i n_i}{q_{\mathrm{e}} n_{\mathrm{e}}} \vec{u}_i \times \vec{B} + \frac{\vec{J} \times \vec{B}}{q_{\mathrm{e}} n_{\mathrm{e}}} - \frac{\nabla_{\vec{r}} p_{\mathrm{e}}}{q_{\mathrm{e}} n_{\mathrm{e}}} + \frac{m_{\mathrm{e}}}{q_{\mathrm{e}}} \sum_n \nu^{\mathrm{S}}_{n\to \mathrm{e}} \left(\vec{u}_n - \vec{u}_{\mathrm{e}}\right) \\ &+ \frac{m_{\mathrm{e}}}{q_{\mathrm{e}}} \sum_n \nu_{n-\mathrm{e}} \left(\vec{u}_n - \vec{u}_{\mathrm{e}}\right) + \frac{m_{\mathrm{e}}}{q_{\mathrm{e}}} \sum_i \nu_{i-\mathrm{e}} \left(\vec{u}_i - \vec{u}_{\mathrm{e}}\right)\end{aligned} \tag{2.19}$$

2.4 Discussion

The M^4 model accounts for collisions for both electrons and ions (O_2^+, CO_2^+, O^+) with neutrals (O, CO_2) in a multifluid MHD formulation. Planetary and solar wind H^+ are neglected for now due to very low densities below 300 km [e.g., *Ma et al.*, 2004], but future plans include expanding the upper domain boundary to study ion loss, which will necessitate the inclusion of H^+. In M^4, ions are treated as individual, yet coupled fluids with conservation laws and equations of state for density, momentum, and pressure. Electron dynamics are obtained from the current density and the plasma approximation as well as the equation of state. The electric field, magnetic field, and current density are obtained from Maxwell-Faraday's, Maxwell-Ampère's, and

generalized Ohm's law. The collision terms appear in the generalized Ohm's law and in the momentum conservation equations, and are the driving force of the formation of the dynamo currents.

In the conservation of ion momentum (2.16), one can see that the sink term does not appear explicitly. However, it can be seen that Equation (2.16) is coupled to Equations (2.15) and (2.17). Specifically, the variables n_i and p_i are present in (2.16), which means that the chemistry loss terms indirectly impact the conservation of momentum. Similarly in the generalized Ohm's law (2.19) the sink term is not present, but (2.19) is coupled to Equation (2.18) through the term p_e. This means that chemistry loss terms do, in fact, affect Ohm's law. One can take this a step further and see that since the electric field is present in Faraday's law, which in turn affects Ampère's law. For now, heat transfer from inelastic collisions are neglected in the conservation of energy equations.

A detailed description of the normalization, or definition of the normalized plasma, is given in Appendix A. Instead of normalizing the plasma depending on one of our three ion fluids, time and length scales in our system are based off of electron parameters. Time scales are defined by the electron gyroperiod. Length scales are based off of the plasma skin depth (also called electron inertial length).

The model inputs assume a constant background neutral profile for CO_2 and O. However, the neutrals are many orders of magnitude larger than the ions in all regions of concern. Therefore, it is reasonable to assume that their concentration would never change enough to make a meaningful impact on simulations. For now it is assumed that the thermal velocity is much greater than kinetic velocities, leading to the temperature profiles being constant.

Photoionization rates ν_1 and ν_3 in Table 2.2 are taken from [*Bößwetter et al.*, 2010] at an EUV index of 1. *Itikawa* [2002, Table 2.2] provides the electron-impact ionization rate of CO_2 through modeling of the cross sections of electron collisions with CO_2, denoted by $\nu_{e-2e}^{CO_2}$. *Lieberman and Lichtenberg* [2005, Table 8.2] provide the electron-impact ionization rate for O. *Schunk and Nagy* [2000], Tables 8.3, 8.4, 8.5 provide rates for dissociation and recombination as well as ion-neutral chemistry. Now that the scheme is implemented into the model, it needs to be tested and validated.

As shown in Table 2.2, the importance of electron-impact ionization is proportional to the temperature of electrons. In fact, this reaction proves to be of limited importance for secondary electrons in the ionosphere, whose temperatures do not exceed 4000 K. However, solar wind electrons can reach these temperatures, and their impact could be noticeable under the right conditions. Rates from [*Bößwetter et al.*, 2010] given in Table 2.2 are available for indexes up to 100 (an extreme case) for photoionization reactions. During intense solar activity, the rates can be up to two orders of magnitude larger. For studies of the early history of Mars, these higher EUV indexes would be more realistic as shown in [*Bößwetter et al.*, 2010].

The chemistry scheme has been introduced and implemented into the model, steps must be taken to ensure that the additions are working correctly. Analytical solutions must be developed and tested against the behavior of the model. This will be the subject of the next chapter.

Table 2.2: Photoionization and electron-impact ionization.

Reaction	Rates (cm^3/s)	Note
$CO_2 + h\nu \longrightarrow CO_2^+ + e$	$\nu_1 = 5.0 \times 10^{-7} \quad (s^{-1})$	[*Bößwetter et al.*, 2010, 1 EUV]
$CO_2 + e \longrightarrow CO_2^+ + e + e$	$k_2 = \nu_{e-2e}^{CO_2} \sqrt{\frac{2k_B T_e}{m_e}}$	[*Itikawa*, 2002]
$O + h\nu \longrightarrow O^+ + e$	$\nu_3 = 2.0 \times 10^{-7} \quad (s^{-1})$	[*Bößwetter et al.*, 2010, 1 EUV]
$O + e \longrightarrow O^+ + e + e$	$k_4 = 9.0 \times 10^{-9} T_e^{0.7} e^{-13.8/T_e}$	[*Lieberman and Lichtenberg*, 2005, Table 8.2]

Table 2.3: Dissociative and radiative recombination.

Reaction	Rates (cm^3/s)	Note
$O_2^+ + e \longrightarrow O + O$	$k_5 = \begin{cases} 2.00 \times 10^{-7} \left(\frac{300}{T_e}\right)^{0.7} & T_e < 1200 \text{ K} \\ 7.38 \times 10^{-8} \left(\frac{1200}{T_e}\right)^{0.56} & T_e > 1200 \text{ K} \end{cases}$	[*Krasnopolsky*, 2002]
$CO_2^+ + e \longrightarrow CO + O$	$k_6 = 4.2 \times 10^{-7} \left(\frac{300}{T_e}\right)^{0.75}$	[*Schunk and Nagy*, 2000, Table 8.3]
$O^+ + e \longrightarrow O + h\nu$	$k_7 = 3.7 \times 10^{-12} \left(\frac{250}{T_e}\right)^{0.7}$	[*Schunk and Nagy*, 2000, Table 8.4]

Table 2.4: Ion-neutral chemistry.

Reaction	Rates (cm^3/s)	Note
$CO_2^+ + O \longrightarrow O_2^+ + CO$	$k_8 = 1.64 \times 10^{-10}$	[*Schunk and Nagy*, 2000, Table 8.5]
$CO_2^+ + O \longrightarrow O^+ + CO_2$	$k_9 = 9.6 \times 10^{-11}$	[*Schunk and Nagy*, 2000, Table 8.5]
$O^+ + CO_2 \longrightarrow O_2^+ + CO$	$k_{10} = 1.1 \times 10^{-9}$	[*Schunk and Nagy*, 2000, Table 8.5]

Chapter 3

Validation of Chemistry

The model introduced in section 2.2 was validated in *Riousset et al.* [2013, 2014]. In this chapter, the analytical solution for the newly implemented chemistry scheme will be developed for the conservation of mass and momentum equations, Equation (2.15) and (2.16). These analytical solutions will then be compared to numerical simulations for the ion-neutral chemistry in Table 2.4. Finally, the significance of these results will be discussed.

3.1 Validation of reaction rates

In this section, the source and loss terms in the conservation of mass (2.15) chemistry source and loss terms are tested and validated. An analytical solution is developed to predict the behavior of the system simplifying the environment, which is then compared to numerical simulation results.

3.1.1 Theoretical solution

Validating the chemistry scheme in the continuity equation is done by testing one chemical reaction at a time from Table 2.2, 2.3, and 2.4. In order to eliminate the advection term in Equation (2.15) and find an analytical solution, uniform ion and density and velocity/wind profiles are used. Only one chemical reaction in each

simulation run is toggled on/off to test individual chemistry rates. For example, if one takes the reaction $O^+ + CO_2 \longrightarrow O_2^+ + CO$ from Table 2.4, the continuity equations (2.15) for O^+ and O_2^+ become ordinary differential equations and can be solved in a straightforward manner. One can obtain an analytical solution for the concentration/density of O^+, which is expected to decrease, as it is a reactant:

$$\frac{dn_{O^+}}{dt} = -\underbrace{k_{10} n_{CO_2}}_{\nu^{\mathrm{L}}_{O^+}} n_{O^+}$$

$$n_{O^+}(t) = n_{O^+,0}\left(e^{-\nu^{\mathrm{L}}_{O^+} t}\right) \tag{3.1}$$

where n_{O^+} is the density of O^+ as a function of time, $n_{O^+,0}$ is the initial density of O^+ in the system. $\nu^{\mathrm{L}}_{O^+}$ is the rate of loss calculated from the density of neutral CO_2 (taken as a constant background value) and the rate coefficient from Table 2.4. One can do the same for O_2^+, which is expected to increase, since it is a product of the reaction:

$$\frac{dn_{O_2^+}}{dt} = \underbrace{k_{10} n_{CO_2}}_{\nu^{\mathrm{L}}_{O^+}} n_{O^+}$$

$$n_{O_2^+}(t) = n_{O_2^+,0} + \nu^{\mathrm{L}}_{O^+} n_{O^+,0}\left(e^{-\nu^{\mathrm{L}}_{O^+} t}\right) \tag{3.2}$$

We see that the concentration of O_2^+ depends not only on its own initial concentration, but also on the population of O^+. In this relationship, the concentration of O_2^+ is expected to continue increasing until there is no more O^+ left to solicit the reaction. There is a 1:1 relationship between the product and the reactant, so the final concentration of O_2^+ will asymptotically converge to the sum of the initial ion densities. These relations are described by the following equations:

$$n_{O^+,\mathrm{final}} + n_{O_2^+,\mathrm{final}} = n_{O^+,0} + n_{O_2^+,0} \tag{3.3}$$

$$n_{O^+,\mathrm{final}} = 0 \tag{3.4}$$

3.1.2 Numerical results

Testing results for the conservation of mass chemistry source and loss terms are shown in Figure 3.1. The three ion-neutral chemical reactions are tested from Table 2.4. Uniform neutral densities of 10^{15} m^{-3} are used while initial ion densities are set three orders of magnitude lower, which is similar to actual composition in lower regions of the Martian ionosphere. Ion and electron temperatures are set to 1000 K. As a result of the uniform temperature and density profiles, the pressure is also uniform. Results are tracked at the center of $7\times7\times15$ simulation cells. Next, a validation of the chemistry source term in Equation (2.16) will be shown.

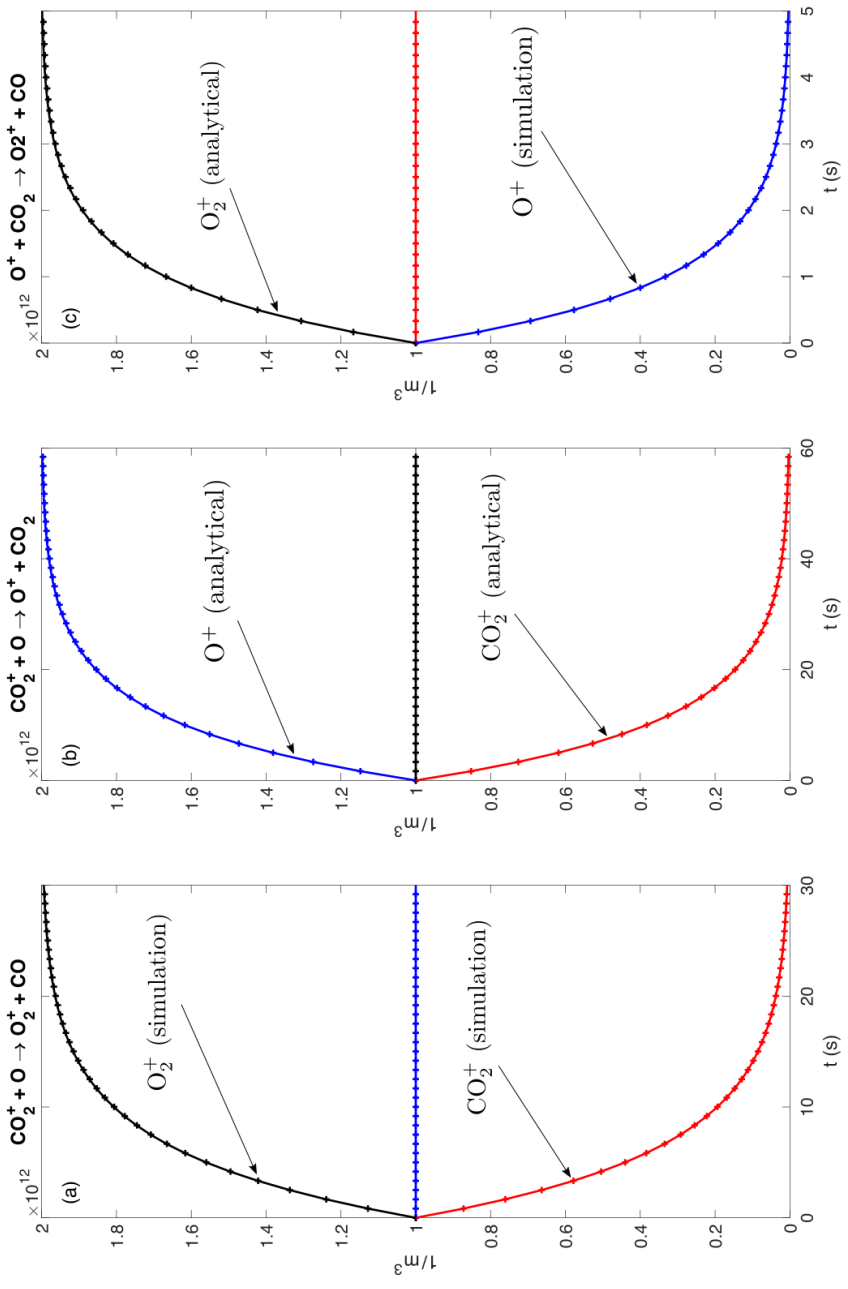

Figure 3.1: Testing results for the conservation of mass chemistry source and loss terms. Three ion-neutral chemical reactions are tested from Table 2.4. Neutral densities of 10^{15} m^{-3} are used while initial ion densities are set three orders of magnitude lower, which is similar to actual composition in lower regions of the ionosphere. Results are tracked at the center of a 7×7×15 domain.

3.2 Validation of response to neutral wind

In this section, the chemistry source term in the conservation of ion momentum (2.16) is tested and validated. An analytical solution is developed to predict the behavior of the system simplifying the environment, which is then compared to numerical simulation results.

3.2.1 Theoretical solution

Validating the chemistry source and loss terms in the momentum equation (2.2) is done by simplifying the system as much as possible so that the effects of chemistry can be analyzed. We note that there exists only a source term in the momentum equation since the loss term now appears through a loss of velocity (see Section A.2). The goal is to turn the complex partial differential equation into a simpler ordinary differential equation, which can be solved analytically. Uniform density and temperature profiles for ions and electrons are used, which means that the gradient pressure term goes to zero. No variation along z is assumed, and the gravitational effects are neglected. Furthermore, all collisions are neglected, so that the only perturbations come from chemistry. Ultimately, Equation (2.2) is reduced to:

$$\frac{\partial \vec{u}_i}{\partial t} = -\vec{u}_i \cdot \nabla_{\vec{r}} \vec{u}_i + \sum_n \nu^{\mathrm{S}}_{n\to i} \frac{n_n}{n_i} (\vec{u}_{\mathrm{n}} - \vec{u}_i)$$

We provide a constant uniform neutral wind directed only in the x (North-South) direction, and an initial ion wind of zero in all directions. As the momentum equation evolves, the ion velocity will only possess a nonzero component in the x direction, and the advective term reduces to a linear spacial derivative, which is zero due to simplified isotropic and uniform ion wind conditions. Last, no magnetic field is introduced into the system, which leads to Equations (2.7)–(2.9) becoming zero. A one-dimensional ordinary differential equation is left:

$$\frac{du_{i,x}}{dt} = \sum_n \nu^{\mathrm{S}}_{n\to i} \frac{n_n}{n_i} (u_{n,x} - u_{i,x})$$

We further assume a zero initial ion wind in order to simplify the analytical solution:

$$u_{i,x}(t) = u_{n,x}\left[1 - \exp\left(-\sum_n \nu^{\mathrm{S}}_{n\to i}\frac{n_n}{n_i}t\right)\right] \tag{3.5}$$

3.2.2 Numerical results

We adopted the same initial conditions in temperature, pressure, and density as in Section 3.1. As a result of the uniform temperature and density profiles, the pressure is also uniform. Initial ion wind/velocity is set to zero in all directions, while a constant uniform neutral wind of 10 m/s in the positive x (northern) direction is provided. Results are tracked at the center of a 7×7×15 domain. Next, we discuss the conclusions we can draw from the findings of this chapter.

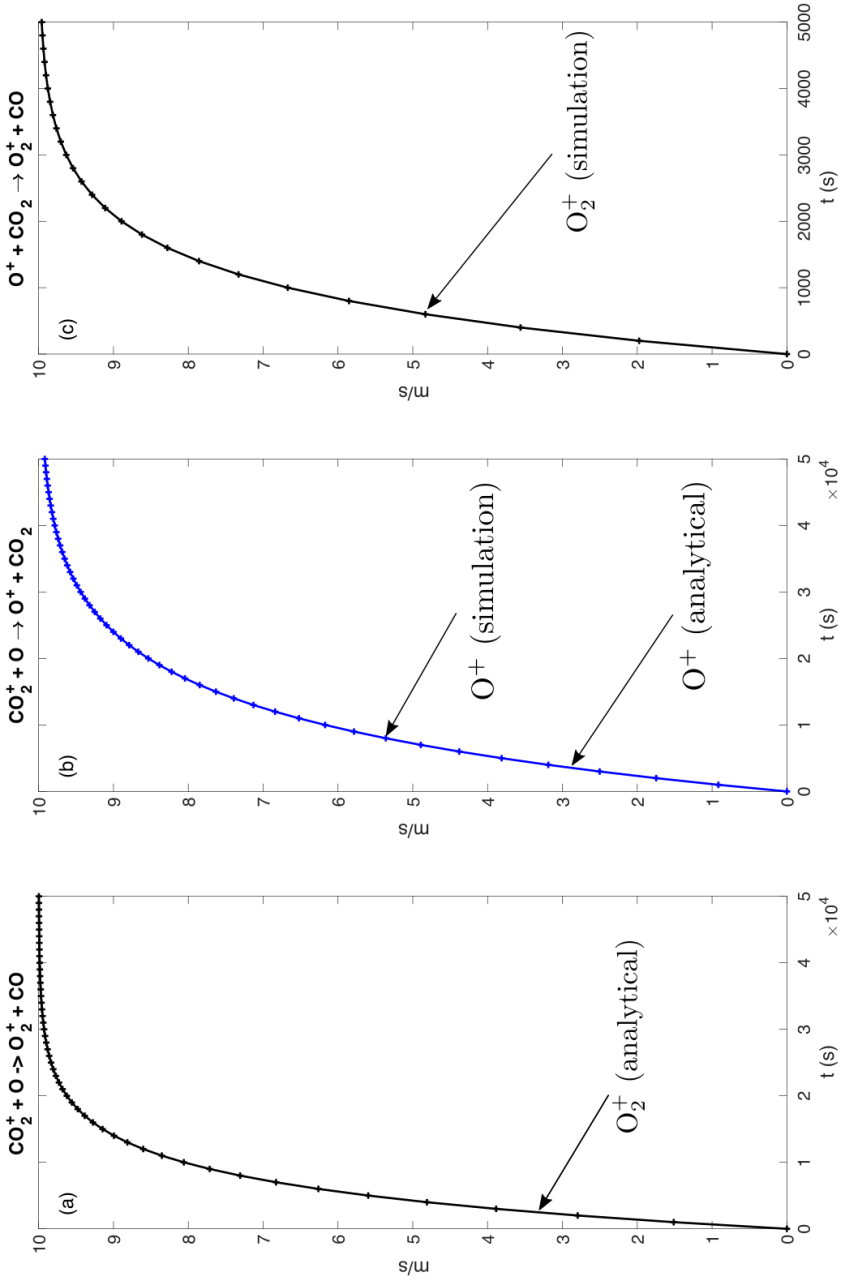

Figure 3.2: Testing results for the conservation of momentum chemistry source terms. Three ion-neutral chemical reactions are tested from Table 2.4. Neutral densities of 10^{15} m^{-3} are used while initial ion densities are set to 10^{12} m^{-3}. Initial ion wind/velocity is set to zero in all directions, while a constant uniform neutral wind of 12 m/s in the positive x (northern) direction is provided. Results are tracked at the center of a $7\times7\times15$ domain.

3.3 Discussion

Reactions in Figures 3.1a and 3.1b appear to be considerably slower than in Figure 3.1c. However, in lower regions of the ionosphere between 100 and 200 km O is present in higher concentrations than CO_2 which can cause reactions involving O to occur on much faster timescales. Figure 3.1 shows that the simulations agree very well with the predicted steady state of the system given by Equation (3.3) and (3.4). The time that it takes the system to reach steady state is proportional to the chemical collision frequency, which varies depending on the reaction being considered.

The neutral wind velocity is treated as an input parameter by the model. For the sake of simplicity, we assume uniform initial wind velocity throughout the simulation domain. Equation (3.5) tells us that the ion wind will asymptotically converge to the neutral wind speed. Figure 3.2 shows that the simulations agree very well with the predicted steady state of the system, where the ion speed converges and eventually reaches the neutral wind speed. The time that it takes the system to reach steady state is inversely proportional to the chemical collision frequency, which vary depending on the reaction being considered. For these simulations, our chosen boundary conditions preserve the uniformity of the ion wind everywhere in the domain.

After the chemistry scheme has been tested and validated, we focus on the behavior of the model as compared to previous simulations performed by *Riousset et al.* [2014] to establish the impact of chemistry on the Martian ionospheric dynamo currents.

Chapter 4

Effect of Chemistry in Dynamo Region

This chapter begins by observing the effect of chemistry on the ion density profile without any external magnetic or collisional effects. Then the effect of chemistry is examined with three cases investigated previously by *Riousset et al.* [2013, 2014]. First, a uniform vertical magnetic field will be introduced to the system along with a neutral wind. Next, a single dipole magnetic field will be placed in the center of the system while maintaining a neutral wind identical to the first case. In this chapter, the positive and negative x direction signify North and South directions, while the positive and negative y direction represents East and West, respectively.

4.1 Control run: Simulation with no magnetic field or wind

In Chapter 3 we examined the effect of individual chemical reactions without any variations in space. In this section, we discern if a steady state can be reached when the full chemistry scheme is used. Then we employ the density, temperature, and pressure profiles shown in Section 2.2.1. A magnetic field will not be employed, nor will a neutral or ion wind be introduced. This means that the problem is effectively

one dimensional in space.

4.1.1 Simulation setup

For the first simulation ran in this section, a simulation grid consisting of 7×7×15 points is used. In the first, none of the profiles shown in Figure 2.1 are employed. Neutral densities are assumed to be 10^{15} m^{-3} with ion densities of 10^{12} m^{-3}. Electron and ion temperatures are set to 1000 K, similar to Chapter 3. No magnetic field configuration is present, nor is there any neutral/ion wind given. No effects due to gravity are present, and due to the uniform temperature and density profiles, the pressure is also uniform. Therefore, there is no variation of any parameter along the x, y, or z direction. Chemistry is activated to observe whether or not a steady state will be reached with the given parameters.

In the second simulation, a 200×200×300 km grid is employed with a resolution of δx=δy=20 km and δz=5 km over an altitude range of 100−400 km. The initial profiles shown in Figure 2.1 are employed. However, no magnetic field is present, and no neutral/ion wind is given. There will be variations of density, temperature, and pressure along z. We also consider the effects of gravity. Essentially we seek to model a full atmosphere without any magnetic field or wind (i.e., collisional effects will be minimal). The system will only vary along the z direction. Results will be shown for runs with and without the chemistry scheme turned on.

4.1.2 Results

Results for ion densities for the "one-dimensional" case with chemistry turned on are shown in Figure 4.1. It is seen that the system reaches a steady state after approximately 15 s. This time to reach steady state will be denoted as τ, and results for future simulations will be drawn after times proportional to τ. The species O_2^+ is the most abundant, followed by CO_2^+ and last by O^+.

Simulation results of density profiles of all species utilizing complete profiles when chemistry is turned on/off are shown in Figures 4.2a and 4.2b, respectively. Results are plotted at 90 s (6τ). No magnetic field or ion/neutral wind is provided and as a

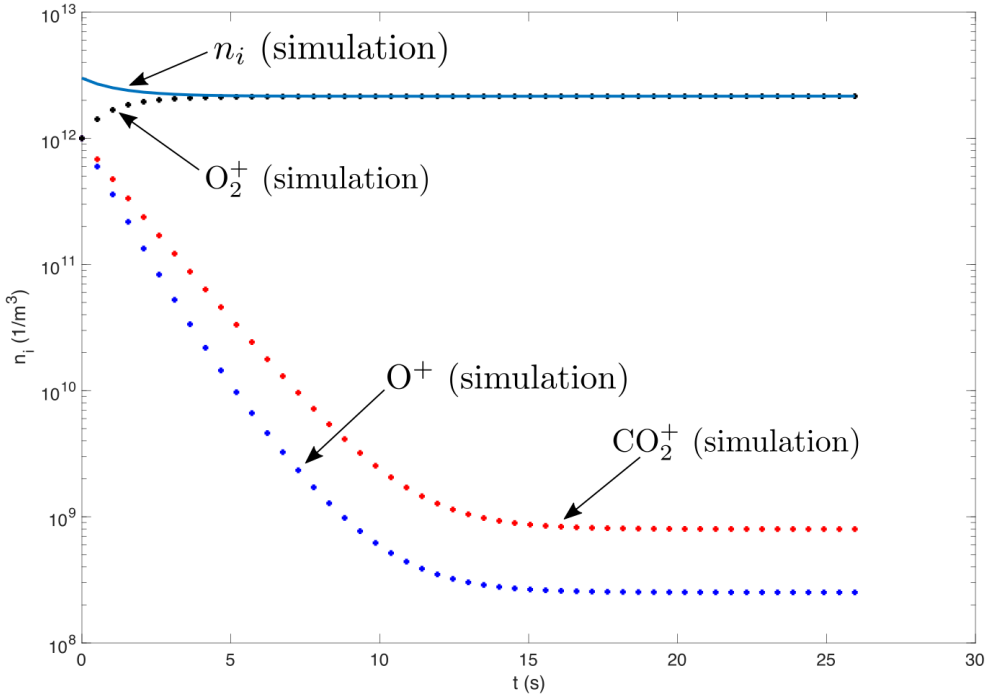

Figure 4.1: Steady state results for chemistry. Electron and ion temperatures of 1000 K are used. Uniform neutral densities of 10^{15} m^{-3} are used while initial uniform ion densities are set three orders of magnitude lower (10^{12} m^{-3}).

result, collisional effects will be small. Figure 4.2a shows the results when chemistry is not utilized, and 4.2b shows the population distributions when chemistry is toggled on.

It should be noted that neutral densities are assumed to be constant in the background when the chemistry scheme is activated. As seen in Figure 2.1, neutral (O, CO_2) densities are 3+ orders of magnitude larger than ion densities throughout the ionosphere. Knowing this, it is assumed that any changes in neutral populations as compared to ions due to chemistry are negligible.

4.1.3 Discussion

In Figure 4.2, there are substantial differences when the chemistry scheme is turned on in Figure 4.2b as compared to when the scheme is not utilized in Figure 4.2a. First, the concentration of O^+ is similar down to ∼250 km altitude; below this, there is another region of O^+ seen, with densities higher than expected extending into the predicted dynamo region. The peak density of O^+ increases by about 30 km with chemistry. O_2^+ populations are an order of magnitude larger at lower altitudes with the chemistry scheme, and the peak region is observed about 30 km lower. Arguably the most noticeable impact of the chemistry scheme is on concentrations of CO_2^+, especially at sub 150 km altitudes. As seen in Figure 4.2b, there is no longer a peak density of CO_2^+, which means there is no longer a peak electron density. We should expect a Chapman profile and hence a cut-off, why it doesn't appear is an unresolved question perhaps indicative of a missing loss process for CO_2^+. Another possible conclusion is the need for a better model of the Martian neutral atmosphere from the ground up. Next, we should examine the effect of this new profile when we introduce a simple uniform magnetic field along with a neutral wind.

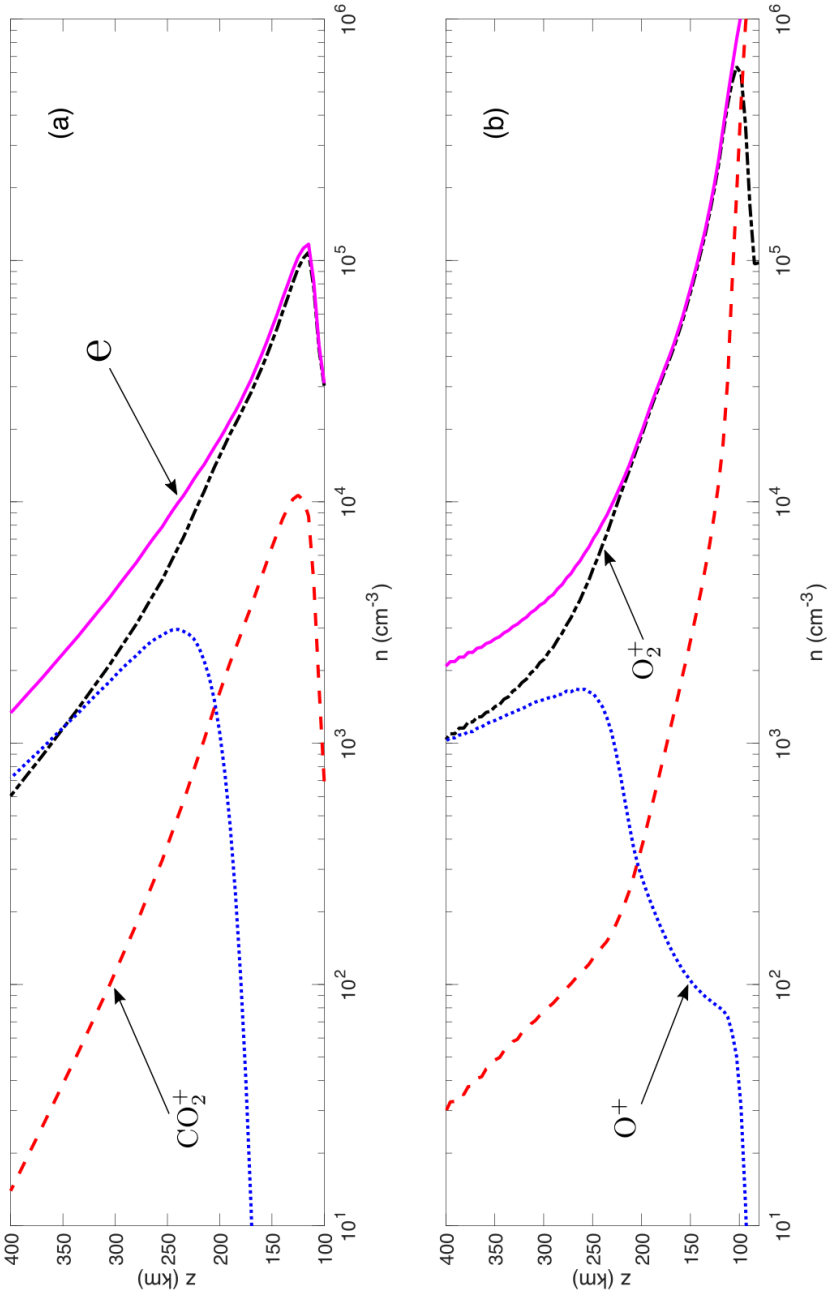

Figure 4.2: Simulation results of density profiles of charged species utilizing complete profiles when chemistry is turned on/off (panels (a) and (b), respectively). No magnetic field or ion/neutral wind is provided. Densities are in particles per cubic centimeter. Panel (a) is when chemistry is not utilized. Panel (b) shows the population distribution when chemistry is activated. Results are drawn at 90 s (6τ).

4.2 Uniform magnetic field

Now we build upon Section 4.1 by introducing a uniform magnetic field in the z direction along with a neutral wind in the North-South, or positive x direction. We will observe where the dynamo region forms compared to the collisional model. Such conditions have been observed by MGS in the nighttime Northern hemisphere as a result of solar wind magnetic field draping [e.g., *Crider et al.*, 2004].

4.2.1 Simulation Setup

For uniform magnetic field simulations, a 400×400×300 km grid is employed with a resolution of δx=δy=20 km and δz=5 km over an altitude range of 100−400 km. A uniform magnetic field of 20 nT is inserted in the positive z direction. Full profiles are employed as shown in Figure 2.1. A uniform neutral wind of 100 m/s in the positive x direction is given, which is consistent with Mars GCM models [e.g., *Forget et al.*, 1999]. Collisional effects are included in all simulation runs, and comparisons are made when chemistry is turned on/off.

4.2.2 Results

For all simulations, conclusions are drawn at t=90 s (6τ). In Figures 4.5−4.8, magenta lines are traced magnetic field lines. Black arrows denote directions of current, electric field, and ion/electron velocities, respectively. The size of solid arrows reflect the magnitude of the value being plotted. Panel (d) illustrates a three-dimensional slice at x=0 km, y=0 km, and z=165 km. Panels (a), (b), and (c) show the individual cuts of the xz, xy, and yz planes, respectively. Current density results without chemistry are shown in Figure 4.5, while results with chemistry are shown in Figure 4.6. Electric field results with chemistry are shown in Figure 4.7. Electron velocity results with chemistry are shown in Figure 4.8.

Figure 4.3 shows an altitude profile of the magnitude of the current density tracked at the center of the xy plane along z. The dashed black line represents the current density results with the chemistry scheme activated, while the solid black line denotes

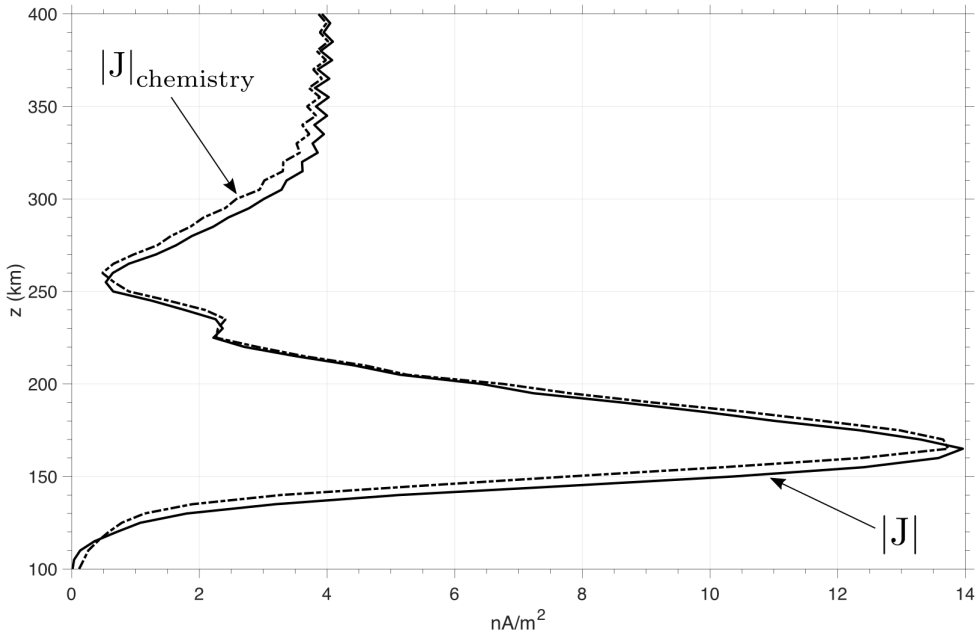

Figure 4.3: Profile of the current density along the vertical direction z. A 20 nT magnetic field directed in the positive z direction is given. A neutral wind of 100 m/s in the x direction is applied, consistent with Mars GCM models [e.g., *Forget et al.*, 1999]. The dashed black line represents the current density results with the chemistry scheme activated, while the solid black line denotes the current density without the chemistry scheme.

the current density without the chemistry scheme. An altitude profile of the magnetic field perturbations tracked at the center of the xy plane are shown in Figure 4.4. Blue lines denote the x component of the perturbation of $\vec{B}$. Magenta lines denote the y component of the disturbance of $\vec{B}$. Dashed and solid lines represent results with and without chemistry, respectively.

4.2.3 Discussion

As seen in Figure 4.5 and predicted in Figure 1.4, in the presence of a uniform vertical magnetic field of 20 nT, dynamo currents form approximately between 150 and 200 km altitude. The strength of these currents are on the order of 10 nA/m^2, which agrees with predictions made by *Withers* [2008]. Currents form in the x plane, as

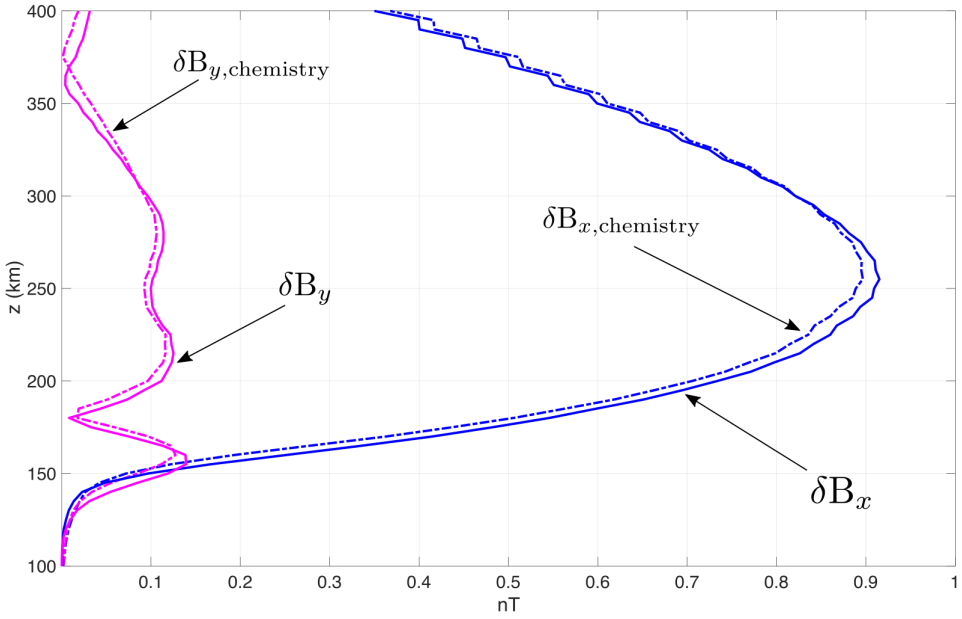

Figure 4.4: Profile of the magnetic field perturbation along the vertical direction z. A 20 nT magnetic field directed in the positive z direction is given. A neutral wind of 100 m/s in the x direction is applied, consistent with Mars GCM models [e.g., *Forget et al.*, 1999]. Blue lines denote the x component of the perturbation of B. Magenta lines denote the y component of the disturbance of B. Dashed and solid lines represent results with and without chemistry, respectively. There is no δB_z, hence it is not shown.

expected due to collisional effects of a neutral wind in the x-direction. Also, currents are seen building up in the negative y direction due to the $\vec{J} \times \vec{B}$ term in Equation (2.19).

When the chemistry is accounted for (Figure 4.6), a dynamo current is also seen to form between 150 and 200 km. Figure 4.3 shows that the peak dynamo current with the chemistry scheme is shifted up by about 10 km. These currents form from differential motions of electrons and ions, which then cause perturbations of the magnetic field. Plots of these perturbations in Figure 4.4 show that there exist disturbances of the magnetic field in both the x and y direction. Electric fields (shown in Figure 4.7) cause these effects on the magnetic field geometry, as defined in Faraday's law (2.8).

From the generalized Ohm's law (2.19), the motions of ions in the positive x direction help to "pull" the magnetic field leading to currents building up over time in the x plane. These currents then lead to further "twisting" of the field in the y direction due to the $\vec{J} \times \vec{B}$ Hall term. The "wiggles" seen in these figures are attributed to numerical resolution, finer resolutions are shown to progressively reduce this behavior. This process is important for the formation of currents when more complex magnetic field geometries are introduced to the system, which will be examined next.

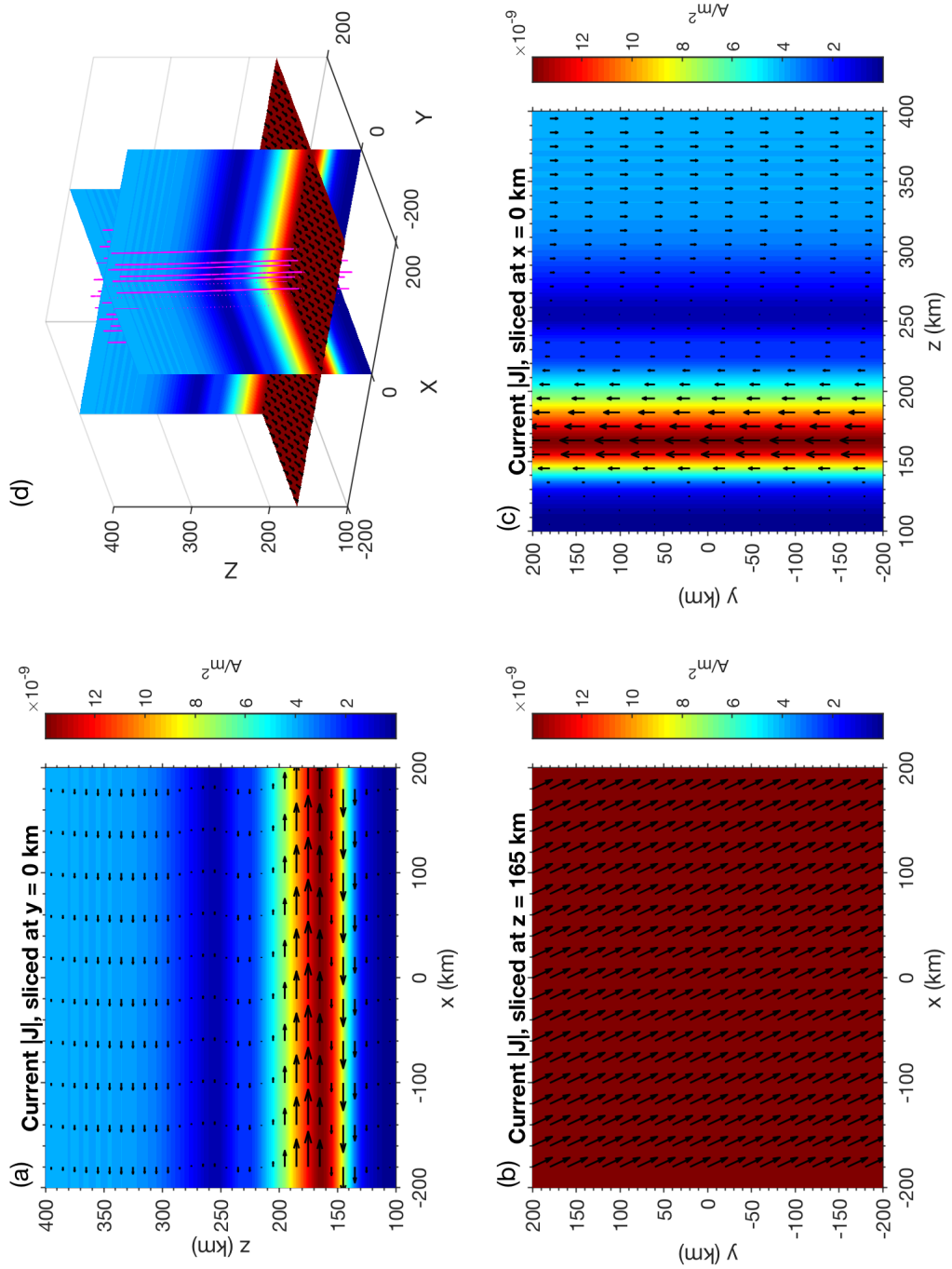

Figure 4.5: Simulation results without chemistry showing the magnitude of the current density at t=90 s (6τ). A 20 nT magnetic field directed in the positive z direction is given. A neutral wind of 100 m/s in the x direction is applied, consistent with Mars GCM models [e.g., *Forget et al.*, 1999]. Black arrows denote direction of the current. Panel (d) shows a three-dimensional view of slices at x=0 km, y=0 km, and z=165 km. Magenta lines in panel (d) are traced magnetic field lines. Panels (a)−(c) are slices along the x, z, and y direction, respectfully. Deep red shading seen between 150 and 200 km altitudes indicate regions of strongest current. Dark blue regions such as that seen at approximately 250 km show weak or zero currents.

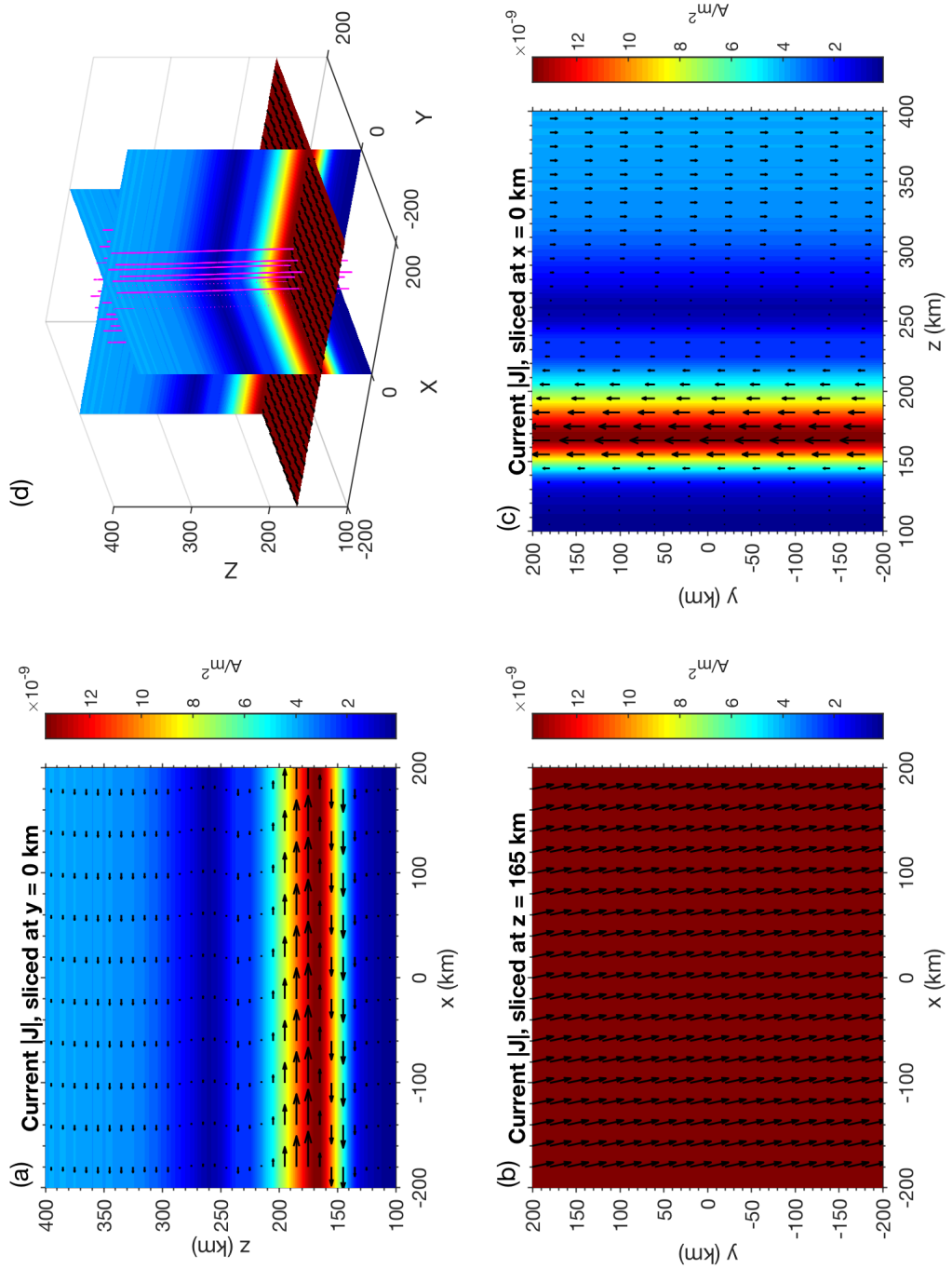

Figure 4.6: Simulation results with chemistry showing the magnitude of the current density at t=90 s (6τ). A 20 nT magnetic field directed in the positive z direction is given. A neutral wind of 100 m/s in the x direction is applied, consistent with Mars GCM models [e.g., *Forget et al.*, 1999]. Black arrows denote direction of the current. Panel (d) shows a three-dimensional view of slices at x=0 km, y=0 km, and z=165 km. Magenta lines in panel (d) are traced magnetic field lines. Panels (a)−(c) are slices along the x, z, and y direction. Deep red shading seen between 150 and 200 km altitudes indicate regions of strongest current. Dark blue regions such as that seen at approximately 250 km show weak or zero currents.

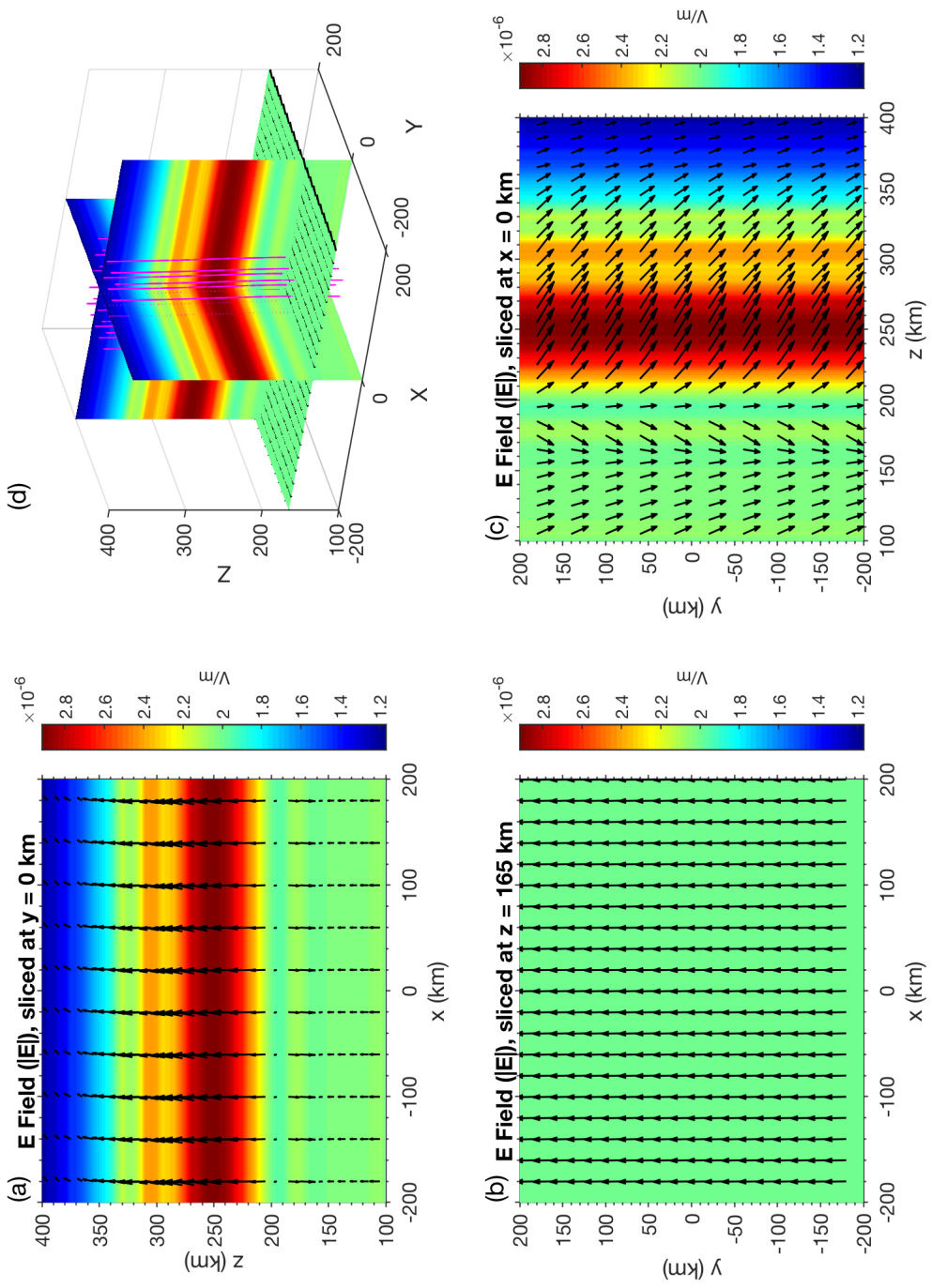

Figure 4.7: Simulation results with chemistry showing the magnitude of the electric field at t=90 s (6τ). A 20 nT magnetic field directed in the positive z direction is given. A neutral wind of 100 m/s in the x direction is applied, consistent with Mars GCM models [e.g., *Forget et al.*, 1999]. Black arrows denote direction of the electric field. Panel (a) shows a slice of the xz plane at y=0 km. Panel (b) shows a slice of the xy plane at z=165 km. Panel (c) shows a slice of the yz plane at x=0 km. Strong fields are highlighted in red, such as those seen at 250 km. Weaker electric fields are shown in dark blue, observed at 400 km.

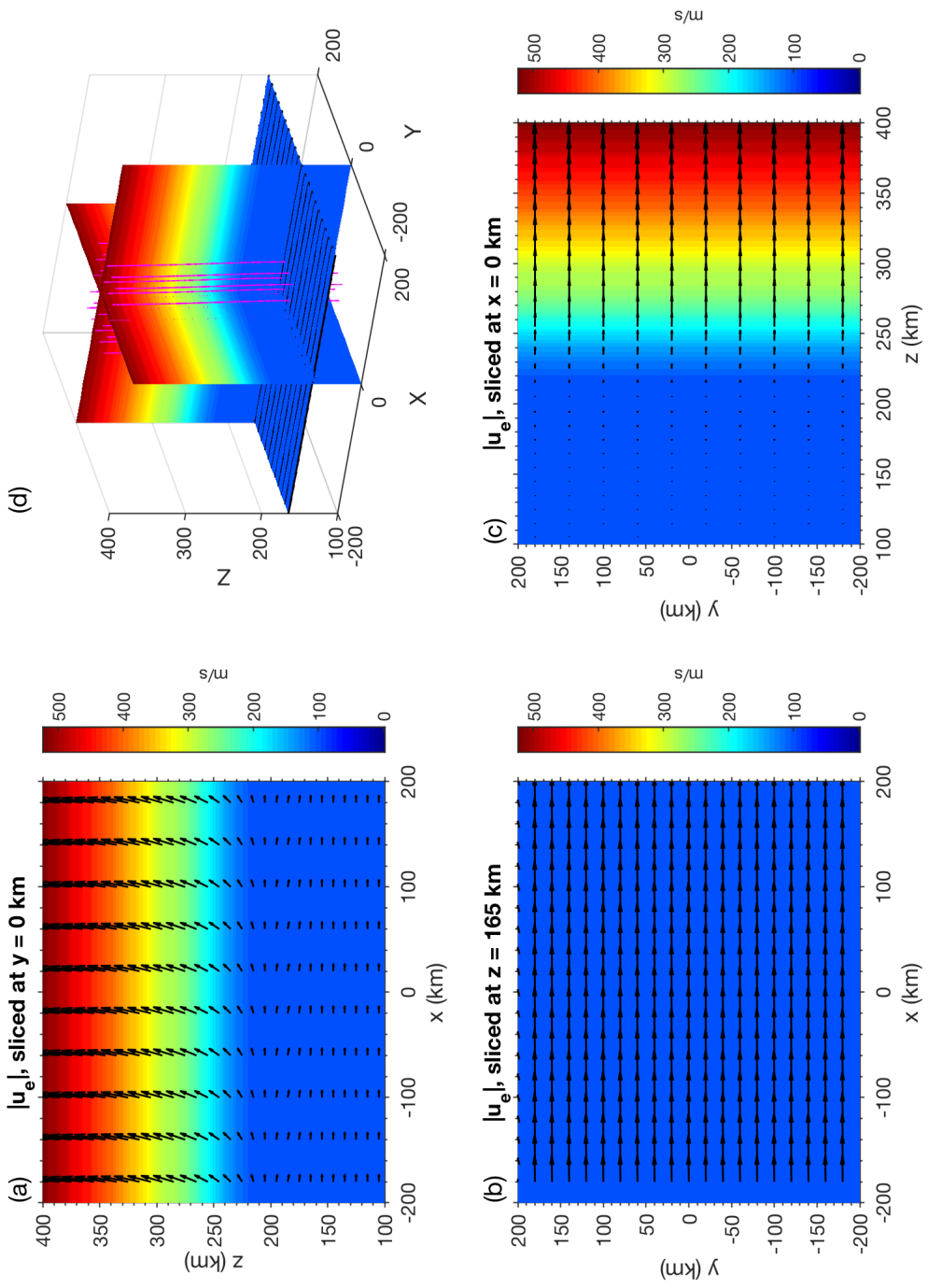

Figure 4.8: Electron velocity results for the uniform magnetic field case with chemistry at t=90 s (6τ). A neutral wind of 100 m/s in the x direction is applied, consistent with Mars GCM models [e.g., *Forget et al.*, 1999]. Black arrows denote direction of the electrons. Panel (d) shows a three-dimensional view of slices at x=0 km, y=0 km, and z=165 km. Magenta lines in panel (d) are traced magnetic field lines. Panels (a)−(c) are slices along the x, z, and y direction. At higher altitudes, large electron velocities are colored in red. At lower regions of the domain, electron velocities are more akin to the neutral wind, and so are denoted in blue.

4.3 Magnetic cusp

The uniform magnetic field is now replaced with a dipole, or cusp, placed below the surface of the simulation domain. These dipoles are analogous to structures observed at (15°N, 15°E) and (10°S, 110°E), and are building blocks for more complex structures. The same neutral wind as in the previous section is used. The addition of a dipole field now produces variations in three dimensions. We will examine the chemistry effects on currents, electric fields, electron and ion velocities, and electron pressure.

4.3.1 Simulation setup

For cusp simulations, a 400×400×300 km grid is employed with a resolution of δx=δy=20 km and δz=5 km over an altitude range of 100−400 km. A magnetic dipole with a magnetic moment of μ=10^{16} $\mathrm{A \cdot m^2}$ is inserted at z=-20 km at the center of the xy plane. Full profiles are employed as shown in Figure 2.1. A uniform neutral wind of 100 m/s in the positive x direction is given. Collisional effects are included in all simulation runs, and comparisons are made when chemistry is turned on/off.

4.3.2 Results

For chemistry and non-chemistry cases, all simulation results are drawn at t=30 s (2τ). Magenta lines in in all figures are traced magnetic fields. Black arrows denote directions of current, electric field, and ions/electrons.

Current density and electric field results without chemistry are shown in Figure 4.14 and 4.15. Panel (d) is a three-dimensional view of three slices at x=0 km, y=0 km, and z=120 km. Panels (a), (b), and (c) show the individual cuts of the xz, xy, and yz planes, respectively. Electron velocity and O_2^+ velocity results without chemistry are shown in Figures 4.9 and 4.10, respectively. Results are tracked on the xy plane at z=120 km.

Current density and electric field results with chemistry are shown in Figure 4.16

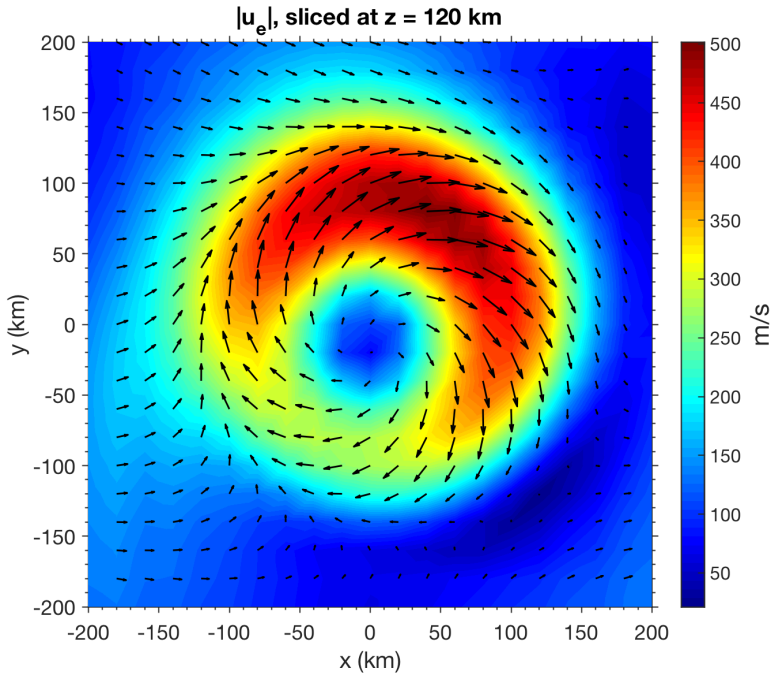

Figure 4.9: Electron velocity results for the magnetic cusp case without chemistry at t=30 s (2τ). Results are tracked on the xy plane at z=120 km. Dipole placed at z=-20 km at the center of the xy plane. A neutral wind of 100 m/s in the positive x direction is applied. Black arrows denote direction of the electrons.

and 4.17. Panel (d) represents a three-dimensional view of slices at x=0 km, y=0 km, and z=105 km. Panels (a), (b), and (c) represent the individual cuts of the xz, xy, and yz planes, respectively. Electron velocity and O_2^+ velocity results are seen in Figures 4.11 and 4.12, respectively. Results are tracked on the xy plane at z=105 km.

Simulation results for the cusp case showing the electron pressure profile with and without chemistry are shown in Figure 4.13. Dashed lines represents the electron pressure with chemistry, while the solid line shows the electron pressure without chemistry. Results are tracked at the center of the xy plane.

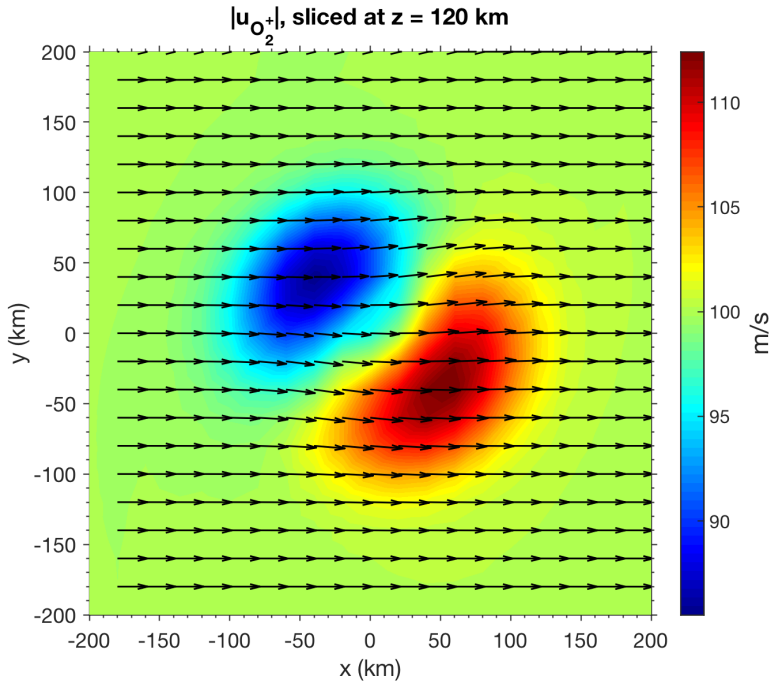

Figure 4.10: O_2^+ velocity results for the magnetic cusp case without chemistry at t=30 s (2τ). Results are tracked on the xy plane at z=120 km. Dipole placed at z=-20 km at the center of the xy plane. A neutral wind of 100 m/s in the positive x direction is applied. Black arrows denote direction of the ions.

4.3.3 Discussion

Without the chemistry scheme, Figure 4.14 shows a distinct current forming around the magnetic cusp between 110 and 150 km. These currents are substantial, on the order of 1 μA. Figure 4.14b specifically shows the concentration of the current that has built up around the dipole. Comparing this with Figure 4.16 we see that with chemistry a current buildup around the cusp is also observed. The current forms much lower in the grid around 105 km, and is much more concentrated around the center of the cusp with an outer boundary approximately 50 km smaller than when chemistry is neglected. The current is noticeably more asymmetrical, which is possibly numerical in nature. The strength of the dynamo current is comparable to before on the Southwest side of the cusp. This is possibly due to the increased concentration of charged species.

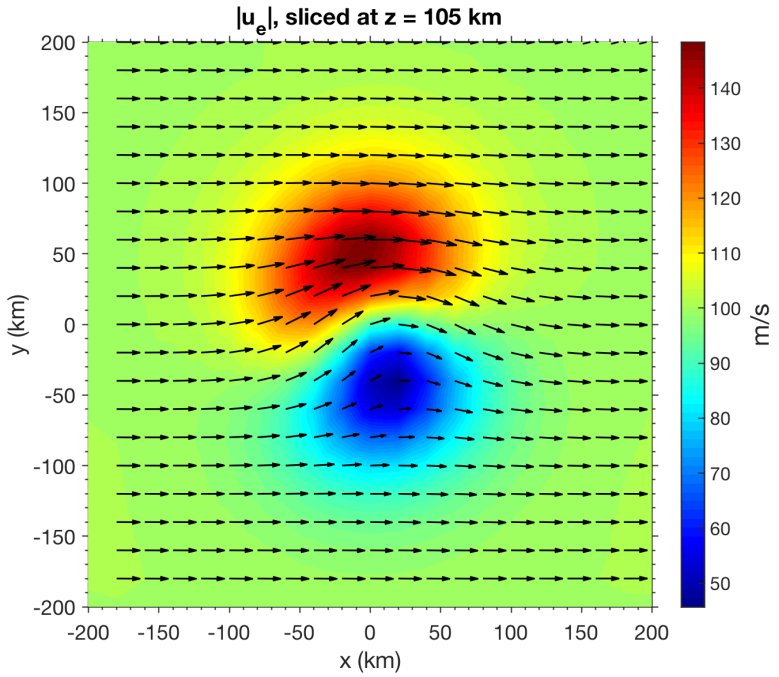

Figure 4.11: Electron velocity results for the magnetic cusp case with chemistry at t=30 s (2τ). Results are tracked on the xy plane at z=105 km. Dipole placed at z=-20 km at the center of the xy plane. A neutral wind of 100 m/s in the positive x direction is applied. Black arrows denote direction of the electrons. Red shading indicates high particle velocities up to 150 m/s for electrons. Regions colored in blue indicate velocities as low as 50 m/s for electrons.

Electric fields are important to understanding the formation of currents, as described in the generalized Ohm's law (2.19) and seen in Figure 4.15. This electric field causes perturbations in the magnetic field as described by Faraday's law (2.8). Subsequently, Ampere's law (2.7) explains how this "pulling" of the field leads to a building up of currents. Figure 4.17 shows that the electric field no longer has the same geometry as before when chemistry is considered. The electric field is almost entirely concentrated on the East side of the cusp. However, where the field is present, it is comparable in magnitude to those seen in Figure 4.15.

The motion of electrons are key to the generation of these electric fields through the $\vec{u}\times\vec{B}$ term in equation (2.19). Electrons are magnetized as seen in Figure 4.9, circulating around the cusp. Notice that the speed of the electrons is higher on

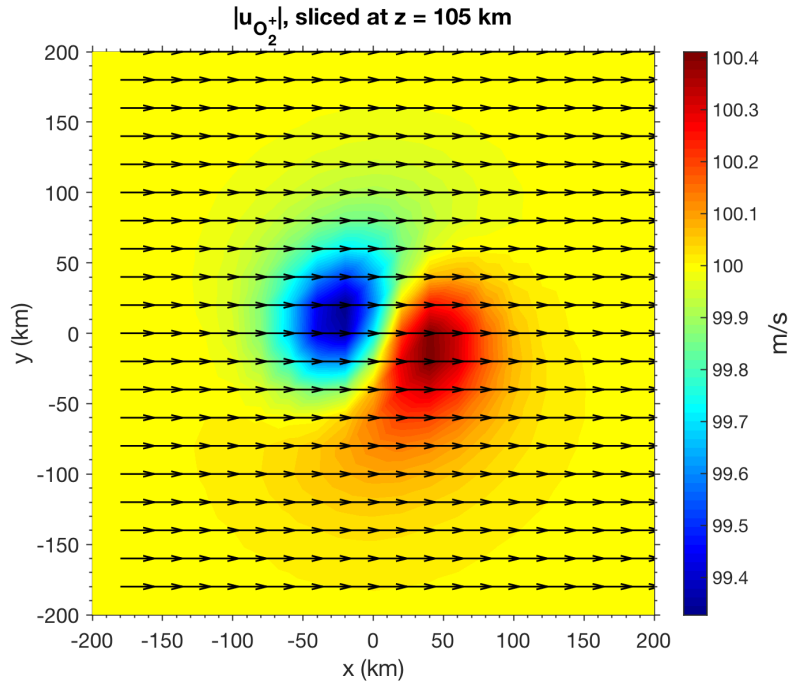

Figure 4.12: O_2^+ velocity results for the magnetic cusp case with chemistry at t=30 s (2τ). Results are tracked on the xy plane at z=105 km. Dipole placed at z=-20 km at the center of the xy plane. A neutral wind of 100 m/s in the positive x direction is applied. Black arrows denote direction of the ions. Ion velocities do not vary by more than 0.5 m/s.

the Northwest side of the cusp than on the Southeast. This is due to ion motion in the North direction and the direction of the dynamo current (clockwise around the cusp), as shown by the conduction current definition (2.5). On the Northwest side of the cusp, the electrons are motivated by the current to move in the same Northward direction as the ion wind. Southeast of the cusp, the direction of the current (Southward) is opposite to that of the ion wind, leading to a reduced speed. In Figure 4.10, ions are demagnetized and flowing with the direction of the neutral wind. with the chemistry scheme, the electrons are only partially magnetized as seen in Figure 4.11, and are moving more than 300 m/s faster compared to previous simulations. The ions are still demagnetized as expected from Figure 4.12.

Electron pressure may also be important for the generation of electric fields necessary to distort the magnetic field, leading to currents. Electron pressure profiles

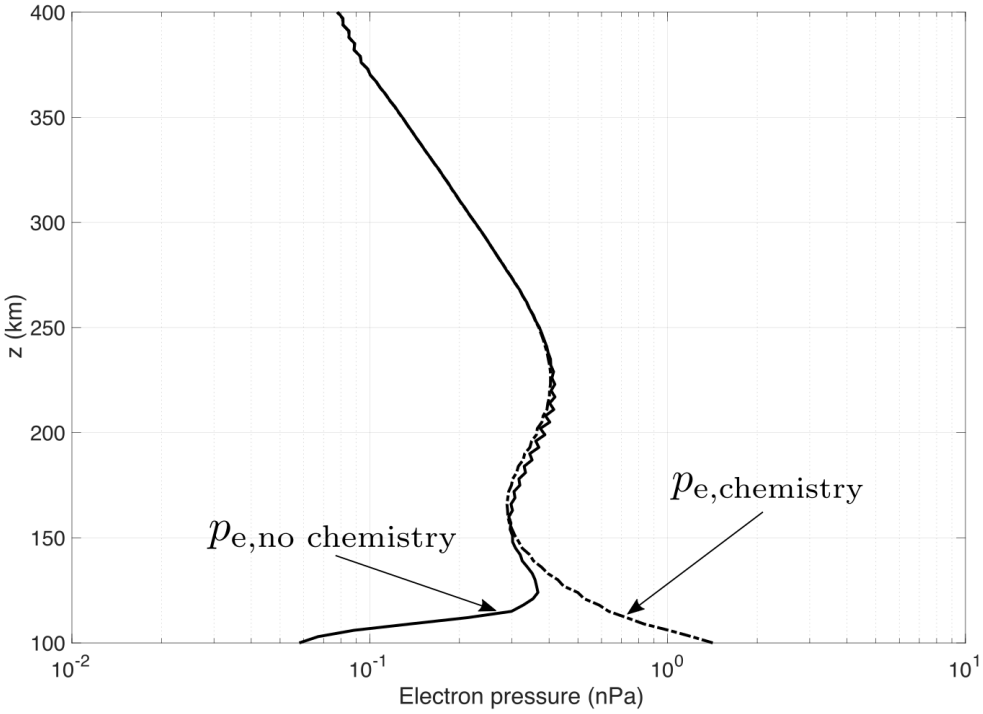

Figure 4.13: Simulation results for the cusp case showing the electron pressure profile with and without chemistry at t=30 s (2τ). Dashed lines represents the electron pressure with the chemistry scheme, while the solid lane shows the electron pressure without the chemistry scheme. Results are tracked at the center of the xy plane.

for chemistry simulation (Figure 4.13) show a stark difference in electron pressure below 150 km as compared to runs without chemistry. There is no inflection point in the electron pressure at 125 km for the chemistry case. It is hypothesized that this turning point in the electron pressure is important due to the gradient pressure term $\nabla_{\vec{r}} p_{\mathrm{e}}$ in equation (2.19). The "wiggles" seen in Figure 4.13 are attributed to numerical resolution. Higher resolutions are shown to progressively reduce this behavior, especially when chemistry is toggled on. Lower in the grid the pressure for chemistry runs is up to an order of magnitude larger than in the non chemistry simulation. Also, recall from the ion and electron profiles (Figure 4.2), there no longer exists a peak electron density region. It is very likely that due to the lack of an electron pressure/density inflection point between 100 and 150 km, there is no longer

an observable lower boundary of the dynamo region within our domain. This seems unlikely, and could be attributed to two reasons: either (a) we are missing a reaction that would destruct CO_2^+ and be consistent with a Chapman profile, or (b) our initial profiles for ions and neutrals need to be revisited.

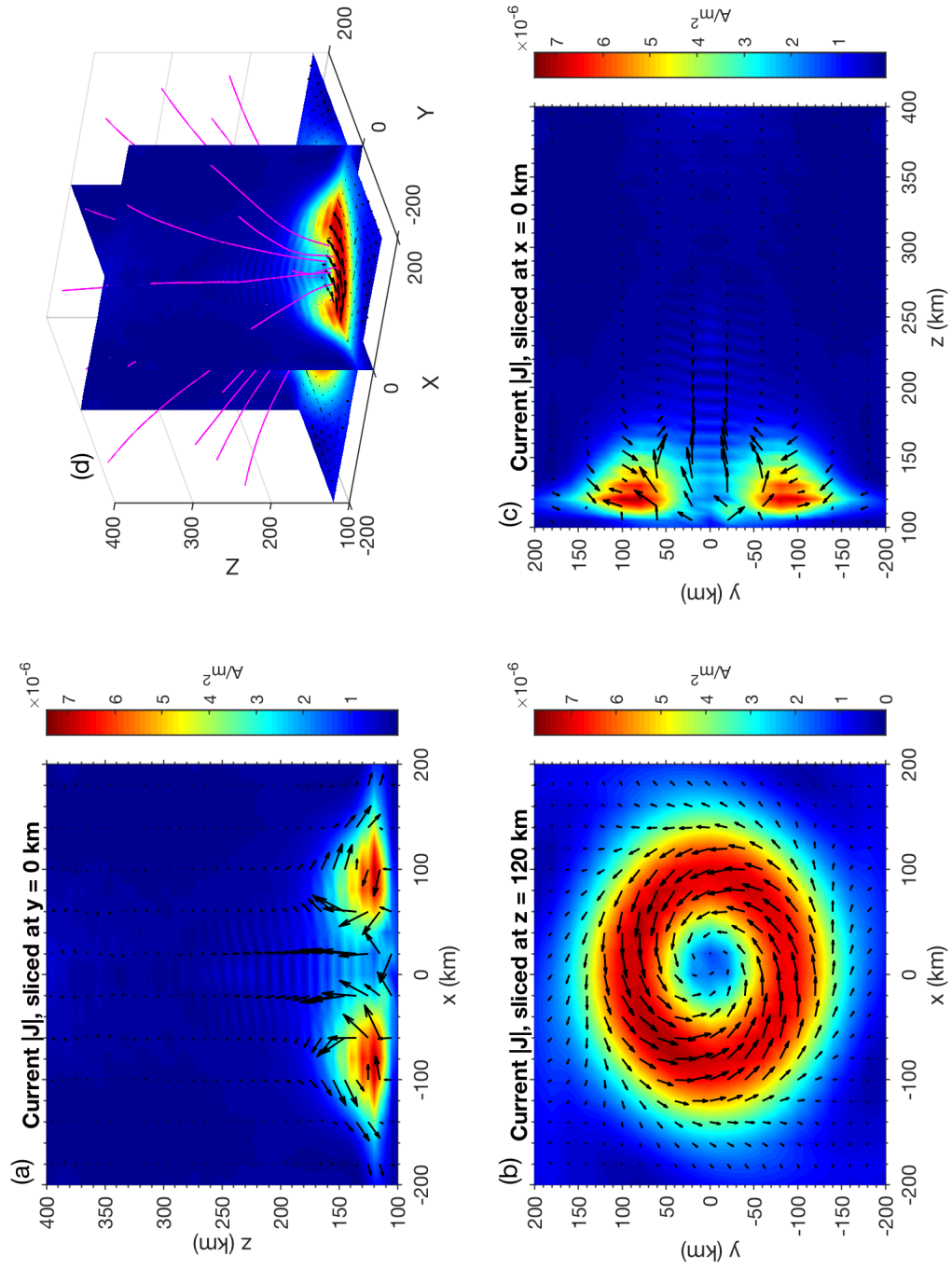

Figure 4.14: Simulation results without chemistry at t=30 s (2τ) showing the magnitude of the current density. Dipole placed at z=-20 km at the center of the xy plane. A neutral wind of 100 m/s in the x direction is applied. Black arrows denote direction of the current. Panel (d) shows a three-dimensional view of slices at x=0 km, y=0 km, and z=120 km. Magenta lines in panel (a) are traced magnetic field lines. Current strengths reach as high as 8 μA/m^2, which are shown in red. Significant currents are absent from most of the domain, and are illustrated in blue.

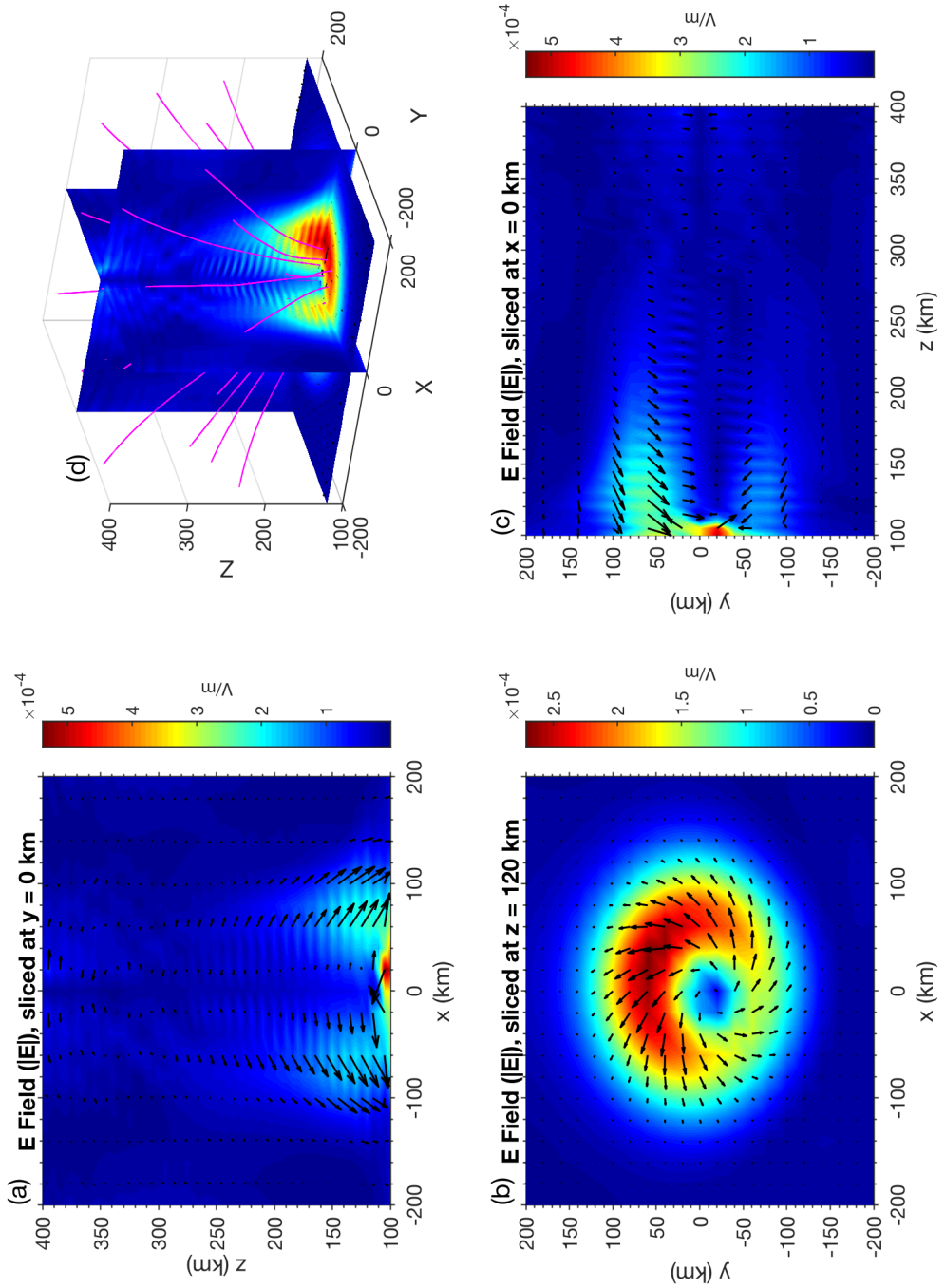

Figure 4.15: Simulation results without chemistry at t=30 s (2τ) showing the magnitude of the electric field. A neutral wind of 100 m/s in the x direction is applied, consistent with Mars GCM models [e.g., *Forget et al.*, 1999]. Black arrows denote direction of the electric field. Panel (a) shows a slice of the xz plane at y=0 km. Panel (b) shows a slice of the xy plane at z=120 km. Panel (c) shows a slice of the yz plane at x=0 km. Red shading indicates strong electric field values of approximately 500 μV/m. Areas of the domain lacking noticeable electric fields are colored in blue.

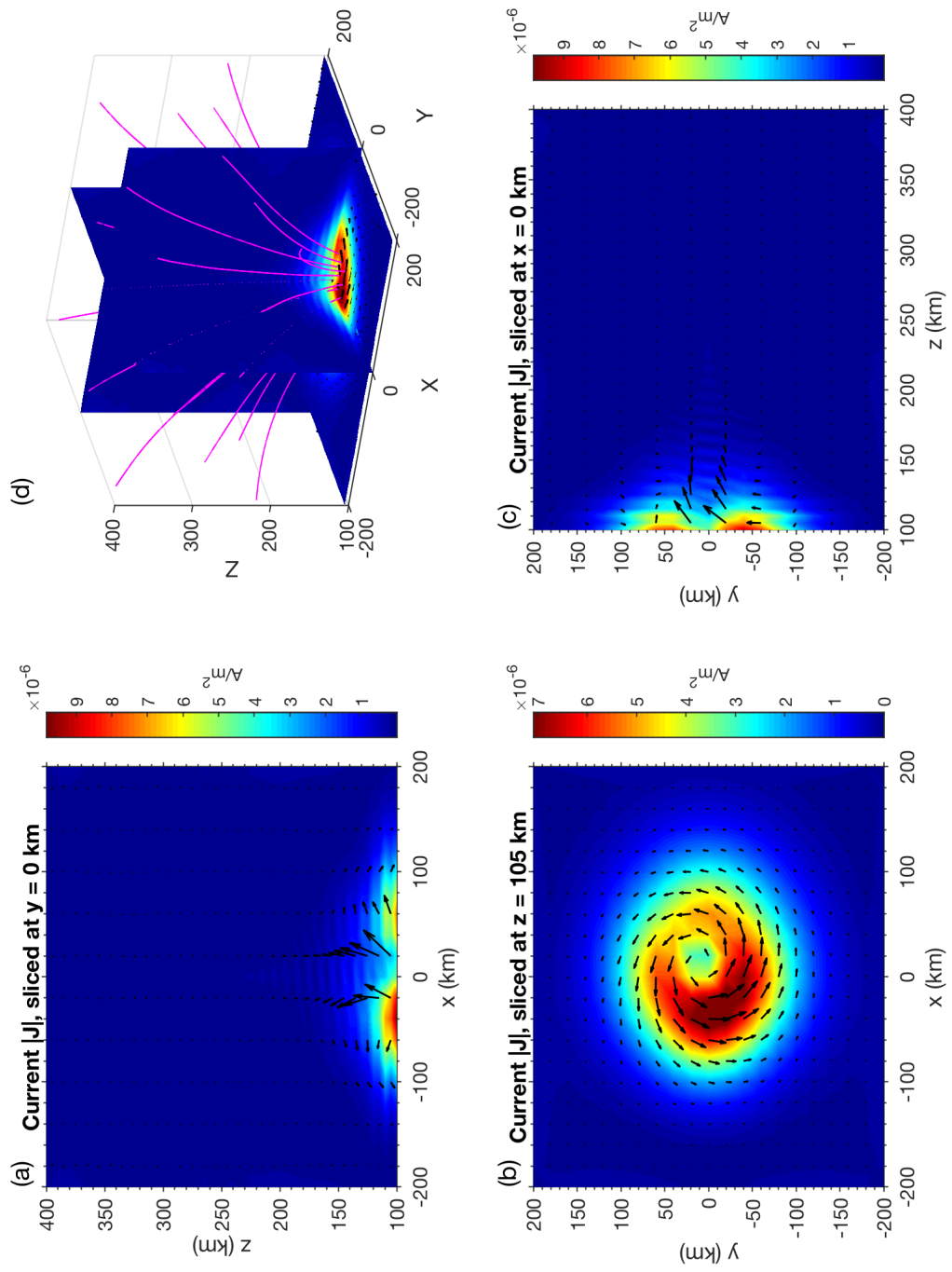

Figure 4.16: Simulation results with chemistry showing the magnitude of the current density at t=30 s (2τ). A neutral wind of 100 m/s in the x direction is applied, consistent with Mars GCM models [e.g., *Forget et al.*, 1999]. Panel (d) shows a three-dimensional view of slices at x=0 km, y=0 km, and z=105 km. Panels (a)−(c) are slices along the x, z, and y direction, respectfully. Current strengths reach as high as 7 μA/m^2 and are colored red. Currents are absent from much of the domain, and are shaded in blue.

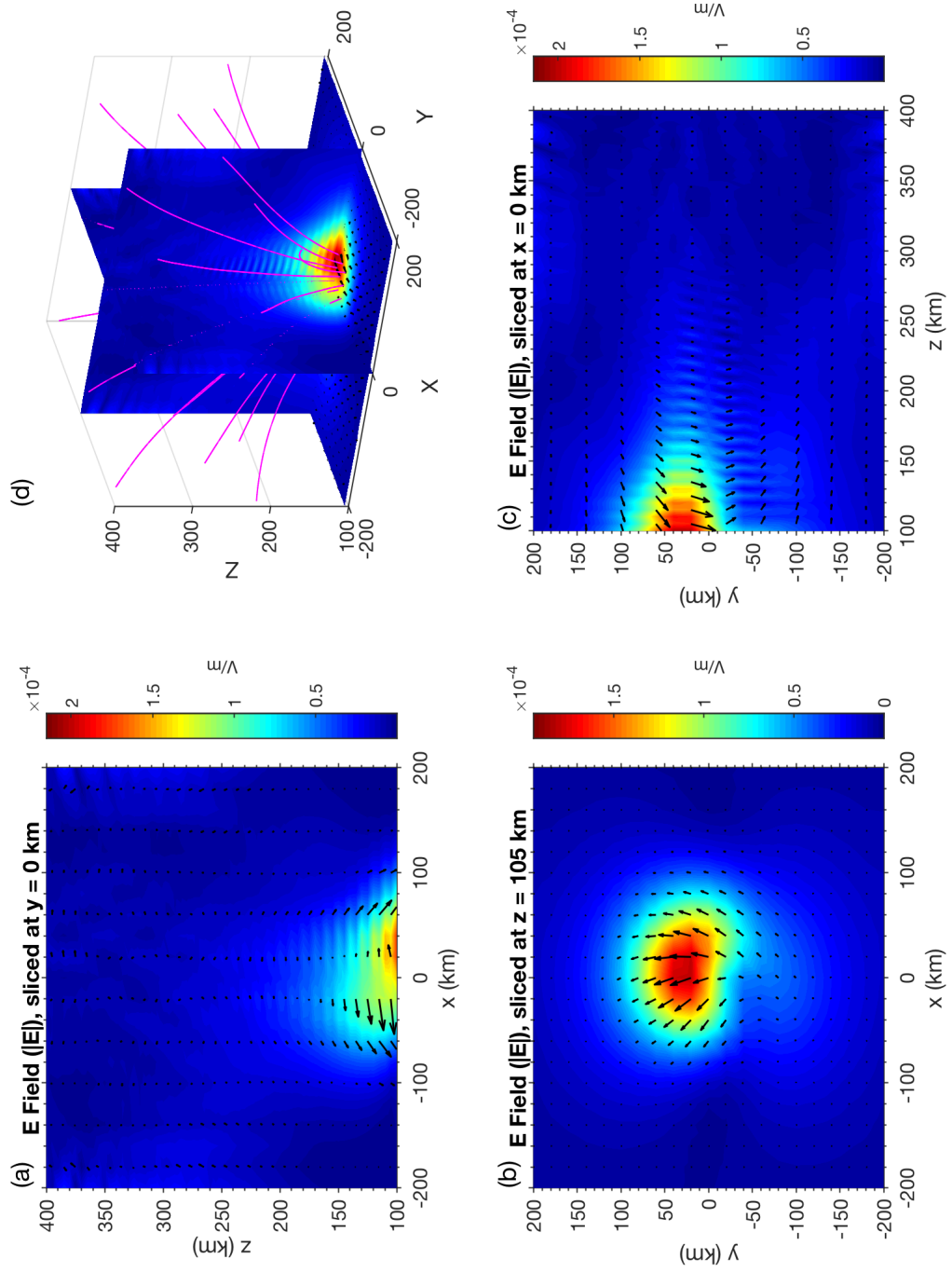

Figure 4.17: Simulation results with chemistry at t=30 s (2τ) showing the magnitude of the electric field. A neutral wind of 100 m/s in the x direction is applied, consistent with Mars GCM models [e.g., *Forget et al.*, 1999]. Black arrows denote direction of the electric field. Panel (a) shows a slice of the xz plane at y=0 km. Panel (b) shows a slice of the xy plane at z=105 km. Panel (c) shows a slice of the yz plane at x=0 km. Red regions indicates strong electric field values up to 220 μV/m. Parts of the domain lacking noticeable electric fields are shown in blue.

Chapter 5

Conclusions and Discussion

Here, we summarize the principal work and contributions following the studies presented in this thesis.

5.1 Results

The chemistry scheme causes noticeable differences in ion and electron profiles. Concentrations of O^+ are similar to the previously used profile except below 250 km altitudes, where there is another region of O^+ observed extending into the dynamo region. The peak density of O^+ is raised by about 30 km. Populations of O_2^+ are an order of magnitude larger below 250 km with the chemistry scheme, with a peak region observed about 30 km lower. Likely, the most influential impact of the chemistry scheme is on CO_2^+. As seen in Figure 4.2b, there is no longer a peak density of CO_2^+ between 100 and 200 km. As a result, there is no longer a peak electron density.

When considering chemistry in the presence of a uniform magnetic field accompanied by a uniform neutral wind in the positive x direction, a dynamo current is observed between 150 and 200 km, shifted upwards by 10 km compared to when chemistry is not considered. With our current δz=5 km, this only accounts to two grid points. The strength of these currents are on the order of 10 nA/m^2, which agree well with the findings of *Withers* [2008]. This current is formed through perturbations of the magnetic field through Ampere's law (2.7). This effect on the field as defined

in Faraday's law (2.8) is caused by electric fields. The motions of ions in the positive x direction help to "pull" the magnetic field leading to currents building up over time in the x plane, as seen in the generalized Ohm's law (2.19). Further "twisting" of the field in the y direction is caused due to the $\vec{J} \times \vec{B}$ Hall term.

When placing a dipole below the center of the simulation grid, we observe a current buildup around the base of the cusp. Compared to when chemistry is not utilized, the current appears to be forming at a much lower altitude around 105 km. Furthermore, it is much more concentrated around the center of the cusp, having an outer envelope radius approximately 50 km smaller than when the scheme is not employed. The current also possesses more asymmetry compared to the previous model. The strength of the dynamo current is slightly smaller, but still on the same order of magnitude as when chemistry is neglected. The electrons are only partially magnetized, and are moving much more slowly than in previous scenarios while the ions are still demagnetized as expected. The electric field no longer has the same symmetry as before, and is mostly concentrated on the east side of the cusp. The magnitude of the electric field is only slightly weakened compared to before. Electron pressure profiles for chemistry and non chemistry simulation runs show a stark difference in electron pressure below 150 km. There is no inflection point in the electron pressure at 125 km, and it is up to an order of magnitude larger than in the non chemistry simulation.

The answers to most of our questions likely stem from differences in the electron density profiles. In the case of the uniform magnetic field, we expect the current to form somewhere between 150 and 200 km when not considering chemistry. When chemistry is included, the ion profile shows differences in ion concentrations, but the electron distributions are similar except at the region below 150 km. This is likely why in the uniform magnetic field case, we see the dynamo current shifting by only 10 km compared to before. However, In the cusp case without chemistry the dynamo region is lower, between 100 and 150 km, which corresponds to where the peak electron density region exists when chemistry is not considered. With chemistry, there is no peak electron density in this region, and the current is "pushed" down to lower altitudes. We should expect a Chapman profile and hence a cut-off, why it doesn't appear is an unresolved question perhaps indicative of a missing loss process

for CO_2^+. Another possible conclusion is the need for more updated neutral and ion profiles.

5.2 Broader impact

Investigating the formation of dynamo currents and the corresponding magnetic perturbations are very important for clarifying our understanding of the magnetic topology of Mars, especially at lower altitudes. Perturbations greater than the IMF values at the surface in the unshielded regions of the northern hemisphere (several nT) are particularly significant and will require revisiting the current maps of the crustal fields obtained by MGS. Alternately, a negative conclusion will simply mean validation of the current maps, which remains a positive and useful outcome. Furthermore, identifying significant currents also implies trapped particles in the Martian atmosphere, which would be important for studying mechanisms of atmospheric loss over the history of the planet.

5.3 Future work

Further investigation of the chemistry model used is required. In this study, peak regions for O^+ and O_2^+ are similar to those found by *Najib et al.* [2011], who employed a similar set of chemical reactions in a Mars global multifluid MHD model. The culprit for the high electron density is attributed to the high production of CO_2^+ in sub 150 km regions. There should be a region where the ionization processes for CO_2^+ balance with recombination processes. It is expected that this region should lie between 100 and 150 km. Future work will include developing Chapman profiles to help predict where the peak electron density region exists.

Boundary conditions could be causing mirroring in the electric field, leading to some non-physical effects. This could be especially important now that the dynamo current is forming close to the lower boundary. Therefore, further investigation of the boundary condition effects is needed. The erratic behavior in density and pressure profiles at high altitudes could be attributed to numerical effects or to waves. The

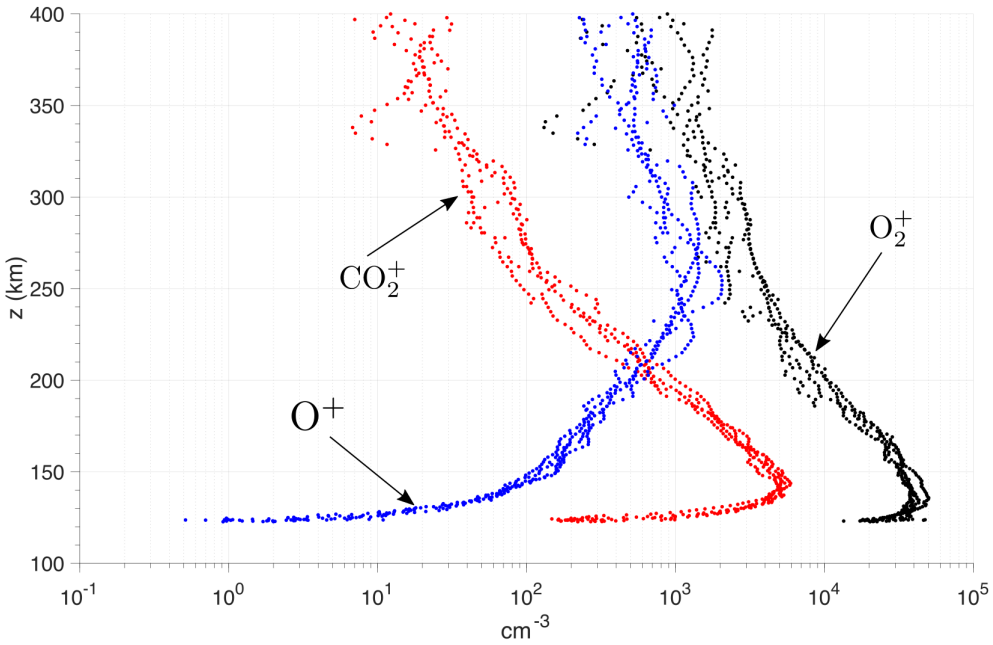

Figure 5.1: MAVEN ion density measurements from the NGIMS instrument. Data is provided from four consecutive deep dips on the dayside. Units are in particles per cubic centimeter [Lillis, 2018, private communication].

$\vec{J}\times\vec{B}$ Hall term in the generalized Ohm's law (2.19) introduces the whistler wave mode into the system, and the calculation of time steps according to the CFL condition must be adapted accordingly.

Future plans include adapting our profiles to correspond to observations by the MAVEN mission in order to provide self-consistent input to the model. Currently, dayside ion densities are available above 100 km, as seen in Figure 5.1. Neutral dayside densities are also available, but only up to 300 km as seen in Figure 5.2. Ion and electron temperatures are also available through the LPW instrument, although not shown here. Ion and neutral wind data will be available August 15, 2018 [*Lillis*, 2018, private communication]. Altogether, this will allow us to create the necessary initial density, pressure, and velocity profiles for all the modeled species.

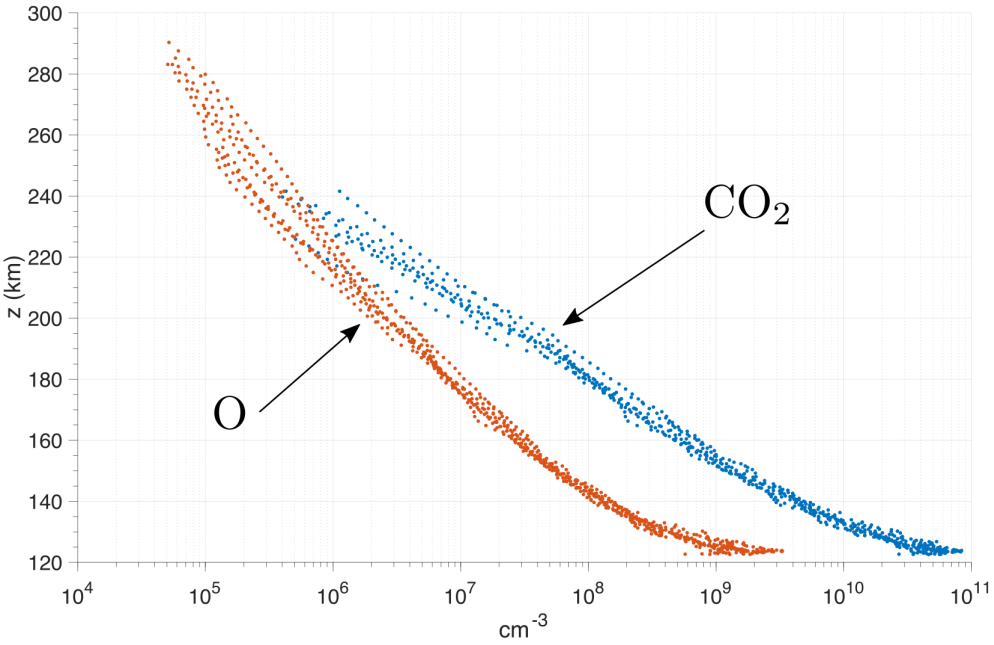

Figure 5.2: MAVEN dayside ion density measurements from the NGIMS instrument. Data is provided from four consecutive deep dips on the dayside. Units are in particles per cubic centimeter [Lillis, 2018, private communication].

Appendix A

Derivation of the Normalized MF-MHD Equations

A.1 Probability function and the Boltzmann equation

For each species α in the six-dimensional phase space $(\vec{r}, \vec{v})$ a distribution function $f_\alpha(\vec{r}, \vec{v}, t)$ is introduced.

$f_\alpha(\vec{r}, \vec{v}, t) d^3\vec{r} d^3\vec{v}$	=	number of particles inside a six-dimensional phase space volume at ($\vec{r}$,$\vec{v}$) at time t	*Lieberman and Lichtenberg* [2005]
$\frac{f_\alpha(\vec{r},\vec{v},t) d^3\vec{r} d^3\vec{v}}{n_\alpha}$	=	probability that a particle has a position in $d^3\vec{r}$ around $\vec{r}$ and a velocity in $d^3\vec{v}$ around $\vec{v}$	*Baierlein* [1999]

The values $\vec{r}$ and $\vec{v}$ are considered to be independent variables. As particles drift or move under the influence of macroscopic forces, they flow into and out of a fixed volume $dxdv_x$, $dydv_y$, or $dzdv_z$. Therefore, the distribution function should obey a continuity equation, which can be written as

$$\frac{\partial f_\alpha}{\partial t} + v_x \frac{\partial f_\alpha}{\partial x} + a_x \frac{\partial f_\alpha}{\partial v_x} = 0 \tag{A.1}$$

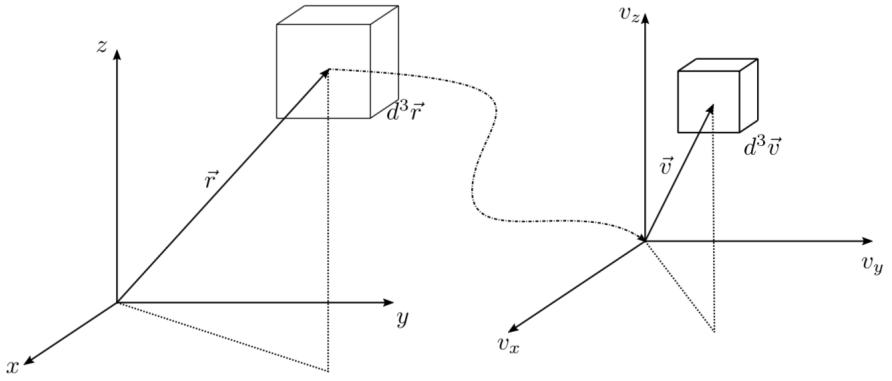

Figure A.1: Illustration of $\frac{f_\alpha(\vec{r},\vec{v},t)d^3\vec{r}d^3\vec{v}}{n_\alpha}$, which is the probability that a particle has a position in $d^3\vec{r}$ space and a velocity in $d^3\vec{v}$ space

It is important to note that v_x is independent of x, and it is assumed that $a_x = \frac{F_x}{m_\alpha}$ of a particle does not depend on v_x. In three dimensions, it is written as

$$\frac{\partial f_\alpha(\vec{r},\vec{v},t)}{\partial t} + \vec{v}\cdot\nabla_{\vec{r}} f_\alpha(\vec{r},\vec{v},t) + \vec{a}\cdot\nabla_{\vec{v}} f_\alpha(\vec{r},\vec{v},t) = \left(\frac{\partial f_\alpha}{\partial t}\right)_c \tag{A.2}$$

and is called the Boltzmann equation. In addition to flows in and out of the volume, sources and sinks of particles exist in the volume because of interparticle collisions and reactions on timescales very small compared to the evolution of f_α in (A.2). Such events can instantly change velocity (but not position) of a particle [e.g., *Lieberman and Lichtenberg*, 2005, p. 28]. To account for this, a collision term $\left(\frac{\partial f_\alpha}{\partial t}\right)_c$ is added.

Collision operator

The collision term $\left(\frac{\partial f_\alpha}{\partial t}\right)_c$ in equation (A.2) is called the Krook collision operator and also referred to as the BGK model [e.g., *Bhatnagar et al.*, 1954]. From *Shu* [1992], this term can be written as:

$$\left(\frac{\partial f_\alpha}{\partial t}\right)_c = \sum_n \nu^{\mathrm{S}}_{n\to\alpha} f_n(\vec{v}) - \nu^{\mathrm{L}}_\alpha f_\alpha(\vec{v}) - \sum_\beta \nu_{\alpha,\beta}(f_\alpha(\vec{v}) - f_{\mathrm{m},\alpha}(\vec{v},\vec{u}_\beta) \tag{A.3}$$

where $f_{\mathrm{m},\alpha}(\vec{v},\vec{u}_\beta)$ is the shifted maxwellian distribution given as

$$f_{\mathrm{m},\alpha}(\vec{v},\vec{u}_\beta) = n_\alpha \left(\frac{m_\alpha}{2\pi k_\mathrm{B} T_\alpha}\right)^{3/2} c^{-\frac{m_\alpha(\vec{v}-\vec{u}_\beta)^2}{2k_\mathrm{B}T_\alpha}} \tag{A.4}$$

By integrating the maxwellian distribution one can obtain densities, velocities, energies etc.

A.2 Moments of the Boltzmann Equation

By integrating the distribution function one can obtain density, fluid velocity, energy, etc. In general:

$$\langle \chi_\alpha(\vec{v})\rangle_\alpha = \frac{\int \chi_\alpha(\vec{v}) f_\alpha(\vec{v}) d^3\vec{v}}{\int f_\alpha(\vec{v}) d^3\vec{v}} \tag{A.5}$$

A general expression for the moments of the Boltzmann equation can now be constructed using (A.5) as $\int \chi_\alpha(\vec{v})[(\mathrm{A.2})]d^3\vec{v}$

$$\underbrace{\int \chi_\alpha(\vec{v})\frac{\partial f_\alpha(\vec{v})}{\partial t} d^3\vec{v}}_{\mathrm{I}} + \underbrace{\int \chi_\alpha(\vec{v})\vec{v}\cdot\nabla_{\vec{r}} f_\alpha(\vec{v}) d^3\vec{v}}_{\mathrm{II}} + \underbrace{\int \chi_\alpha(\vec{v})\vec{a}\cdot\nabla_{\vec{v}} f_\alpha(\vec{v}) d^3\vec{v}}_{\mathrm{III}} = \underbrace{\int \chi_\alpha(\vec{v})\left(\frac{\partial f_\alpha}{\partial t}\right)_c d^3\vec{v}}_{\mathrm{IV}} \tag{A.6}$$

The first term can be simplified

$$\mathbf{I} = \int \chi_\alpha(\vec{v})\frac{\partial f_\alpha(\vec{v})}{\partial t} d^3\vec{v} = \frac{\partial}{\partial t}\left(\int \chi_\alpha(\vec{v}) f_\alpha d^3\vec{v}\right) = \frac{\partial n_\alpha \langle \chi_\alpha(\vec{v})\rangle_\alpha}{\partial t} \tag{A.7}$$

Similarly, the other terms can be written as

$$\mathbf{II} = \int \chi_\alpha(\vec{v})\vec{v}\cdot\nabla_{\vec{r}} f_\alpha(\vec{v}) d^3\vec{v} = \nabla_{\vec{r}}\cdot(n_\alpha\langle\chi_\alpha(\vec{v})\vec{v}\rangle_\alpha) \tag{A.8}$$

$$\mathbf{III} = \int \chi_\alpha(\vec{v})\vec{a}\cdot\nabla_{\vec{v}} f_\alpha(\vec{v}) d^3\vec{v} = -n_\alpha\left\langle (\nabla_{\vec{v}}\chi_\alpha(\vec{v}))\cdot\frac{\vec{F}(\vec{v})}{m_\alpha}\right\rangle_\alpha \tag{A.9}$$

$$\begin{aligned}\mathbf{IV} = \int \chi_\alpha(\vec{v}) \left(\frac{\partial f_\alpha}{\partial t}\right)_c d^3\vec{v} = \sum_n \nu^{\mathrm{S}}_{n\to\alpha} n_n \langle\chi_\alpha(\vec{v})\rangle_n - \nu^{\mathrm{L}}_\alpha n_\alpha \langle\chi_\alpha(\vec{v})\rangle_\alpha \\ - \sum_\beta \nu_{\alpha,\beta}\left(n_\alpha\langle\chi_\alpha(\vec{v})\rangle_\alpha - \int \chi_\alpha(\vec{v}) f_{\mathrm{m},\alpha}(\vec{v},\vec{u}_\beta) d^3\vec{v}\right)\end{aligned} \tag{A.10}$$

Therefore the moments of the Boltzmann equation for any species α can be written as

$$\begin{aligned}&\frac{\partial n_\alpha\langle\chi_\alpha(\vec{v})\rangle_\alpha}{\partial t} + \nabla_{\vec{r}}\cdot\left(n_\alpha\langle\chi_\alpha(\vec{v})\vec{v}\rangle_\alpha\right) - n_\alpha\left\langle\left(\nabla_{\vec{v}}\chi_\alpha(\vec{v})\right)\cdot\frac{\vec{F}(\vec{v})}{m_\alpha}\right\rangle_\alpha = \\ &\sum_n \nu^{\mathrm{S}}_{n\to\alpha} n_n\langle\chi_\alpha(\vec{v})\rangle_n - \nu^{\mathrm{L}}_\alpha n_\alpha\langle\chi_\alpha(\vec{v})\rangle_\alpha - \sum_\beta \nu_{\alpha,\beta}\left(n_\alpha\langle\chi_\alpha(\vec{v})\rangle_\alpha - \int\chi_\alpha(\vec{v}) f_{\mathrm{m},\alpha}(\vec{v},\vec{u}_\beta)d^3\vec{v}\right)\end{aligned} \tag{A.11}$$

Where $\vec{a} = \frac{\vec{F}(\vec{v})}{m_\alpha}$, and the force vector is defined as

$$\vec{F}(\vec{v}) = q_\alpha\big(\vec{E} + \vec{v}\times\vec{B}\big) + \frac{m_\alpha \vec{g}_{\mathrm{M}}}{\left(1+\frac{z}{R_{\mathrm{M}}}\right)^2} \tag{A.12}$$

A.2.1 Conservation of mass

Allow $\chi_\alpha(\vec{v})$=1 and find the terms

$$\mathbf{I} = \frac{\partial n_\alpha\langle 1\rangle_\alpha}{\partial t} = \frac{\partial n_\alpha}{\partial t}$$

$$\mathbf{II} = \nabla_{\vec{r}}\cdot\left(n_\alpha\langle\vec{v}\rangle_\alpha\right) = \nabla_{\vec{r}}\cdot\left(n_\alpha\vec{u}_\alpha\right)$$

$$\mathbf{III} = -n_\alpha\left\langle\cancelto{0}{\nabla_{\vec{v}}(1)}\cdot\frac{\vec{F}(\vec{v})}{m_\alpha}\right\rangle_\alpha = 0$$

$$\mathbf{IV} = \sum_n \nu^{\mathrm{S}}_{n\to\alpha} n_n\langle 1\rangle_n - \nu^{\mathrm{L}}_\alpha n_\alpha\langle 1\rangle_\alpha - \sum_\beta \nu_{\alpha,\beta}\cancelto{0}{\left(n_\alpha\langle 1\rangle_\alpha - \underbrace{\int (1) f_{\mathrm{m},\alpha}(\vec{v},\vec{u}_\beta)d^3\vec{v}}_{n_\alpha}\right)}$$

$$= S_\alpha - L_\alpha$$

Where the sources and losses due to chemistry are defined as

$$S_\alpha = \sum_n \nu^{\mathrm{S}}_{n\to\alpha} n_n \tag{A.13}$$

$$L_\alpha = \nu^{\mathrm{L}}_\alpha n_\alpha \tag{A.14}$$

Finally mass continuity can be written by substituting **I**–**IV** into the Boltzmann equation (A.6)

$$\frac{\partial n_\alpha}{\partial t} + \nabla_{\vec{r}} \cdot (n_\alpha \vec{u}_\alpha) = S_\alpha - L_\alpha \tag{A.15}$$

A.2.2 Conservation of momentum

Allow $\chi_\alpha(\vec{v}) = m_\alpha \vec{v}$ and form **I**–**IV** again. The first one is straightforward:

$$\mathbf{I} = \frac{\partial n_\alpha \langle m_\alpha \vec{v} \rangle_\alpha}{\partial t} = \frac{\partial n_\alpha m_\alpha \vec{u}_\alpha}{\partial t}$$

The second moment:

$$\mathbf{II} = \nabla_{\vec{r}} \cdot (n_\alpha \langle m_\alpha \vec{v}\vec{v} \rangle_\alpha) = \vec{u}_\alpha \vec{u}_\alpha + \langle \vec{w}\vec{w} \rangle_\alpha$$

where $\langle \vec{v}\vec{v} \rangle_\alpha = \langle (\vec{u}_\alpha + \vec{w})(\vec{u}_\alpha + \vec{w}) \rangle_\alpha$ and the particle velocity $\vec{v}$ is the sum of the macroscopic fluid velocity $\vec{u}_\alpha$ and the peculiar velocity $\vec{w}$, as defined by [Harris, 2004]. The diffusion term can be expressed as

$$\mathbf{II} = \nabla_{\vec{r}} \cdot \left(n_\alpha m_\alpha \vec{u}_\alpha \vec{u}_\alpha + \underbrace{m_\alpha n_\alpha \langle \vec{w}\vec{w} \rangle_\alpha}_{\bar{\bar{\Pi}}_\alpha} \right) = \nabla_{\vec{r}} \cdot (n_\alpha m_\alpha \vec{u}_\alpha \vec{u}_\alpha) + \nabla_{\vec{r}} \cdot \bar{\bar{\Pi}}_\alpha$$

where $\bar{\bar{\Pi}}_\alpha$ is the stress tensor. The term **III** is given by:

$$\mathbf{III} = -n_\alpha \langle \nabla_{\vec{v}} (m_\alpha \vec{v}) \cdot \frac{\vec{F}(\vec{v})}{m_\alpha} \rangle_\alpha = -n_\alpha \langle \vec{F}(\vec{v}) \rangle_\alpha$$

Substitute in (A.12) for the force term,

$$\mathbf{III} = -n_\alpha q_\alpha\big(\vec{E} + \langle\vec{v}\rangle_\alpha \times \vec{B}\big) - \frac{m_\alpha \vec{g}_{\mathrm{M}}}{\Big(1+\frac{z}{R_{\mathrm{M}}}\Big)^2} = -n_\alpha q_\alpha\big(\vec{E} + \vec{u}_\alpha \times \vec{B}\big) - \frac{m_\alpha n_\alpha \vec{g}_{\mathrm{M}}}{\Big(1+\frac{z}{R_{\mathrm{M}}}\Big)^2}$$

Last, the collision term can be written as

$$\begin{aligned}
\mathbf{IV} &= \sum_n \nu^{\mathrm{S}}_{n\to\alpha} n_n \langle m_\alpha \vec{v}\rangle_n - \nu^{\mathrm{L}}_\alpha n_\alpha \langle m_\alpha \vec{v}\rangle_\alpha - \sum_\beta \nu_{\alpha,\beta}\Big(n_\alpha \langle m_\alpha \vec{v}\rangle_\alpha - \int m_\alpha \vec{v} f_{\mathrm{m},\alpha}(\vec{v},\vec{u}_\beta) d^3\vec{v}\Big) \\
&= m_\alpha \underbrace{\sum_n \nu^{\mathrm{S}}_{n\to\alpha} n_n}_{S_\alpha} \langle\vec{v}\rangle_n - m_\alpha \underbrace{\nu^{\mathrm{L}}_\alpha n_\alpha}_{L_\alpha} \langle\vec{v}\rangle_\alpha - m_\alpha \sum_\beta \nu_{\alpha,\beta}\Big(n_\alpha\langle\vec{v}\rangle_\alpha - \underbrace{\int \vec{v} f_{\mathrm{m},\alpha}(\vec{v},\vec{u}_\beta) d^3\vec{v}}_{n_\alpha \vec{u}_\beta}\Big) \\
&= m_\alpha S_\alpha \vec{u}_n - m_\alpha L_\alpha \vec{u}_\alpha - \sum_\beta \nu_{\alpha,\beta} m_\alpha n_\alpha (\vec{u}_\alpha - \vec{u}_\beta)
\end{aligned}$$

Now, Equation (A.6) can be used to obtain the first moment of the Boltzmann equation:

$$\begin{aligned}
\frac{\partial n_\alpha m_\alpha \vec{u}_\alpha}{\partial t} + \nabla_{\vec{r}}\cdot(n_\alpha m_\alpha \vec{u}_\alpha \vec{u}_\alpha) &= n_\alpha q_\alpha\big(\vec{E} + \vec{u}_\alpha \times \vec{B}\big) - \nabla_{\vec{r}}\cdot\bar{\bar{\Pi}}_\alpha + ... \\
&\frac{m_\alpha n_\alpha \vec{g}_{\mathrm{M}}}{\Big(1+\frac{z}{R_{\mathrm{M}}}\Big)^2} + m_\alpha S_\alpha \vec{u}_n - m_\alpha L_\alpha \vec{u}_\alpha - \sum_\beta \nu_{\alpha,\beta} m_\alpha n_\alpha (\vec{u}_\alpha - \vec{u}_\beta)
\end{aligned} \tag{A.16}$$

This can be simplified Furthermore by expanding the left side:

$$\begin{aligned}
&\frac{\partial m_\alpha n_\alpha \vec{u}_\alpha}{\partial t} + \underbrace{\nabla_{\vec{r}}\cdot(m_\alpha n_\alpha \vec{u}_\alpha \vec{u}_\alpha)}_{\text{Expand}} = \underbrace{\frac{\partial}{\partial t}(m_\alpha n_\alpha \vec{u}_\alpha)}_{\text{Expand}} + \nabla_{\vec{r}}\cdot(m_\alpha n_\alpha \vec{u}_\alpha)\vec{u}_\alpha + (m_\alpha n_\alpha \vec{u}_\alpha\cdot\nabla_{\vec{r}})\vec{u}_\alpha \\
&= m_\alpha n_\alpha \frac{\partial}{\partial t}(\vec{u}_\alpha) + \underbrace{m_\alpha \vec{u}_\alpha \frac{\partial}{\partial t}(n_\alpha) + m_\alpha \vec{u}_\alpha\big(\nabla_{\vec{r}}\cdot(n_\alpha\vec{u}_\alpha)\big)}_{\text{Combine}} + (m_\alpha n_\alpha \vec{u}_\alpha\cdot\nabla_{\vec{r}})\vec{u}_\alpha \\
&= m_\alpha n_\alpha \frac{\partial}{\partial t}(\vec{u}_\alpha) + m_\alpha \vec{u}_\alpha\Bigg(\underbrace{\frac{\partial n_\alpha}{\partial t} + \nabla_{\vec{r}}\cdot(n_\alpha\vec{u}_\alpha)}_{\text{(A.15)}}\Bigg) + (m_\alpha n_\alpha \vec{u}_\alpha\cdot\nabla_{\vec{r}})\vec{u}_\alpha \\
&= m_\alpha n_\alpha\Big(\frac{\partial \vec{u}_\alpha}{\partial t} + \vec{u}_\alpha\cdot\nabla_{\vec{r}}\vec{u}_\alpha\Big) + m_\alpha \vec{u}_\alpha(S_\alpha - L_\alpha)
\end{aligned}$$

This addition of a loss term which is coupled with the species' fluid velocity effectively eliminates losses in (A.16). Note, however, that the source term is now coupled to

both $\vec{u}_n$ and $\vec{u}_\alpha$. Now, conservation of momentum can be written as

$$\frac{\partial \vec{u}_\alpha}{\partial t}+\vec{u}_\alpha\cdot\nabla_{\vec{r}}\vec{u}_\alpha=\frac{q_\alpha}{m_\alpha}\big(\vec{E}+\vec{u}_\alpha\times\vec{B}\big)-\frac{\nabla_{\vec{r}}\cdot\bar{\bar{\Pi}}_\alpha}{m_\alpha n_\alpha}+\frac{\vec{g}_{\rm M}}{\Big(1+\frac{z}{R_{\rm M}}\Big)^2}+\frac{S_\alpha}{n_\alpha}(\vec{u}_n-\vec{u}_\alpha)-\sum_\beta\nu_{\alpha,\beta}(\vec{u}_\alpha-\vec{u}_\beta) \quad \text{(A.17)}$$

A.2.3 Conservation of energy

Now we can tackle the final equation of energy conservation. Allow $\chi_\alpha(\vec{v})=m_\alpha\frac{\vec{v}^2}{2}$ and find the moments of (A.6),

$$\mathbf{I}=\frac{\partial n_\alpha\langle m_\alpha\frac{\vec{v}^2}{2}\rangle_\alpha}{\partial t}=\frac{\partial W_\alpha}{\partial t}$$

Recall that

$$\underbrace{\vec{v}}_{\text{fluid velocity}}=\underbrace{\vec{u}_\alpha}_{\text{fluid velocity}}+\underbrace{\vec{w}}_{\text{peculiar velocity}} \quad \text{(A.18)}$$

By integrating the fluid velocity (A.18) over the distribution function, the group velocity is obtained, and the random motions are averaged out:

$$\langle\vec{v}\rangle_\alpha=\vec{u}_\alpha\rightarrow\langle\vec{w}\rangle_\alpha=\vec{0} \quad \text{(A.19)}$$

Therefore, specific energy of either charged species or neutral species $W_{\alpha/n}$ can be written as

$$W_{\alpha/n}=\langle\frac{1}{2}m_{\alpha/n}n_{\alpha/n}\underbrace{\vec{v}^2}_{\text{(A.18)}}\rangle_{\alpha/n}=\frac{1}{2}m_{\alpha/n}n_{\alpha/n}\vec{u}^2_{\alpha/n}+m_{\alpha/n}n_{\alpha/n}\mathcal{E}_{\alpha/n} \quad \text{(A.20)}$$

where $\mathcal{E}_\alpha$ is the specific internal energy from [Shu, 1992]

$$\mathcal{E}_{\alpha/n}=\frac{\langle\vec{w}^2\rangle_{\alpha/n}}{2} \quad \text{(A.21)}$$

Knowing this, we can rewrite **I** in terms of pressure instead of energy

$$\begin{aligned}\mathbf{I} &= \frac{\partial W_\alpha}{\partial t} = \frac{\partial}{\partial t}\left(m_\alpha n_\alpha \mathcal{E}_\alpha + \frac{m_\alpha n_\alpha \vec{u}_\alpha^2}{2}\right) = \frac{\partial}{\partial t}(m_\alpha n_\alpha \mathcal{E}_\alpha) + \frac{\partial}{\partial t}\left(\frac{m_\alpha n_\alpha \vec{u}_\alpha^2}{2}\right) \\ &= \frac{\partial}{\partial t}(m_\alpha n_\alpha \mathcal{E}_\alpha) + m_\alpha \frac{\vec{u}_\alpha^2}{2}\underbrace{\frac{\partial n_\alpha}{\partial t}}_{\text{(A.15)}} + m_\alpha n_\alpha \vec{u}_\alpha \underbrace{\frac{\partial \vec{u}_\alpha}{\partial t}}_{\text{(A.17)}}\end{aligned}$$

After substituting in (A.15) and (A.17), the first term can be simplified to

$$\mathbf{I} = \frac{\partial}{\partial t}(m_\alpha n_\alpha \mathcal{E}_\alpha) - \nabla_{\vec{r}} \cdot \left(m_\alpha n_\alpha \frac{\vec{u}_\alpha}{2}\vec{u}_\alpha\right) + \vec{J}_\alpha \cdot \vec{E} - \vec{u}_\alpha \cdot \left(\nabla_{\vec{r}} \cdot \bar{\bar{\Pi}}_\alpha\right) + \frac{m_\alpha n_\alpha \vec{u}_\alpha \cdot \vec{g}_{\mathrm{M}}}{\left(1 + \frac{z}{R_{\mathrm{M}}}\right)^2} + \ldots$$

$$\sum_n \nu^{\mathrm{S}}_{n\to\alpha} m_\alpha n_n \big(\vec{u}_\alpha \cdot \vec{u}_n - \frac{\vec{u}_\alpha^2}{2}\big) - \nu^{\mathrm{L}}_\alpha n_\alpha m_\alpha \frac{\vec{u}_\alpha^2}{2} - \sum_\beta \nu_{\alpha,\beta} m_\alpha n_\alpha (\vec{u}_\alpha^2 - \vec{u}_\alpha \cdot \vec{u}_\beta)$$

Using a similar approach, (A.8) can be rewritten:

$$\mathbf{II} = \nabla_{\vec{r}} \cdot \left(n_\alpha \langle m_\alpha \frac{\vec{v}^2}{2}\vec{v}\rangle_\alpha\right)$$

at this point, we introduce the flux of thermal energy, which is written as

$$\vec{Q}_\alpha = \langle m_\alpha \frac{\vec{w}^2}{2}\vec{w}\rangle_\alpha \tag{A.22}$$

Decomposing $\langle \vec{v}^2\vec{v}\rangle_\alpha$ using (A.18) and utilizing (A.22) yields:

$$\begin{aligned}\mathbf{II} &= \nabla_{\vec{r}} \cdot \left(n_\alpha m_\alpha \langle \frac{1}{2}(\vec{u}_\alpha + \vec{w})^2(\vec{u}_\alpha + \vec{w})\rangle_\alpha\right) = \nabla_{\vec{r}} \cdot \left(n_\alpha m_\alpha \frac{1}{2}(\vec{u}_\alpha^2\vec{u} + 2\langle \vec{w}\vec{w}\rangle_\alpha \vec{u}_\alpha + \langle \vec{w}^2\rangle_\alpha \vec{u}_\alpha + \langle \vec{w}^3\rangle_\alpha)\right) \\ &= \nabla_{\vec{r}} \cdot \left(n_\alpha m_\alpha \frac{\vec{u}_\alpha^2\vec{u}_\alpha}{2} + \underbrace{n_\alpha m_\alpha \langle \vec{w}\vec{w}\rangle_\alpha}_{\bar{\bar{\Pi}}_\alpha}\vec{u}_\alpha + n_\alpha m_\alpha \underbrace{\frac{\langle \vec{w}^2\rangle_\alpha}{2}}_{\text{(A.21)}}\vec{u}_\alpha + \underbrace{n_\alpha m_\alpha \frac{\langle \vec{w}^3\rangle_\alpha}{2}}_{\text{(A.22)}}\right) \\ &= \nabla_{\vec{r}} \cdot \left(m_\alpha \frac{\vec{u}_\alpha^2\vec{u}_\alpha}{2}\right) + \nabla_{\vec{r}} \cdot \left(\bar{\bar{\Pi}}_\alpha \vec{u}_\alpha\right) + \nabla_{\vec{r}} \cdot \left(n_\alpha m_\alpha \mathcal{E}_\alpha \vec{u}_\alpha\right) + \nabla_{\vec{r}} \cdot \vec{Q}_\alpha\end{aligned}$$

Now the third moment can be worked on,

$$\begin{aligned}
\mathbf{III} &= -n_\alpha \Big\langle \nabla_{\vec{v}} \Big(m_\alpha \frac{\vec{v}^2}{2} \Big) \cdot \frac{\vec{F}(\vec{v})}{m_\alpha} \Big\rangle_\alpha = -n_\alpha \Big\langle \vec{v} \cdot \vec{F}(\vec{v}) \Big\rangle_\alpha = -n_\alpha \Big\langle \vec{v} \cdot \Big(q_\alpha (\vec{E} + \vec{v} \times \vec{B}) + \frac{m_\alpha \vec{g}_{\mathrm{M}}}{(1+\frac{z}{R_{\mathrm{M}}})^2} \Big) \Big\rangle_\alpha \\
&= -n_\alpha \Big\langle q_\alpha (\vec{v} \cdot \vec{E} + \cancelto{0}{\vec{v} \cdot (\vec{v} \times \vec{B})}) + \vec{v} \cdot \frac{m_\alpha \vec{g}_{\mathrm{M}}}{(1+\frac{z}{R_{\mathrm{M}}})^2} \Big\rangle_\alpha = -n_\alpha \Big\langle q_\alpha (\vec{v} \cdot \vec{E}) + \vec{v} \cdot \frac{m_\alpha \vec{g}_{\mathrm{M}}}{(1+\frac{z}{R_{\mathrm{M}}})^2} \Big\rangle_\alpha \\
&= -\underbrace{n_\alpha q_\alpha \langle \vec{v} \rangle_\alpha}_{\vec{J}_\alpha} \cdot \vec{E} - n_\alpha m_\alpha \langle \vec{v} \rangle_\alpha \cdot \frac{\vec{g}_{\mathrm{M}}}{(1+\frac{z}{R_{\mathrm{M}}})^2} = -\vec{J}_\alpha \cdot \vec{E} - n_\alpha m_\alpha \vec{u}_\alpha \cdot \frac{\vec{g}_{\mathrm{M}}}{(1+\frac{z}{R_{\mathrm{M}}})^2}
\end{aligned}$$

We can express **IV** in terms of specific energy W_α and W_β (A.21). Furthermore, by integrating the Maxwellian distribution function (A.4), a representation of the energy contribution from elastic collisions can be found [*Shu*, 1992, p. 22]:

$$\int \Big(m_\alpha \frac{\vec{v}^2}{2} \Big) f_{\mathrm{m},\alpha}(\vec{v}, \vec{u}_\beta) d^3\vec{v} = \frac{3}{2} n_\alpha k_{\mathrm{B}} T_\alpha + \frac{1}{2} m_\alpha n_\alpha \vec{u}_\beta^2 \tag{A.23}$$

finally, (A.10) can be constructed.

$$\begin{aligned}
\mathbf{IV} &= \sum_n \nu^{\mathrm{S}}_{n\to\alpha} n_n \langle m_\alpha \frac{\vec{v}^2}{2} \rangle_n - \nu^{\mathrm{L}}_\alpha n_\alpha \langle m_\alpha \frac{\vec{v}^2}{2} \rangle_\alpha - \sum_\beta \nu_{\alpha,\beta} \Big(n_\alpha \langle m_\alpha \frac{\vec{v}^2}{2} \rangle_\alpha - \int m_\alpha \frac{\vec{v}^2}{2} f_{\mathrm{m},\alpha}(\vec{v}, \vec{u}_\beta) d^3\vec{v} \Big) \\
&= \sum_n \nu^{\mathrm{S}}_{n\to\alpha} \frac{m_\alpha}{m_n} n_n \underbrace{\langle m_n \frac{\vec{v}^2}{2} \rangle_n}_{(A.20)} - \nu^{\mathrm{L}}_\alpha n_\alpha \underbrace{\langle m_\alpha \frac{\vec{v}^2}{2} \rangle_\alpha}_{(A.20)} - \sum_\beta \nu_{\alpha,\beta} \Big(n_\alpha \underbrace{\langle m_\alpha \frac{\vec{v}^2}{2} \rangle_\alpha}_{(A.20)} - \underbrace{\int \Big(m_\alpha \frac{\vec{v}^2}{2} \Big) f_{\mathrm{m},\alpha}(\vec{v}, \vec{u}_\beta) d^3\vec{v}}_{(A.23)} \Big) \\
&= \sum_n \nu^{\mathrm{S}}_{n\to\alpha} \Big(m_\alpha n_n \frac{\vec{u}_n^2}{2} + m_\alpha n_n \mathcal{E}_n \Big) - \nu^{\mathrm{L}}_\alpha \Big(m_\alpha n_\alpha \frac{\vec{u}_\alpha^2}{2} + m_\alpha n_\alpha \mathcal{E}_\alpha \Big) - \ldots \\
&\sum_\beta \nu_{\alpha,\beta} \Big(\Big(m_\alpha n_\alpha \frac{\vec{u}_\alpha^2 - \vec{u}_\beta^2}{2} \Big) + m_\alpha n_\alpha \mathcal{E}_\alpha - \frac{3}{2} n_\alpha k_{\mathrm{B}} T_\alpha \Big)
\end{aligned}$$

Now, after substituting **I**−**IV** into (A.6) many of the terms can be canceled out, and then rearranged to form the energy equation in its most general form

$$\begin{aligned}
\frac{\partial}{\partial t}(m_\alpha n_\alpha \mathcal{E}_\alpha) + \nabla_{\vec{r}} \cdot (m_\alpha n_\alpha \mathcal{E}_\alpha \vec{u}_\alpha) = -(\bar{\bar{\Pi}}_\alpha \nabla_{\vec{r}}) \cdot \vec{u}_\alpha - \nabla_{\vec{r}} \cdot \vec{Q}_\alpha + \sum_n \nu^{\mathrm{S}}_{n\to\alpha} \Big(m_\alpha n_n \frac{\vec{u}_n^2 - \vec{u}_\alpha^2}{2} + m_\alpha n_n \mathcal{E}_n \Big) - \\
\nu^{\mathrm{L}}_\alpha m_\alpha n_\alpha \mathcal{E}_\alpha - \sum_\beta \nu_{\alpha,\beta} \Big(m_\alpha n_\alpha \mathcal{E}_\alpha - m_\alpha n_\alpha \frac{\vec{u}_\alpha^2 - \vec{u}_\beta^2}{2} - \frac{3}{2} n_\alpha k_{\mathrm{B}} T_\alpha \Big)
\end{aligned} \tag{A.24}$$

A.3 Ideal gas in an adiabatic process

The general forms of the conservation equations can be simplified through the assumption of an adiabatic process, which takes the following mathematical form

$$m_\alpha n_\alpha \mathcal{E}_\alpha = \frac{p_\alpha}{\gamma_\alpha - 1} \tag{A.25}$$

and for an ideal gas we can utilize

$$p_\alpha = n_\alpha k_\mathrm{B} T_\alpha \tag{A.26}$$

Furthermore, if we assume a non-viscous isotropic gas the stress tensor becomes much easier to deal with

$$\bar{\bar{\Pi}}_\alpha = p_\alpha \vec{I} \tag{A.27}$$

Where $\bar{\bar{\Pi}}_\alpha$ is the pressure tensor and $\vec{I}$ is the identity matrix. None of these approximations are needed to simplify the continuity equation (A.15), which is still:

$$\frac{\partial n_\alpha}{\partial t} + \nabla_{\vec{r}} \cdot (n_\alpha \vec{u}_\alpha) = \sum_n \nu^\mathrm{S}_{n\to\alpha} n_n - \nu^\mathrm{L}_\alpha n_\alpha \tag{A.28}$$

Only the approximation of the pressure tensor (A.27) is needed to simplify momentum conservation (A.17) to obtain:

$$\frac{\partial \vec{u}_\alpha}{\partial t} + \vec{u}_\alpha \cdot \nabla_{\vec{r}} \vec{u}_\alpha = \frac{q_\alpha}{m_\alpha}\left(\vec{E} + \vec{u}_\alpha \times \vec{B}\right) - \frac{\nabla_{\vec{r}} p_\alpha}{m_\alpha n_\alpha} + \frac{\vec{g}_\mathrm{M}}{\left(1 + \frac{z}{R_\mathrm{M}}\right)^2} + \sum_n \nu^\mathrm{S}_{n\to\alpha} \frac{n_\alpha}{n_\alpha}(\vec{u}_n - \vec{u}_\alpha) - \sum_\beta \nu_{\alpha,\beta}(\vec{u}_\alpha - \vec{u}_\beta) \tag{A.29}$$

Energy conservation (A.24) is where most of the simplification takes place after applying the adiabatic (A.25), ideal gas (A.26), and non-viscous isotropic pressure approximation (A.27). Ultimately, we get:

$$\begin{aligned}\frac{\partial p_\alpha}{\partial t} &= -\gamma_\alpha \nabla_{\vec{r}} \cdot (p_\alpha \vec{u}_\alpha) + (\gamma_\alpha - 1)\vec{u}_\alpha \cdot \nabla_{\vec{r}} p_\alpha - (\gamma_\alpha - 1)\nabla_{\vec{r}} \cdot \vec{Q}_\alpha + \sum_n \nu^\mathrm{S}_{n\to\alpha} \frac{m_\alpha}{m_n} \frac{\gamma_\alpha - 1}{\gamma_n - 1} p_n \\ &- \sum_\beta \nu_{\alpha,\beta}\left(\frac{5}{2} - \frac{3}{2}\gamma_\alpha\right) p_\alpha - \nu^\mathrm{L}_\alpha p_\alpha + (\gamma_\alpha - 1)\left(\sum_n \nu^\mathrm{S}_{n\to\alpha} m_\alpha n_n \frac{(\vec{u}_n - \vec{u}_\alpha)^2}{2} + \sum_\beta \nu_{\alpha,\beta} m_\alpha n_\alpha \frac{(\vec{u}_\beta - \vec{u}_\alpha)^2}{2}\right)\end{aligned} \tag{A.30}$$

after applying these approximations the gravitational term $\vec{g}_{\mathrm{M}}$ vanishes. We are left with the chemistry heat exchange $\vec{Q}_\alpha$ term, chemistry source term $\nu^{\mathrm{S}}_{n\to\alpha}$, chemistry loss term $\nu^{\mathrm{L}}_{\alpha}$, and elastic collision term $\nu_{\alpha,\beta}$.

A.4 Normalized equations

Define the following variables

$$\boxed{\begin{array}{lll} L_x = x_{\max} - x_{\min} \;\; ; & \delta_x = \dfrac{L_x}{m_x - 1} \;\; ; & h_x = \dfrac{\delta_x}{\ell_0} \\ L_y = y_{\max} - y_{\min} \;\; ; & \delta_y = \dfrac{L_y}{m_y - 1} \;\; ; & h_y = \dfrac{\delta_y}{\ell_0} \\ L_z = z_{\max} - z_{\min} \;\; ; & \delta_z = \dfrac{L_z}{m_z - 1} \;\; ; & h_z = \dfrac{\delta_z}{\ell_0} \end{array}}$$

L_x, L_y, and L_z are the domain dimensions in meters. The values $x_{\max}/x_{\min}$, $y_{\max}/y_{\min}$, and $z_{\max}/z_{\min}$ are the outer boundaries of the domain. The parameters δ_x, δ_y, and δ_z is the domain resolution in meters, which is calculated based on the domain dimensions and the number of grid points denoted by m_x, m_y, and m_z. Finally, the normalized domain resolution is unitless and is given by h_x, h_y, and h_z.

$$\boxed{\begin{array}{rcrcrcl} x &=& x_{\min} + i\delta_x &=& x_{\min} + ih_x\ell_0 &=& x_{\min} + \hat{x}\ell_0 \\ y &=& y_{\min} + j\delta_y &=& y_{\min} + jh_y\ell_0 &=& y_{\min} + \hat{y}\ell_0 \\ z &=& z_{\min} + k\delta_z &=& z_{\min} + kh_z\ell_0 &=& z_{\min} + \hat{z}\ell_0 \end{array}}$$

$$\boxed{\begin{array}{rcrcl} \hat{x} &=& \dfrac{x - x_{\min}}{\ell_0} &=& ih_x \\ \hat{y} &=& \dfrac{y - y_{\min}}{\ell_0} &=& jh_y \\ \hat{z} &=& \dfrac{z - z_{\min}}{\ell_0} &=& kh_z \\ \hat{t} &=& \dfrac{t - t_{\min}}{\tau_0} & & \end{array}}$$

Grid coordinates are given by i, j, and k. Geometric coordinates are then given in meters and represented by x, y, and z. Reduced variables are unitless and are shown as $\hat{t}$, $\hat{x}$, $\hat{y}$, and $\hat{z}$. The normalization can be fully defined by four reference parameters: m_0 (normalization mass), q_0 (normalization charge), B_0 (normalization magnetic field), n_0 (normalization number density). Altogether these define the *normalization plasma*. This is a plasma with a density n_0 of particles with mass m_0 and charge q_0 in a magnetic field B_0. The normalized plasma gyroperiod τ_0 and inertial length ℓ_0 are given by:

$$\tau_0 = \frac{1}{\Omega_{\mathrm{g},0}} = \frac{m_0}{q_0 B_0}$$

$$\ell_0 = \frac{c}{\omega_{\mathrm{p},0}} = \frac{\dfrac{1}{\sqrt{\mu_0 \varepsilon_0}}}{\sqrt{\dfrac{n_0 q_0^2}{m_0 \varepsilon_0}}} = \sqrt{\frac{m_0}{q_0^2 \mu_0 n_0}}$$

Assuming that m_0 and q_0 are set, then τ_0 is solely defined by B_0, and ℓ_0 by n_0. The normalized variables are given below:

$$\begin{array}{rclcrclcrclcrcl}
\hat{x}_\alpha & = & \dfrac{\vec{x}_\alpha}{\ell_0} & ; & \hat{v}_\alpha & = & \dfrac{\vec{v}_\alpha}{u_0} & ; & & & & & & & \\
\hat{n}_\alpha & = & \dfrac{n_\alpha}{n_0} & ; & \hat{u}_\alpha & = & \dfrac{\vec{u}_\alpha}{u_0} & ; & \hat{p}_\alpha & = & \dfrac{p_\alpha}{p_0} & ; & & & \\
\hat{B} & = & \dfrac{\vec{B}}{B_0} & ; & \hat{E} & = & \dfrac{\vec{E}}{E_0} & ; & \hat{J} & = & \dfrac{\vec{J}}{J_0} & ; & \hat{u}_n & = & \dfrac{\vec{u}_n}{u_0}
\end{array}$$

The continuity equation for ions utilizes the normalization gyroperiod and is taken from the ideal gas approximation for the conservation of mass (A.28)

$$\frac{\partial \hat{n}_i}{\partial \hat{t}} + \nabla_{\hat{r}} \cdot (\hat{n}_i \hat{u}_i) = \sum_n \nu^{\mathrm{S}}_{n \to i} \tau_0 \hat{n}_n - \nu^{\mathrm{L}}_i \tau_0 \hat{n}_i \tag{A.31}$$

Table A.1: Normalization of the equations.

symbol	definition	symbol (alt.)	interpretation (w.r.t. the normalizaion plasma)
	fundamental parameters		
n_0			number density
B_0			background magnetic field
m_0			particle mass
q_0			particle charge
	phase parameters		
τ_0	$=\dfrac{m_0}{q_0 B_0}$	$=\dfrac{1}{\Omega_{\mathrm{g},0}}$	gyroperiod
ℓ_0	$=\sqrt{\dfrac{m_0}{q_0^2 \mu_0 n_0}}$	$=\dfrac{c}{\omega_{\mathrm{p},0}}$	inertial length
	fluid parameters		
n_0			number density
u_0	$=\dfrac{\ell_0}{\tau_0}=\dfrac{B_0}{\sqrt{m_0 n_0 \mu_0}}$	$=v_{\mathrm{A},0}$	Alfvén speed
a_0	$=\dfrac{u_0}{\tau_0}$		acceleration
p_0	$=\dfrac{B_0^2}{\mu_0}=m_0 n_0 u_0^2$	$=p_{\mathrm{B},0}$	kinetic/magnetic pressure
	electromagnetic parameters		
J_0	$=q_0 n_0 u_0$		current
E_0	$=u_0 B_0$		electric field
B_0			magnetic field
η_0	$=\dfrac{B_0}{q_0 n_0}$	$=\dfrac{E_0}{J_0}$	plasma resistivity
$\mathcal{M}_0$	$=\dfrac{4\pi}{\mu_0} B_0 \ell_0^3$		magnetic dipole moment

We employ the quasi-neutrality assumption, which tells us that the number of electrons are always equal to the sum of the ions

$$\boxed{\hat{n}_e = \sum_i \hat{n}_i} \tag{A.32}$$

Starting from (A.29) and utilizing the normalization parameters and the fact that the

heat term is dropped, the momentum equation for ions yields:

$$\boxed{\begin{aligned}\frac{\partial \hat{u}_i}{\partial \hat{t}} =& - \hat{u}_i \cdot \hat{\nabla}_{\hat{r}} \hat{u}_i + \frac{\hat{q}_i}{\hat{m}_i}\left(\hat{E} + \hat{u}_i \times \hat{B}\right) - \frac{\hat{\nabla}_{\hat{r}} \hat{p}_i}{\hat{m}_i \hat{n}_i} - \frac{\frac{g_{\mathrm{M}}}{a_0}\hat{z}}{\left(1 + \frac{z}{R_{\mathrm{M}}}\right)^2} + ... \\ & \sum_n \nu^{\mathrm{S}}_{n\to i}\tau_0 \frac{\hat{n}_n}{\hat{n}_i}(\hat{u}_n - \hat{u}_i) + \sum_\beta \nu_{i,\beta}\tau_0\left(\hat{u}_\beta - \hat{u}_i\right)\end{aligned}} \tag{A.33}$$

The electron velocity is derived by employing Ampere's law of currents:

$$\begin{aligned}\vec{J} &= \sum_\alpha q_\alpha n_\alpha \vec{u}_\alpha \\ \Rightarrow \vec{u}_{\mathrm{e}} &= \sum_i \frac{q_i n_i}{e n_{\mathrm{e}}}\vec{u}_i - \frac{\vec{J}}{e n_{\mathrm{e}}}\end{aligned}$$

And therefore:

$$\boxed{\hat{u}_e = \sum_i \frac{\hat{q}_i \hat{n}_i}{\hat{q}_e \hat{n}_e}\hat{u}_i - \frac{\hat{J}}{\hat{q}_e \hat{n}_e}} \tag{A.34}$$

Starting from the approximation of an ideal gas in an adiabatic process, neglecting the heat term, and assuming elastic collisions, conservation of energy for ions is simplified to:

$$\boxed{\begin{aligned}\frac{\partial \hat{p}_i}{\partial \hat{t}} =& \gamma_i \hat{\nabla}_{\hat{r}} \cdot (\hat{p}_i \hat{u}_i) + (\gamma_i - 1)\,\hat{u}_i \cdot \hat{\nabla}_{\hat{r}} \hat{p}_i + \sum_n \nu^{\mathrm{S}}_{n\to i}\tau_0 \frac{\hat{m}_i}{\hat{m}_n}\frac{\gamma_i - 1}{\gamma_n - 1}\hat{p}_n - ... \\ & \nu^{\mathrm{L}}_i \tau_0 \hat{p}_i + (\gamma_i - 1)\sum_n \nu^{\mathrm{S}}_{n\to i}\tau_0 \hat{m}_i \hat{n}_n \frac{(\hat{u}_n - \hat{u}_i)^2}{2}\end{aligned}} \tag{A.35}$$

And through the same process electron energy is given:

$$\boxed{\begin{aligned}\frac{\partial \hat{p}_{\mathrm{e}}}{\partial \hat{t}} =&\gamma_{\mathrm{e}}\hat{\nabla}_{\hat{r}}\cdot\left(\hat{p}_{\mathrm{e}}\hat{u}_{\mathrm{e}}\right)+\left(\gamma_{\mathrm{e}}-1\right)\hat{u}_{\mathrm{e}}\cdot\hat{\nabla}_{\hat{r}}\hat{p}_{\mathrm{e}}+\sum_{n}\nu^{\mathrm{S}}_{n\rightarrow\mathrm{e}}\tau_0\frac{\hat{m}_{\mathrm{e}}}{\hat{m}_n}\frac{\gamma_{\mathrm{e}}-1}{\gamma_n-1}\hat{p}_n-\ldots\\ &\nu^{\mathrm{L}}_{\mathrm{e}}\tau_0\hat{p}_{\mathrm{e}}+\left(\gamma_{\mathrm{e}}-1\right)\sum_{n}\nu^{\mathrm{S}}_{n\rightarrow\mathrm{e}}\tau_0\hat{m}_{\mathrm{e}}\hat{n}_n\frac{\left(\hat{u}_n-\hat{u}_{\mathrm{e}}\right)^2}{2}\end{aligned}} \tag{A.36}$$

Together these equations form the fluid description of M^4. The electrodynamic description is given by Ampèrè's Law (A.37), Faraday's law (A.38), and Generalized Ohm's law (A.39).

$$\boxed{\hat{J}=\hat{\nabla}_{\hat{r}}\times\hat{B}} \tag{A.37}$$

$$\boxed{\frac{\partial \hat{B}}{\partial \hat{t}}=-\hat{\nabla}_{\hat{r}}\times\hat{E}} \tag{A.38}$$

$$\boxed{\begin{aligned}\hat{E}=&-\sum_{i}\frac{\hat{q}_i\hat{n}_i}{\hat{q}_{\mathrm{e}}\hat{n}_{\mathrm{e}}}\hat{u}_i\times\hat{B}+\frac{\hat{J}\times\hat{B}}{\hat{q}_{\mathrm{e}}\hat{n}_{\mathrm{e}}}-\frac{\hat{\nabla}_{\hat{r}}\hat{p}_{\mathrm{e}}}{\hat{q}_{\mathrm{e}}\hat{n}_{\mathrm{e}}}+\frac{\hat{m}_{\mathrm{e}}}{\hat{q}_{\mathrm{e}}}\sum_{n}\nu^{\mathrm{S}}_{n\rightarrow\mathrm{e}}\tau_0\left(\hat{u}_n-\hat{u}_{\mathrm{e}}\right)+\ldots\\ &\frac{\hat{m}_{\mathrm{e}}}{\hat{q}_{\mathrm{e}}}\sum_{n}\nu_{n-\mathrm{e}}\tau_0\left(\hat{u}_n-\hat{u}_{\mathrm{e}}\right)+\frac{\hat{m}_{\mathrm{e}}}{\hat{q}_{\mathrm{e}}}\sum_{i}\nu_{i-\mathrm{e}}\tau_0\left(\hat{u}_i-\hat{u}_{\mathrm{e}}\right)\end{aligned}} \tag{A.39}$$

Bibliography

Acuña, M. H. (1999), Global distribution of crustal magnetization discovered by the Mars Global Surveyor MAG/ER experiment, *Science*, *284*(5415), 790–793, doi:10.1126/science.284.5415.790.

Baierlein, R. (1999), *Thermal Physics*, Cambridge University Press, doi:10.1017/CBO9780511840227.

Balay, S., S. Abhyankar, M. F. Adams, J. Brown, P. Brune, K. Buschelman, L. Dalcin, V. Eijkhout, W. D. Gropp, D. Kaushik, M. G. Knepley, D. A. May, L. C. McInnes, R. T. Mills, T. Munson, K. Rupp, P. Sanan, B. F. Smith, S. Zampini, H. Zhang, and H. Zhang (2018), PETSc users manual, *Tech. Rep. ANL-95/11 - Revision 3.9*, Argonne National Laboratory.

Barth, Stewart, Bougher, Hunten, Bauer, and Nagy (1992), *Aeronomy of the current Martian atmosphere*, p. 1054, Univ. of Arizona Press.

Bertaux, J.-L., F. Leblanc, O. Witasse, E. Quemerais, J. Lilensten, S. A. Stern, B. Sandel, and O. Korablev (2005), Discovery of an aurora on Mars, *Nature*, *435*(7043), 790–794, doi:10.1038/nature03603.

Bhatnagar, P. L., E. P. Gross, and M. Krook (1954), A model for collision processes in gases. i. small amplitude processes in charged and neutral one-component systems, *Phys. Rev.*

Bößwetter, A., H. Lammer, Y. Kulikov, U. Motschmann, and S. Simon (2010), Non-thermal water loss of the early Mars: 3D multi-ion hybrid simulations, *Planet. Space Sci.*, *58*(14), 2031 – 2043, doi:10.1016/j.pss.2010.10.003.

Bougher, S. W., T. M. McDunn, K. A. Zoldak, and J. M. Forbes (2009), Solar cycle variability of Mars dayside exospheric temperatures: Model evaluation of underlying thermal balances, *Geophys. Res. Lett.*, *36*(5), doi:10.1029/2008gl036376.

Bougher, S. W., T. E. Cravens, J. Grebowsky, and J. Luhmann (2014), The aeronomy of Mars: Characterization by MAVEN of the upper atmosphere reservoir that regulates volatile escape, *Space Sci. Rev.*, *195*(1-4), 423–456, doi:10.1007/s11214-014-0053-7.

Brain, D. A., J. P. McFadden, J. S. Halekas, J. E. P. Connerney, S. W. Bougher, S. Curry, C. F. Dong, Y. Dong, F. Eparvier, X. Fang, K. Fortier, T. Hara, Y. Harada, B. M. Jakosky, R. J. Lillis, R. Livi, J. G. Luhmann, Y. Ma, R. Modolo, and K. Seki (2015), The spatial distribution of planetary ion fluxes near Mars observed by MAVEN, *Geophys. Res. Lett.*, *42*(21), 9142–9148, doi:10.1002/2015gl065293.

Chapman, S. (1931), The absorption and dissociative or ionizing effect of monochromatic radiation in an atmosphere on a rotating Earth, *Proc. of the Phys. Soc.*, *43*(1), 26–45, doi:10.1088/0959-5309/43/1/305.

Connerney, J. E. P., M. H. Acuna, P. J. Wasilewski, N. F. Ness, H. Rème, C. Mazelle, D. Vignes, R. P. Lin, D. L. Mitchell, and P. A. Cloutier (1999), Magnetic lineations in the ancient crust of Mars, *Science*, *284*(5415), 794–798, doi:10.1126/science.284.5415.794.

Courant, R., K. Friedrichs, and H. Lewy (1967), On the partial difference equations of mathematical physics, *IBM J. of Res. Dev.*, *11*(2), 215–234, doi:10.1147/rd.112.0215.

Crider, D. H., D. A. Brain, M. H. Acuña, D. Vignes, C. Mazelle, and C. Bertucci (2004), Mars global surveyor observations of solar wind magnetic field draping around mars, in *Mars' Magnetism and Its Interaction with the Solar Wind*, pp. 203–221, Springer Netherlands, doi:10.1007/978-0-306-48604-3_5.

Dong, C., Y. Lee, Y. Ma, M. Lingam, S. Bougher, J. Luhmann, S. Curry, G. Toth, A. Nagy, V. Tenishev, X. Fang, D. Mitchell, D. Brain, and B. Jakosky (2018), Modeling Martian atmospheric losses over time: Implications for exoplanetary climate evolution and habitability, *Astrophys. J.*, *859*(1), L14, doi:10.3847/2041-8213/aac489.

Fillingim, M., L. Peticolas, R. Lillis, D. Brain, J. Halekas, D. Lummerzheim, and S. Bougher (2010), Localized ionization patches in the nighttime ionosphere of Mars and their electrodynamic consequences, *Icarus*, *206*(1), 112–119, doi:10.1016/j.icarus.2009.03.005.

Fillingim, M. O., R. J. Lillis, S. L. England, L. M. Peticolas, D. A. Brain, J. S. Halekas, C. Paty, D. Lummerzheim, and S. W. Bougher (2012), On wind-driven electrojets at magnetic cusps in the nightside ionosphere of Mars, *Earth Planets Space*, *64*(2), 5, doi:10.5047/eps.2011.04.010.

Forget, F., F. Hourdin, R. Fournier, C. Hourdin, O. Talagrand, M. Collins, S. R. Lewis, P. L. Read, and J.-P. Huot (1999), Improved general circulation models of the martian atmosphere from the surface to above 80 km, *J. Geophys. Res.*, *104*(E10), 24,155–24,175, doi:10.1029/1999je001025.

Fox, J. (2004), Advances in the aeronomy of Venus and Mars, *Adv. in Space Res.*, *33*(2), 132 – 139, doi:10.1016/j.asr.2003.08.014, Planetary Atmospheres, Ionospheres and Plasma Interactions.

Gilat, A. (2013), *Numerical Methods for Engineers and Scientists*, 3 ed., John Wiley & Sons Inc, ISBN: 1118554930.

Green, J. (2017), A Future Mars Environment For Science and Exploration, in *Planetary Science Vision 2050 Workshop*.

Haider, S. A., J. Kim, A. F. Nagy, C. N. Keller, M. I. Verigin, K. I. Gringauz, N. M. Shutte, K. Szego, and P. Kiraly (1992), Calculated ionization rates, ion densities, and airglow emission rates due to precipitating electrons in the nightside ionosphere of Mars, *J. Geophys. Res.*, *97*(A7), 10,637, doi:10.1029/92ja00317.

Halekas, J., D. Brain, R. Lin, J. Luhmann, and D. Mitchell (2008), Distribution and variability of accelerated electrons at Mars, *Adv. Space Res.*, *41*(9), 1347 – 1352, doi:10.1016/j.asr.2007.01.034.

Hanson, W. B., S. Sanatani, and D. R. Zuccaro (1977), The Martian ionosphere as observed by the Viking retarding potential analyzers, *J. Geophys. Res.*, *82*(28), 4351–4363, doi:10.1029/JS082i028p04351.

Hinson, D. P., R. A. Simpson, J. D. Twicken, G. L. Tyler, and F. M. Flasar (1999), Initial results from radio occultation measurements with Mars Global Surveyor, *J. Geophys. Res.*, *104*(E11), 26,997–27,012, doi:10.1029/1999je001069.

Hoehler, T., J. Eigenbrode, S. Rafkin, P. Withers, S. Ruff, R. Yingst, D. Lim, and R. Whitley (2015), MEPAG (2015), Mars Scientific Goals, Objectives, Investigations, and Priorities: 2015, *Hamilton*.

Itikawa, Y. (2002), Cross sections for electron collisions with carbon dioxide, *J. Phys. Chem. Ref. Data*, *31*(3), 749–767, doi:10.1063/1.1481879.

Jakosky, B. M., J. M. Grebowsky, J. G. Luhmann, and D. A. Brain (2015), Initial results from the MAVEN mission to Mars, *Geophys. Res. Lett.*, *42*(21), 8791–8802, doi:10.1002/2015gl065271.

Kopf, A. J., D. A. Gurnett, D. D. Morgan, and D. L. Kirchner (2008), Transient layers in the topside ionosphere of Mars, *Geophys. Res. Lett.*, *35*(17), doi:10.1029/2008GL034948.

Krasnopolsky, V. A. (2002), Mars upper atmosphere and ionosphere at low, medium, and high solar activities: Implications for evolution of water, *J. Geophys. Res.*, *107*(E12), doi:10.1029/2001je001809.

Langlais, B., M. E. Purucker, and M. Mandea (2004), Crustal magnetic field of Mars, *J. Geophys. Res.*, *109*(E2), doi:10.1029/2003je002048.

Ledvina, S. A., Y.-J. Ma, and E. Kallio (2008), Modeling and Simulating Flowing Plasmas and Related Phenomena, *Space Sci. Rev.*, *139*(1), 143–189, doi:10.1007/s1121400893846.

Lewis, S. R., M. Collins, P. L. Read, F. Forget, F. Hourdin, R. Fournier, C. Hourdin, O. Talagrand, and J.-P. Huot (1999), A climate database for Mars, *J. Geophys. Res.*, *104*(E10), 24,177–24,194, doi:10.1029/1999je001024.

Lieberman, M. A., and A. J. Lichtenberg (2005), *Plasma Dynamics*, pp. p. 87–132, Wiley, New York NY, doi:10.1002/0471724254.ch4.

Lillis, R. J., M. O. Fillingim, L. M. Peticolas, D. A. Brain, R. P. Lin, and S. W. Bougher (2009), Nightside ionosphere of Mars: Modeling the effects of crustal magnetic fields and electron pitch angle distributions on electron impact ionization, *J. Geophys. Res.*, *114*(E11), doi:10.1029/2009je003379.

Ma, Y.-J., A. F. Nagy, T. E. Cravens, I. V. Sokolov, J. Clark, and K. C. Hansen (2004), 3-D global MHD model prediction for the first close flyby of Titan by Cassini, *Geophys. Res. Lett.*, *31*(22), doi:10.1029/2004gl021215.

Mitchell, D. L., R. P. Lin, C. Mazelle, H. Rasme, P. A. Cloutier, J. E. P. Connerney, M. H. Acuna, and N. F. Ness (2001), Probing Mars' crustal magnetic field and ionosphere with the MGS electron reflectometer, *J. Geophys. Res.*, *106*(E10), 23,419–23,427, doi:10.1029/2000JE001435.

Najib, D., A. F. Nagy, G. Toth, and Y. Ma (2011), Three-dimensional, multifluid, high spatial resolution mhd model studies of the solar wind interaction with Mars, *J. Geophys. Res.*, *116*(A5), doi:10.1029/2010JA016272, A05204.

Purucker, M., D. Ravat, H. Frey, C. Voorhies, T. Sabaka, and M. Acuna (2000), An altitude-normalized magnetic map of Mars and its interpretation, *Geophys. Res. Lett.*, *27*(16), 2449–2452, doi:10.1029/2000gl000072.

Riousset, J. A., C. S. Paty, R. J. Lillis, M. O. Fillingim, S. L. England, P. G. Withers, and J. P. M. Hale (2013), Three-dimensional multifluid modeling of atmospheric

electrodynamics in Mars' dynamo region, *J. Geophys. Res.*, *118*(6), 3647–3659, doi:10.1002/jgra.50328.

Riousset, J. A., C. S. Paty, R. J. Lillis, M. O. Fillingim, S. L. England, P. G. Withers, and J. P. M. Hale (2014), Electrodynamics of the Martian dynamo region near magnetic cusps and loops, *Geophys. Res. Lett.*, *41*, 1119–1125, doi:10.1002/2013GL059130.

Romanelli, N., R. Modolo, F. Leblanc, J.-Y. Chaufray, S. Hess, D. Brain, J. Connerney, J. Halekas, J. McFadden, and B. Jakosky (2018), Effects of the crustal magnetic fields and changes in the IMF orientation on the magnetosphere of Mars: MAVEN observations and results., *J. Geophys. Res.*, doi:10.1029/2017ja025155.

Schunk, and Nagy (2000), *Ionospheres*, 231-253, Cambridge University Press, Cambridge, UK.

Shinagawa, H. (2000), Our current understanding of the ionosphere of Mars, *Adv. Space Res.*, *26*(10), 1599–1608, doi:10.1016/S0273-1177(00)00099-5, Planetary Ionospheres and Magnetospheres.

Shu (1992), *The physics of astrophysics. Volume II: Gas dynamics.*, University Science Books.

Trotignon, J., M. Parrot, J. Cerisier, M. Menvielle, W. Axford, M. Pätzold, R. Warnant, and A. Wernik (2000), The plasma environment of Mars: From the shocked solar wind down to the ionosphere, *Planet. Space Sci.*, *48*(12), 1181–1191, doi:10.1016/S0032-0633(00)00102-1, Mars Exploration Program.

Withers, P. (2008), Theoretical models of ionospheric electrodynamics and plasma transport, *J. Geophys. Res.*, *113*(A7), doi:10.1029/2007ja012918.

Withers, P. (2009), A review of observed variability in the dayside ionosphere of Mars, *Adv. Space Res.*, *44*, 277–307, doi:10.1016/j.asr.2009.04.027.

Withers, P., and M. Mendillo (2005), Response of peak electron densities in the Martian ionosphere to day-to-day changes in solar flux due to solar rotation, *Planet. Space Sci.*, *53*(14-15), 1401–1418, doi:10.1016/j.pss.2005.07.010.

Zhang, M. H. G., J. G. Luhmann, A. J. Kliore, and J. Kim (1990), A post Pioneer Venus reassessment of the Martian dayside ionosphere as observed by radio occultation methods, *J. Geophys. Res.*, *95*(B9), 14,829–14,839, doi:10.1029/JB095iB09p14829.